Single Particle ICP-MS:

Capabilities of Microsecond Time Resolution and Coupling to Capillary Electrophoresis

DISSERTATION

Darya Mozhayeva

University of Siegen

Siegen 2019

Single Particle ICP-MS:

Capabilities of Microsecond Time Resolution and Coupling to Capillary Electrophoresis

DISSERTATION

to obtain the degree of Doctor of Science (Dr. rer. nat.)

submitted by M. Sc. Darya Mozhayeva

born in Almaty

School of Science and Technology

University of Siegen

Siegen 2019

Supervisor and first reviewer

Prof. Dr. Carsten Engelhard

University of Siegen

Second reviewer

Prof. Dr. Holger Schönherr

University of Siegen

Date of the oral examination

12 July 2019

printed on non-ageing wood-free and acid-free paper

“Наука начинается с тех пор, как начинают измерять.

Точная наука немыслима без меры.”

Д. И. Менделеев

“Science begins as soon as one begins to measure.

Exact science is unthinkable without a measure.”

D. I. Mendeleev

Abstract

Single particle inductively coupled plasma mass spectrometry (SP-ICP-MS) is a method that allows to obtain size, size distribution, and particle number concentration of nanoparticles (NPs) in suspensions only after few minutes of measurement. However, several challenges of commercially available SP-ICP-MS instruments currently exist that limit the analytical performance of the method. This thesis reports novel developments and improvements of SP-ICP-MS with the ultimate goal to be able to use it as a routine NP analysis method in the future.

First, the state-of-the-art in SP-ICP-MS is reviewed on a step-by-step basis, from the sample introduction system to the detector. Applications of the method for the analysis of nanomaterials are critically discussed and current challenges are highlighted. Necessary improvements and directions for further developments are identified.

Second, capillary electrophoresis (CE) is coupled to SP-ICP-MS and used for the first time with a data aquistion system (DAQ) that provides microsecond time resolution (5 µs dwell time, µsDAQ) for the separation and characterization of mixtures of Ag NPs. An online preconcentration approach is implemented to decrease the detection limits to the sub-microgram-per-liter range. In addition, it is demonstrated for the first time that the optimized CE-SP-ICP-MS method can be successfully used to separate NPs with similar sizes but different surface coatings. Each component in a complex mixture of 20 nm, 40 nm, 60 nm sized citrate-coated and 40 nm, 60 nm sized PVP-coated Ag NPs can be distinguished.

Finally, a novel data processing algorithm for SP-ICP-MS with the µsDAQ is developed to extract NP signals from a continuous background signal. The method is based on Poisson statistics and allows to distinguish and quantify both NPs and dissolved elements. It is demonstrated that Ag NPs (20 nm – 100 nm) can be identified on a particle-by-particle level even in the presence of a significant concentration of ionic background (Ag^+ up to 7.5 µg L^{-1}, $^{107}Ag^+$ up to 1 000 000 counts per second).

Zusammenfassung

Die Massenspektrometrie mit induktiv gekoppeltem Plasma im Einzelpartikel-Modus (SP-ICP-MS) ist eine Methode, mit der sich die Größe, die Größenverteilung und die Partikelkonzentration von Nanopartikeln (NP) in Suspensionen innerhalb von wenigen Minuten bestimmen lassen. Obwohl die SP-ICP-MS kommerziell erhältlich ist, gibt es zahlreiche Herausforderungen, die die analytischen Leistungskenndaten und die Anwendbarkeit der Methode für die Nanomaterialanalytik beschränken. Die vorliegende Arbeit beschäftigt sich mit der Entwicklung und Optimierung von neuen Ansätzen in der SP-ICP-MS, um diese in der Zukunft noch besser als Analysemethode für die Nanomaterialanalytik einsetzen zu können.

Zunächst wird der Stand der Technik auf dem Gebiet der SP-ICP-MS schrittweise vom Probeneinführungssystem bis zum Detektor kritisch diskutiert. Wichtige Anwendungen werden rezensiert und notwendige methodische und apparative Verbesserungen werden identifiziert.

Im Ergebnisteil der Arbeit wird eine neuartige Methode vorgestellt, die auf der Kopplung von Kapillarelektrophorese (CE) mit SP-ICP-MS beruht, mit einem kontinuierlichen Datenerfassungssystem mit Mikrosekundenzeitauflösung (5 µs Integrationszeit) arbeitet und erfolgreich für die Charakterisierung von Ag NP eingesetzt wird. Ebenso wird eine Methode zur Online-Aufkonzentration implementiert, um die Nachweisgrenzen zu verbessern (µg L^{-1} – Bereich). Schließlich wird die CE-SP-ICP-MS zur Trennung von NP mit ähnlichen Größen, jedoch unterschiedlichen Oberflächenbeschichtungen verwendet. Jede Komponente in einer komplexen Mischung, welche 20 nm, 40 nm und 60 nm große Citrat-beschichtete Ag NP, sowie 40 nm und 60 nm große PVP-beschichtete Ag NP enthielt, kann unterschieden werden.

Zum Schluss wird ein Datenverarbeitungsalgorithmus für die SP-ICP-MS mit µsDAQ vorgestellt. Die entwickelte Methode basiert auf der Poisson-Statistik und ermöglicht die Unterscheidung und Quantifizierung von NP und gelösten Elementen. Das Verfahren ermöglicht den Nachweis von Ag NP (von 20 nm bis 100 nm) in Anwesenheit einer signifikanten Konzentration an ionischem Hintergrund (Ag^+ bis zu 7.5 µg L^{-1}, $^{107}Ag^+$ bis zu 1 000 000 Anzahl von Impulsen pro Sekunde).

Table of Contents

Chapter 1 Aims and Scope of the Thesis 1

1.1 Introduction 2

1.2 Aims and Scope 4

Chapter 2 Single Particle ICP-MS – A Critical Review of the State-of-the-Art 7

2.1 Introduction 8

2.1.1 Nanomaterials 8

2.1.2 Principle and early development of SP-ICP-MS 9

2.2 Towards the Ideal SP-ICP-MS Method 10

2.2.1 Sample Preparation 12

2.2.2 Sample Introduction 13

2.2.3 NPs in the ICP Source 15

2.2.4 Ion Transport 19

2.2.5 Mass Analyzers 20

2.2.6 Detector Dwell Time 22

2.2.7 Quantification Considerations 24

2.2.8 Coupling of SP-ICP-MS to Separation Techniques 26

2.3 Applications of SP-ICP-MS 33

2.4 Conclusion 84

Chapter 3 Implementation of Online Preconcentration and Microsecond Time Resolution to CE-SP-ICP-MS 87

3.1 Introduction 88

3.2 Experimental Section 91

3.2.1 Sample Preparation 91

3.2.2 Instrumentation 91

3.2.3 CE Injection Volume Determination 93

3.2.4 Data Acquisition and Data Processing 94

3.3 Results and Discussion 95

3.3.1 The Effect of CE Separation Conditions on NP Ion Clouds Profiles . 95

3.3.2 CE-SP-ICP-MS Capabilities 96
3.3.3 REPSM Method Development 98
3.3.4 Quantification of NPs in Mixtures 102
3.3.5 Preconcentration Efficiency in CE-SP-ICP-MS for Ag NPs Mixtures 104
3.4 Conclusion 106
Chapter 4 Separation of Silver Nanoparticles with Different Coatings by CE-SP-ICP-MS 107
4.1 Introduction 108
4.2 Experimental Section 111
4.2.1 Sample Preparation 111
4.2.2 Instrumentation 111
4.2.3 Data Processing 113
4.3 Results and Discussion 113
4.3.1 Theoretical Considerations on NPs Migration Order 113
4.3.2 Separation of 20 nm Sized NPs with Different Coatings 114
4.3.3 Separation of 40 nm Sized NPs with Different Coatings 115
4.3.4 Separation of 60 nm Sized NPs with Different Coatings 118
4.3.5 Separation of Complex Mixtures with CE-SP-ICP-MS 120
4.4 Conclusion 124
Chapter 5 A Quantitative Nanoparticle Extraction Method for Microsecond Time Resolved SP-ICP-MS Data in the Presence of High Background 125
5.1 Introduction 126
5.2 Experimental Section 129
5.2.1 Sample Preparation 129
5.2.2 Instrumentation 129
5.2.3 Data Acquisition and Data Processing 130
5.3 Results and Discussion 133
5.3.1 Quantification of Ionic Silver in the Presence of NPs with Millisecond Time Resolution 133
5.3.2 Matrix Effects in the Plasma 133
5.3.3 Background Correction for NP Signals Recorded with Microsecond Time Resolution (µsDAQ) 136

5.3.4 Limits for Qualitative NPs Ion Cloud Extraction for the μsDAQ ... 137
5.3.5 Optimization of the Ion Cloud Extraction Conditions 141
5.3.6 Workflow after Method Optimization..... 144
5.4 Conclusion 146
Chapter 6 Concluding Remarks and Future Perspectives..... 147
6.1 Summary and Concluding Remarks 148
6.2 Future Perspectives 150
Appendix..... 153
References..... 167
List of Abbreviations 191
List of Figures 195
List of Tables 199
Acknowledgements 201

Chapter 1

Aims and Scope of the Thesis

Based on:

D. Mozhayeva, C. Engelhard, A Critical Review of Single Particle Inductively Coupled Plasma Mass Spectrometry – A Step Towards the Ideal Method for Nanomaterials Characterization, *J. Anal. At. Spectrom.*, 2019, DOI: 10.1039/C9JA00206E.

D. Mozhayeva, I. Strenge, C. Engelhard, Implementation of Online Preconcentration and Microsecond Time Resolution to Capillary Electrophoresis Single Particle Inductively Coupled Plasma Mass Spectrometry (CE-SP-ICP-MS) and its Application in Silver Nanoparticle Analysis, *Anal. Chem.*, 2017, **89**, 7152-7159.

D. Mozhayeva, C. Engelhard, Separation of Silver Nanoparticles with Different Coatings by Capillary Electrophoresis Coupled to ICP-MS in Single Particle Mode, *Anal. Chem.*, 2017, **89**, 9767-9774.

D. Mozhayeva, C. Engelhard, A Quantitative Nanoparticle Extraction Method for Microsecond Time Resolved Single-Particle ICP-MS Data in the Presence of High Background, *J. Anal. At. Spectrom.*, 2019, DOI: 10.1039/C9JA00042A.

1.1 Introduction

With the advancements in nanoscience the utilization of engineered nanoparticles (NPs) has recently increased, particularly in consumer products.[1, 2] Ag NPs are among the most utilized nanomaterials, especially in clothing, food supplements, appliances, electronics, etc. due to their antimicrobial activity. However, for more than 50% of the products that are listed in the nanomaterials containing consumer products databases,[1, 2] it is not specified, which nanomaterial was used during their production. Clearly, a robust analysis method will be required for these products and raw materials. After their use nanomaterials may be released into the environment, where transformations may take place.[3] In recent environmental exposure studies the predicted environmental concentrations of Ag NPs in surface waters were calculated to range from ng L^{-1} concentrations to low µg L^{-1} concentrations.[4, 5] Consequently, a sensitive method is required for NP size separation and characterization when a suspension (consumer products or environmental samples) contains NPs with different sizes.

An ideal characterization method for NP containing suspensions should cover the determination of the NPs chemical composition, size, and size distribution. It should provide the particle number concentration (PNC) for each NP size range that is present in a mixture and allow for the determination of additional parameters such as surface coating and shape of the of NPs. Different microscopy techniques (scanning electron microscopy, transmission electron microscopy (TEM), atomic force microscopy (AFM)) can be used for assessment of NP shape, diameter, and size distribution. High spatial resolution of up to 1 nm allows for visual inspection of individual NPs.[6] However, these methods can be time-consuming, the area that is analyzed may not represent the whole sample, and measurement artifacts may affect the results because only the NP surface projection is measured.[6]

Techniques based on inductively coupled plasma mass spectrometry (ICP-MS) can be used to separate and directly analyse the NPs and dissolved metals. Single particle (SP)-ICP-MS utilizes short dwell times (DTs) (typically in the low to sub-millisecond range) and time-resolved data acquisition to detect single NPs

in sufficiently diluted suspension with minimal sample pretreatment (dilution) at environmentally relevant concentrations (low nanogram-per-litre range for NPs). Individual NPs sizes can be assessed through mass-related counts detected at a given mass-to-charge ratio (*m*/*z*). These signals can be characterized as individual spikes from NPs, whereas the background (BG) represents the level of dissolved metal in the solution.[7] Several reviews summarized the capabilities and limitations of SP-ICP-MS[8-10], emphasizing that there is still room for improvement. Namely, more well-characterized standards are needed for size and PNC determination, matrix effects require more detailed investigations and should be accounted for, the linear dynamic range of the pulse counting stage of the secondary electron multiplier (SEM) is limited, etc.

The development of the prototype data acquisition system that allows to acquire SP-ICP-MS data continuously with up to 5 μs time resolution (μsDAQ)[11] opens new opportunities for the precise characterization of NPs. Capillary electrophoresis (CE) has a unique separation principle based on NP charge-to-size ratio (C/S) that can be used for separation of NPs with different sizes. Microsecond time resolution for SP-ICP-MS and CE coupled to SP-ICP-MS (CE-SP-ICP-MS) broadens the capabilities of both methods.

1.2 Aims and Scope

The thesis is dedicated to the development of novel techniques and improvement of existing methods for NPs analysis and characterization using SP-ICP-MS and CE-SP-ICP-MS.

Chapter 2 is focused on literature review of SP-ICP-MS as a method. Instrumental developments in SP-ICP-MS are reviewed on a step-by-step basis, from the sample introduction system to the detector. Necessary improvements and directions for further developments are identified in order for the method to get closer to "an ideal method for atomic spectroscopy".[12] The second part of the review is dedicated to applications of SP-ICP-MS. Key steps in sample preparation and selected instrumental conditions that are used in the published literature are summarized in a table. The table may serve as a guide for SP-ICP-MS users to choose an experimental procedure depending on the matrix that is present in the sample.

In Chapter 3, CE-SP-ICP-MS is used for the first time with a μsDAQ system to separate and quantify mixtures of Ag NPs. Additionally, an online preconcentration technique (reversed electrode polarity stacking mode, REPSM) is applied for Ag NPs analysis with CE-SP-ICP-MS for the first time. After optimization, best results are achieved using an injection time of 110 s and a constant pressure of 50 mbar in hydrodynamic injection mode. It is possible to detect 14 ± 2 times more 20 nm sized, 21 ± 4 times more 40 nm sized, and 28 ± 5 times more 60 nm sized Ag NPs compared to the standard injection time of only 3 s. The possibility to separate 20 nm, 40 nm, and 60 nm sized Ag NPs simultaneously present in a mixture is demonstrated over a broad concentration range.

In Chapter 4 the possibility to separate mixtures of Ag NPs with similar sizes but different surface coatings using CE-SP-ICP-MS is investigated. In two-component mixtures it is possible to separate 40 nm sized polyvinylpyrrolidone (PVP) and citrate-coated, 40 nm sized polyethylene glycol (PEG) and citrate-coated, and 60 nm sized PVP and citrate-coated NPs. The separation of a more complex mixture containing NPs with the different coatings and sizes is successful,

and each component, namely 20 nm, 40 nm, 60 nm sized citrate-coated and 40 nm, 60 nm sized PVP-coated NPs, can be distinguished. The theoretically expected migration order is confirmed by experimental results with selected Ag NPs. Based on the experimental observations a separation mechanism that considers the effect of stable vs. displaceable coatings during NP migration in CE is suggested.

The detection of NPs in the presence of high BG is challenging in SP-ICP-MS and leads to inaccurate quantification. In Chapter 5, a data processing procedure for the deconvolution of SP-ICP-MS data and its application to quantification of both the Ag NP size distribution (20 to 100 nm Ag NPs) and the concentration of Ag^+ (up to 7.5 $\mu g\ L^{-1}$) in mixtures using Poisson statistics to determine thresholds to identify beginning and end of NP signal events is developed. SP-ICP-MS with the µsDAQ and conventional pneumatic nebulization is used for the detection of Ag NPs in the presence of a significant concentration of ionic BG ($^{107}Ag^+$ up to 1 000 000 counts per second, cps). In contrast to a conventional decision criterion (three times standard deviation of the BG, $3\times SD_{BG}$, normal distribution), the NP ion cloud extraction method reported here is based on setting thresholds to determine the beginning and the end of an ion cloud using Poisson statistics, which is suitable for the low count data. The algorithm is exemplarily applied for the flagging and detection of Ag NPs in the presence of Ag^+. Two parameters, namely the critical level (false positive probability was set to 5%) and the detection limit (false positive and false negative probabilities were set to 5%) based on Poisson distribution are implemented to determine the thresholds. Different sets of the NP ion cloud extraction condition are used to verify the calculated thresholds. IN the future, the method can be universally applied for the detection of different elements with SP-ICP-MS.

Chapter 6 summarizes the results of this thesis and discusses future perspectives in the field of SP-ICP-MS.

Chapter 2

Single Particle ICP-MS – A Critical Review of the State-of-the-Art

Based on:

D. Mozhayeva, C. Engelhard, A Critical Review of Single Particle Inductively Coupled Plasma Mass Spectrometry – A Step Towards the Ideal Method for Nanomaterials Characterization,

J. Anal. At. Spectrom., 2019, DOI: 10.1039/C9JA00206E.

2.1 Introduction

2.1.1 Nanomaterials

Nanotechnology is a rapidly developing field of science, which utilizes materials and their properties at the nanometre (10^{-9} m) scale. The basic idea of nanotechnology has been formulated already in 1960 by Richard P. Feynman: "What would the properties of materials be if we could really arrange the atoms the way we want them?"[13] Indeed, materials at the nanometre scale possess unique properties different from those of the chemically identical bulk materials. The fact that matter has distinct size-dependent properties led to the development of colloid chemistry. The first systematic studies in this field were conducted by Michael Faraday, when he described the properties of "ruby" gold (Au) suspensions in 1857.[14] "The state of division of these particles must be extreme; they have not as yet been seen by any power of the microscope."[14] This statement is an evidence that the task to analyze Au NPs has been a challenge. The variety of states and properties of nanomaterials still presents a challenge for their characterization in analytical chemistry, even after more than 150 years after the term "colloid" has appeared.[15] The invention of electron microscopes in the 20th century has allowed to visualize nanomaterials (with at least one dimension of the size from 1 nm to 100 nm). Although the microscopy based techniques became prominent nanomaterials analysis tools, they possess some limitations. Namely, difficult sample preparation, limited area of analysis, and measurement of projections (not three-dimensional imaging). Therefore, alternative analysis methods are needed.

An alternative method for nanomaterials characterization is single particle inductively coupled plasma mass spectrometry (SP-ICP-MS, also referred to as spICP-MS or SP-ICPMS).[16] The technique utilizes a standard ICP-MS setup, and makes use of the time-resolved detection for analysis of NPs that are introduced in diluted suspensions one by one. Since the first publications, the field has grown rapidly (Figure 2.1) and, in the authors estimation, will continue to grow. There has been several reviews focusing on the topic of SP-ICP-MS[8-10, 17], discussing the principles, capabilities, limitations, and selected applications. The goal of this chapter is to critically discuss the latest developments and remaining challenges

of SP-ICP-MS and its metrology; to highlight instrumental parameters that are important for NPs detection and to summarize the latest applications of SP-ICP-MS when used with and without particle fractionation methods.

2.1.2 Principle and early development of SP-ICP-MS

The basic principle of SP-ICP-MS is that NPs can be individually detected if they are introduced in sufficiently diluted suspensions. When the signal is acquired in a time-resolved manner, NPs can be characterized on a particle-by-particle basis. Each NP then produces a short spike on the order of few hundreds of microseconds above the continuous BG[18]. The signal abundance is proportional to the mass of a NP. NP size can be calculated from NP mass if one assumes an element-specific NP density and geometry. The frequency of the detected spikes can be related to the PNC in the suspension. Overall, SP-ICP-MS allows to obtain NP average size, size distribution, and PNC after only a few minutes of measurement. The quantification and calibration strategies were summarized and described in detail before[8-10, 17], so they will be only shortly discussed below.

The first utilization of the ICP source for time-resolved particles analysis was published by H. Kawaguchi et al.[19]. In the paper, micrometer-sized particles were generated after the desolvation of monodisperse NaCl, $Ca(NO_3)_2$, and $Cu(NO_3)_2$ droplets. The method based on atomic emission spectroscopy (AES) detection was intended for analysis of particles in air. Later the same group adapted the technique to ICP-MS (the commercial detector was modified) to achieve 15 times lower mass detection limit (L_D) and detect femtogram amounts of zinc.[20] This method utilized monodisperse droplets of $Zn(CH_3COO)_2$ and $Pb(NO_3)_2$ suspensions that were dried to produce the particles for the introduction into the ICP-MS. Two years later it was shown that instrumental conditions significantly affect the resulting particle signal intensity.[21] Namely, the combination of radio frequency (RF) power, sampling positions, and carrier gas (also referred to as "nebulizer gas") flow determine the intensity of the signal. It was found that for Zn-containing particles 1400 W RF power, 14 mm sampling position, and 0.8 $L \cdot min^{-1}$ carrier gas flow were optimal for the particles detection; however, no

other elements or matrices were tested. The main application fields of the air aerosols analysis were predicted to be environmental studies (detection of contaminants in air) and control of clean environments (e.g. clean rooms in industrial application).[19-23] Later on the detection of particles was performed in suspensions with ICP-AES.[24, 25] Micrometer-sized particles of "refractory oxides and silicates"[25] were used for analysis. The authors pointed out that due to incomplete ionization, the response obtained for 3–7 µm silica particles was not proportional to the mass of the analytes. Furthermore, the mass calibration "still remains a problem" due to the absence of any particles (detectable by ICP-AES) with narrow size distributions.[25]

A feasibility study for colloid suspension analysis with SP-ICP-MS was published by C. Degueldre and P. Y. Favarger in 2003.[16] In the paper, the results of SP-ICP-MS with 10 ms dwell time for analysis of polydisperse 400 nm (median size) TiO_2, 150 nm Al_2O_3, 400 nm FeOOH, and some natural colloids were demonstrated. The choice of isotopes for detection was discussed in detail because of the mass interferences experienced by light elements in a single quadrupole ICP-MS (ICP-Q-MS), and $^{48}Ti^+$, $^{27}Al^+$, $^{57}Fe^+$, and $^{44}[SiO]^+$ were chosen for detection in a model water matrix. Similar studies were published by the same authors for 100 nm ZrO_2[26], manually milled ThO_2[27] and UO_2[28], and 80 to 250 nm Au particles.[29] The studies utilized the PNC of $10^5 – 10^6$ cm^{-3}, and the method was presented as an alternative to microscopy investigations.[16, 26-29]

After the first publications on SP-ICP-MS between 2003 and 2011, the total number of publications first doubled in 2012 (cf. Figure 2.1). According to a search in the Web of Science database, interest is steadily growing and over 300 peer-reviewed manuscripts on the topic are published today.

2.2 Towards the Ideal SP-ICP-MS Method

The title and the idea of the chapter were inspired by plenary lectures of Gary M. Hieftje[30, 31] and his publication dedicated to Howard Malmstadt in 2006.[12] Research ideas of Howard Malmstadt were reportedly following the concept of an

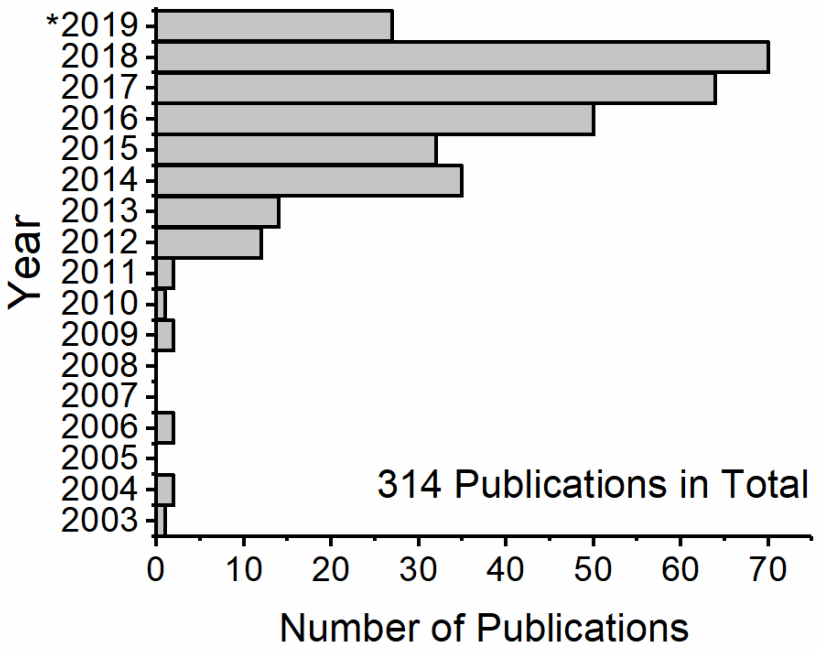

Figure 2.1: Number of SP-ICP-MS publications according to the Web of Science database (accessed on 28 May 2019). 314 publications in total. The search command: "SP-ICP-MS" OR "SP-ICPMS" OR "sp-ICPMS" OR "single particle ICPMS" OR "single particle ICP-MS" OR "single particle inductively coupled plasma mass spectrometry" OR "single particle inductively coupled plasma mass-spectrometry" (the characters are not register sensitive). Note that two publication published in 2004-2006, that do not use the above mentioned terms, were added manually.

*The results for 2019 are incomplete.

ideal. He was first defining the qualities of an ideal "concept, method, device, or system"; and the research was then aimed to overcome the identified weaknesses.[12]

In the same paper[12] the characteristics that "an ideal method for atomic spectroscopy" would have, were defined. These characteristics comprise, among others, L_D of a single atom, no spectral or matrix interferences, simultaneous multielemental detection, and standardless analysis.[12] The author would like to look at these ideal characteristics and compare them with the existing ones for SP-

ICP-MS and NPs analysis. This way the advances and capabilities of the method along with the limitations are reviewed, in order to evaluate future perspectives and directions of SP-ICP-MS.

2.2.1 Sample Preparation

"An ideal method for atomic spectroscopy" would require no sample preparation, and "ideally" liquid samples could be analyzed with SP-ICP-MS without any sample preparation. In reality, this can be done only for model solutions (and not for unknown samples); however, even then a lot of factors should be considered beforehand, especially when a significant amount of matrix is present, in order not to alter the state of NPs. Nanomaterials possess high surface energy that makes them more reactive compared to the bulk materials of the same composition; therefore, the stability of the NPs suspensions should be always considered during storage, handling, sample preservation, and sample preparation. Different dispersion media or dilutions, interactions with materials of the sampling or storage containers, storage conditions, and storage time may alter the surface coating or size of the NPs, and cause aggregation. Moreover, a certain PNC range is required for analysis to measure the NPs individually. The required PNC range for analysis is discussed here in detail, because it depends on many factors (nebulization and transport efficiency, type of the nebulizer and sample introduction system, elemental composition and size of the NPs etc.). If the samples are too diluted, measurement time can be increased to increase the number of detected particles. In some cases, matrix interferences can be reduced by sample dilution.

Nanomaterials often come in complex matrices (e.g. solid matrices, environmental and food samples) and require carefully optimized sample preparation protocols for their successful extraction and SP-ICP-MS analysis. In Table 2.2, all papers are listed that report sample preparation strategies for SP-ICP-MS sorted by type of matrix (e.g. animal tissue, cell cultures, body fluids, cosmetics etc.) and publication year. This table is intended to help the reader to

easily grasp the experimental details. In addition, the reader is advised that the main challenges of sample preparation were recently reviewed by others.[32, 33]

Clearly, in complex matrices it is important to consider that the state NPs may change due to filtering (NPs may interact with filter membranes), species interconversion (NPs may partially dissolve and form ionic species or ionic species can be reduced to corresponding metals), extraction and digestion procedures, or storage. At the current development stage, SP-ICP-MS is considered to be very suitable for the analysis of liquid samples without any sample preparation but only in the case of a rather simple matrix. In all other cases, a careful sample preparation method development is required for analysis of complex, in particular, solid matrices to ensure that NPs do not change in their size, form, or aggregation state.

2.2.2 Sample Introduction

In an ideal world, a sample introduction system would exist for SP-ICP-MS that features a 100% transport efficiency and a high tolerance to all kinds of different matrices. Today, commercially available nebulizers do not achieve a 100% particle transport efficiency, and, thus, the precise determination of the nebulizer transport efficiency is required for system calibration. Pneumatic nebulizers achieve only approximately 0.5 – 2% transport efficiency with 1 mL min^{-1} sample uptake rate.[34] The aerosol transport through a spray chamber is aimed to eliminate larger droplets, which helps to reduce the solvent load and to improve analyte signal stability, but at the same time a considerable amount of the analytes is also lost in the drain. An alternative to the high-flow pneumatic nebulizers (e.g. 1 mL min^{-1} sample uptake rate) are micronebulizers with considerably lower sample flow rates. With micronebulizers (e.g. at 10 µL min^{-1} sample uptake rate) the transport efficiency can be improved to 60 and 80%.[34] Micronebulizers utilize low-volume spray chambers (e.g. 15 cm^3) and help to improve the transport efficiency. For example, a transport efficiency of approximately 93% was reportedly achieved for 70 nm Pt NPs with a large-bore concentric nebulizer and a small-volume on-axis cylinder chamber.[35] A loss of 7% was discussed to be likely due to

adsorption to nebulizer and spray chamber walls, NPs surface charges, and assumptions made during PNC determination.[35] In general, the higher the sample flow of a nebulizer, the lower its transport efficiency typically is. However, the matrix tolerance decreases from higher toward lower sample uptake rates. Micronebulizers can be more difficult to operate and maintain due to the dimensions of the inlet capillary (e.g. 0.15 mm)[35], which might get obstructed, and sample interchange can also be tedious. When compared to standard pneumatic nebulizers; however, micronebulizers are considered to be advantageous in the field of SP-ICP-MS for low-volume samples, simple matrices, when they are used to interface separation devices, or to achieve lower PNC L_D.

Another approach to achieve high transport efficiency for NPs is through a microdroplet generator (MDG), where monodisperse droplets are generated by a piezoelectrically actuated quartz capillary.[36] The droplets with a controlled volume and speed of generation are transported into the ICP, and transport efficiency above 95% can be achieved.[37] The advantage of the MDG introduction is that calibration may be performed with dissolved metal standards, when reference materials of the NPs are not available.[37] Also, a combination of a pneumatic nebulizer and a MDG was recently reported as a means to exchange different sample matrixes faster and to calibrate the NP signal using traceable elemental standards without the need to use NP reference materials.[38] In this setup, the MDG was used for system calibration, and the pneumatic nebulizer was used for sample introduction.

A comparison of pneumatic nebulizers and MDG based sample introduction systems were performed in order to highlight advantages and disadvantages of the techniques for NPs quantification.[39, 40] It was found that losses are still possible at the sample introduction stage affecting both NPs and dissolved species. Future improvements of sample introduction system are still needed to ensure high NP and dissolved ion transport efficiency, robust operation, and a high tolerance toward different matrices.

2.2.3 NPs in the ICP Source

When NPs enter the ICP, they would ideally get fully vaporized and ionized, regardless of their elemental composition, size, and matrix they are in. However, it is important to consider differences in boiling points and ionization potentials of the elements the particles are made of because these might result in different optimal experimental conditions. For example, Ho et al. focused on the determination of the maximum signal intensity as a function of the ion sampling position (frequently referred to as "sampling depth") for different elements.[41] It was shown that different elements have a different signal maximum in their sampling position profiles depending on the combination of element ionization potentials and boiling points of the corresponding oxides. The maxima of sampling position profiles of 19 dissolved elements were determined in solution. The maxima of sampling position profiles vary from 3.8 mm ($^{60}Ni^+$, NiO boiling point is 2300 K) to 6.1 mm ($^{140}Ce^+$, Ce_2O_3 boiling point is 4000 K). Lower oxide boiling point results in lower sampling position maximum; however, some studied elements do not follow the trend, e.g. the signal maximum for $^{208}Pb^+$ was at 5 mm sampling position with PbO boiling point being 1800 K. Ionization potential alone does not have a clear effect on the position of the sampling position maximum. Therefore, a combination between the element ionization potential and particle vaporization (oxide boiling points) was considered. The sampling position maxima for elements with volatile oxides and relatively high ionization potentials (e.g. Ni, Cu, Zn, As, Cd, and Pb) are expected to occur after the complete dried aerosol vaporization. Elements such as Y, Zr, La, Ce, Gd, Ti, Al, Cr, Sr, and V have high oxide boiling points (above 3000 K) and are highly ionized in the plasma after their vaporization. "The position of maximum ICP-MS sensitivity, therefore, depends on the boiling point of the oxides for high-boiling oxides or the difference between the boiling point and the temperature for high degree of ionization for elements of high ionization potential and low-boiling oxides."[41] 150 nm and 250 nm Au and 80 nm ZrO_2 NPs were studied afterwards, and they were found to have different complete ionization positions (only around 0.5 mm) in the ICP compared to dissolved metals analysis (Figure 2.2).[41] Consequently, it is important to determine the position of the maximum signal in sampling position profiles for method optimization and

minimization of systematic errors, when calibration with dissolved metals is performed in SP-ICP-MS.

Incomplete ionization may occur due to a relatively larger mass of individual NPs, and, in turn, would lead to a limited upper size dynamic range for NP analysis. Additionally, matrix ions that reach the plasma together with the NPs may affect the ionization of the NPs. In order to study these processes, the effects of NPs or droplets on the plasma have been investigated by several groups, only selected recent papers are presented here. Kay Niemax and co-workers utilized a MDG to study atomization processes in the plasma.[42] They got the indications that the local plasma cooling occurs during atomization, and it is dependent on the analyte mass. Another finding was that the matrix elements in the droplets affect the droplets atomization. Later they confirmed experimentally that the position of atomization and ionization of analytes in the ICP strongly depends on the injector gas flow, the size of the introduced droplet, and also on the mass of the analyte.[43] Further experiments demonstrated the effect of analyte mass in particles on the position of analyte atomization. According to the calculations, if the injector gas flow is increasing from 0.14 to 0.5 L min^{-1}, then the temperature of the central plasma channel decreases, which may lead to a delay in the atomization depending on the properties of the analyte under investigation. Additionally, higher particle mass causes more significant plasma cooling, also leading to delayed atomization. It was also confirmed that the presence of matrix (SiO_2 particles in Ca^{2+} matrix) affects both particles and matrix components atomization. Namely, there was a delay in complete atomization of two 1.55 μm SiO_2 particle compared to one 0.83 μm SiO_2 particle that translates in "a spatial shift of about 8 mm in the ICP".[43] It has also been shown that the position of atomization and ionization is important for ion sampling. If the ions are sampled too early, when atomization and ionization are still not complete, then the detected signal per particle decreases. If the sampling is performed too late, then after the particles are ionized, diffusion occurs, and the signal per particle may also decrease.[34]

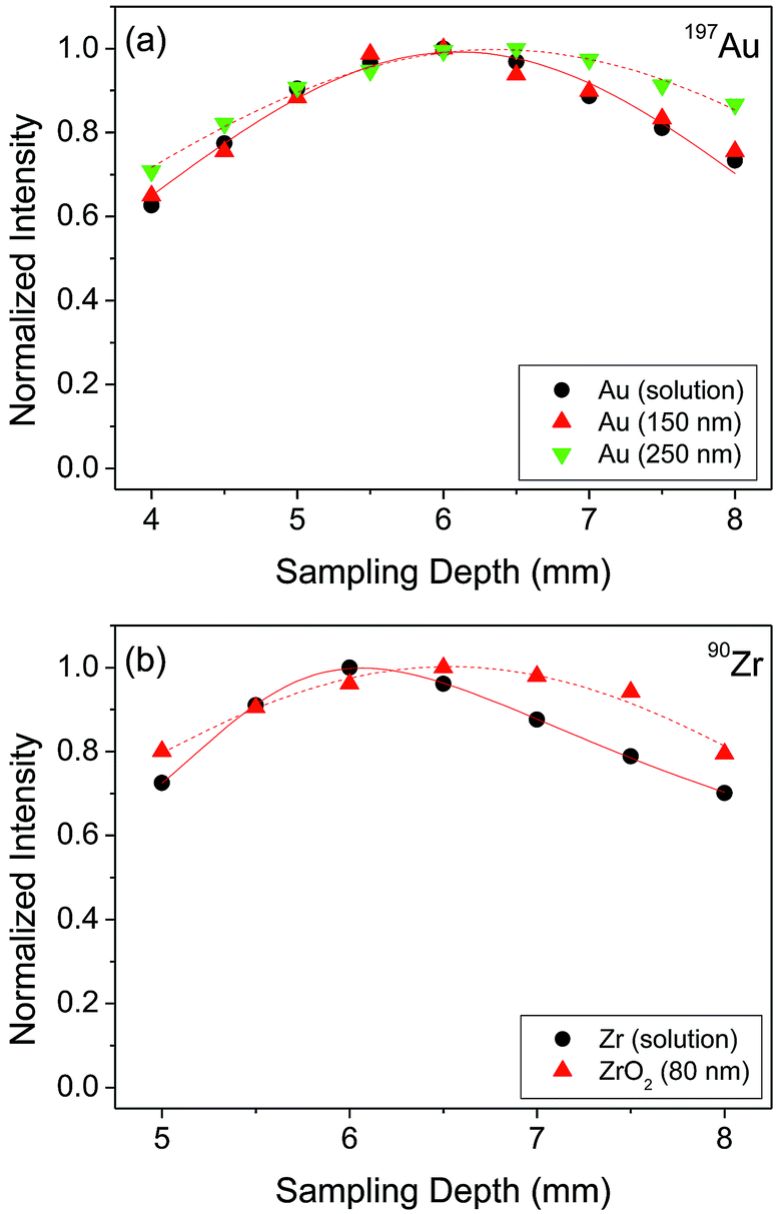

Figure 2.2: Sampling position profiles of (a) Au and (b) Zr in the form of aqueous solution of concentration of 10 µgL $^{-1}$ and discrete NPs. Reproduced from Ho et al. [41] with permission from The Royal Society of Chemistry, Copyright 2015.

Ho et al. performed a simulation study focusing on incomplete particle vaporization.[44] It was shown that it is important to know the point of complete particle ionization for ions sampling. For example, Au particles larger than 150 nm are not completely ionized, and, thus, the mass calibration levels off at higher mass

values (above 34 fg) at 8 mm sampling position. A sampling position upstream in the plasma (closer to the coil) resulted in an even narrower linear dynamic range for Au NPs detection (e.g. 6 mm in the simulations results in incomplete vaporization for Au NPs above 60 nm). Additionally, smaller NPs are subjected to diffusion to the higher extent, causing analyte losses for smaller particles that already completely vaporize early in the ICP. Therefore, it was pointed out that it is important to match the NPs masses used for calibration with the analyzed particles. A literature search[44] was done to determine the detected signal of the particles at which it is no longer proportional to the particles mass (100 nm for Ag NPs[40], 150 nm for Au NPs[44]); however, the influence of the detector linear dynamic range on the obtained values was not studied. O. Borovinskaya et al. demonstrated that droplets that are off the central axis of the plasma experience a temporal shift in their ICP-MS signals due to diffusion in the plasma.[45] A computational study confirmed the advantages of introducing the samples on-axis to achieve higher transport efficiencies of the ions into the MS.[46] G. Chan and G. Hieftje demonstrated that injection of droplets (deionized water) into the ICP causes a noticeable influence on it, the plasma is locally cooled (the cooling lasts more than 2 ms after the droplet leaves the load-coil) and is then reheated to the temperature above equilibrium (this effects lasts up to 4 ms after the droplet leaves the load coil); therefore, these effects last longer than the residence time of droplets in the plasma.[47] Here, the OH molecular band, Ar I and H I emission lines were measured with a monochromatic imaging spectrometer every 100 μs.

The studies presented in the paragraph above demonstrate that it is indeed important to optimize the plasma conditions for a precise and sensitive NPs detection. Namely, injector gas flow (only Ar and not He was considered in this review), plasma power, sampling position, and injector diameter should be optimized based on the analytes and matrix used. The effect of the ICP-MS sampling position on the signal intensity of Ag and Au NPs was studied.[48] It was shown that it is necessary to optimize the sampling position, because it can decrease the size L_D by 25 – 30% for the studied NPs compared to the standard instrument tuning procedure. E.g. the sampling position of 4 mm was found to be optimal for Ag and Au NPs to obtain the highest signal intensity, the signal of

dissolved silver and gold standards followed the same trend.[48] It is important to note that the optimal sampling position would be different for different instruments, the elements of the different mass ranges; and the formation rate of doubly charged ions and oxides should be accounted for some elements. K.-H. Chun et al. used a double-viewing-position single particle ICP-AES approach to study and select an appropriate sampling position.[49] The approach can be used to elucidate a potential incomplete ionization of particles, and, therefore, provide the information for SP-ICP-MS that sampling from these positions would not be suitable.

SP-ICP-MS is sensitive toward the plasma conditions, and more studies are required in this respect to develop robust protocols to establish optimal plasma conditions for different NPs and different matrices. The plasma conditions that were used in SP-ICP-MS application papers are summarized in Table 2.2 and discussed in the corresponding chapter. Apart from the choice of the nebulizer, torch injectors of smaller diameter may help to focus the NPs on a central axis (with low matrix load). The combination of the three parameters injector gas flow, plasma power, and sampling position significantly affect NPs ionization and, in turn, the recorded signals, and should be optimized prior to analyses. The aim is to achieve the conditions at which the ionization is complete for the required NP size range in a specific matrix, and to sample the ions into the MS from the point of complete ionization to avoid ion cloud diffusion in the plasma and a loss of ions per particle.

2.2.4 Ion Transport

All ion clouds produced in the ICP ideally would be transported into the MS. However, the step of ion extraction into the MS is associated with losses. The extraction takes place (for most of the commercial instruments) through the sampler and skimmer cones that help to reduce the pressure from atmospheric conditions in the ICP to vacuum conditions inside the MS. After sampling, positively charged ions should be separated from the negatively charged ones, neutrals, and electrons; and focused to proceed to a mass analyzer. Optimal ion

lenses voltages may differ from element to element, so the standard tuning is accustomed to determine only one set of voltages for the whole mass range. The maximum sensitivity for a particular ion may be achieved by fine tuning. Additionally, the generated ion beam is experiencing space-charge effects: A charge repulsion between ions of the same charge in the beam occurs, and this effect is particularly pronounced for lighter low-mass ions. The space charge effect may explain some matrix effects and why low-mass element have lower sensitivity, compared to higher-mass elements.[50] H. Niu and R.S. Houk[51] described fundamental aspects of ion extraction in ICP-MS, and highlighted that the understanding of the processes happening during the transport of the ion to a mass analyzer would help to reduce the ion losses at this stage.

The ion transport for NPs is associated with possible partial losses of the number of ions per NP that were generated in the plasma, partial losses of the BG ions, losses due to the extraction of positively charged ions, space charge effect, etc. All of these losses increase the size L_D for NPs and decrease the overall instrument sensitivity.

2.2.5 Mass Analyzers

The ideal mass analyzer for NPs would be able to have a high mass resolution to provide isotopic information along with simultaneous rapid multi-elemental detection of short (few hundreds of microseconds)[18] NP signals. The mass analyzers that are available nowadays are suitable for different types of applications and still have some room for improvement.

ICP-Q-MS are widely used because of their comparatively low cost and capability for fast NP detection. However, ICP-Q-MS instruments are limited in terms of multielemental detection and resolution (typically one m/z unit). ICP-Q-MS is a sequential instrument, where a certain set of voltages is used for each m/z. Therefore, switching between different m/z ratios requires some settling time (on the order of 100 μs)[52] for the new set of parameters to be stable. This settling time leads to only partial detection of fast transient NP signals, when more than one isotope is detected in one measurement, which significantly limits the amount of

counts detected per NP. A proof-of-principle for two elements detection was demonstrated, where Au/Ag core/shell NPs were detected with 100 µs dwell time and 100 µs settling time.[52] A partial solution to this multielemental quadrupole limitation would be analysis of different m/z one after the other, if the amount of the sample is sufficient. Another limitation of ICP-Q-MS stemming from its comparatively low mass resolution is interferences. A lot of elements experience interferences in ICP-Q-MS[53], especially in the presence of matrix. If the interfering ion is present only as the BG and not in the form of NPs, then NPs could still be detected to a certain extent as spikes above the continuous BG. However, as the variation of the BG signal rises with the increasing signal level[54, 55], the NP size L_D rapidly increases (from 18 nm to 32 nm for Ag NPs, when 0.3 µg L^{-1} Ag^+ was added, 5 ms dwell time)[7]. One approach to remove the interference may be the use of collision-reaction cell with kinetic energy discrimination, e.g. it helped to reduce the sensitivity of the instrument to detect Au NPs up to 200-250 nm in diameter.[56, 57] After passing through the mass analyzer, the ion detection itself is performed usually by discrete dynode electron multiplier. The crucial parameter to set is the detector dwell time, which will be discussed in the next subchapter. In spite of all limitations, ICP-Q-MS is still the most widely used instrument for NPs detection.

The utilization of triple quadrupole (TQ) technology allows to overcome matrix interferences. The use of CH_3F or H_2 for reactions/collisions allowed to quantify SiO_2 NPs (high natural BG of N_2) in the range from 80 to 400 nm.[58] TiO_2 NPs can be quantified with the use of NH_3 as the reaction gas in candy products[59] and water matrices with high Ca content[60] ($^{48}Ca^+$ causes interference with the most abundant $^{48}Ti^+$ isotope). Sector field (SF)-ICP-MS has a higher mass resolution and sensitivity compared to ICP-Q-MS and can also be used for NPs detection.[37, 60-66] In particular, the method was used to distinguish $^{48}Ti^+$ (m/z = 47.948) and $^{48}Ca^+$ (m/z = 47.953).[60]

The feasibility of SP-ICP-MS for isotope analysis in erbium oxide particles was demonstrated with multi-collector (MC)-ICP-MS.[67] Isotope dilution analysis was introduced for Ag NPs analysis and quantification with ICP-Q-MS.[68, 69] Here, spikes of isotopically enriched $^{109}Ag^+$ solution were introduced for quantification.

Quasi-simultaneous multielemental analysis can be performed with time-of-flight ICP-MS (ICP-TOF-MS).[70] The prototype instrument was able to acquire a mass spectrum each 30 kHz; however, the size L_D were 46, 32, and 22 nm for Ag, Au, and U NPs respectively (higher than in ICP-Q-MS[40, 71, 72]). The commercial instrument allows to perform the analysis of e.g. Au/Ag core/shell NPs and distinguish them from Ag NPs with improved 19 and 27 nm L_D for Au and Au NPs respectively (Poisson statistics).[73] ICP-TOF-MS allows to distinguish between natural and engineered CeO_2 NPs[74] and TiO_2 NPs[75]. The commercial ICP-TOF-MS is reported to achieve 29, 14, and 7 nm L_D for Ti, Mo, and Au containing NPs respectively.[76] It was used, for instance, for Bi containing NPs and NPs of steel to obtain the elemental composition of this industrial materials.[76]

2.2.6 Detector Dwell Time

Ideally, SP-ICP-MS requires fast time-resolved detection to get accurate information (number of counts) for each detected NP over the whole required length of the measurement. Here we focus mainly on secondary electron multiplier detectors (most frequently used for ICP-Q-MS). Usually the detection occurs sequentially during the intervals called dwell times. Dwell times in the millisecond time range are the most frequently used (Table 2.2, also determined by the available settings of the instruments). As it was mentioned and confirmed earlier[18], NPs represent the ion cloud events in the range of few hundreds of microseconds. Additionally, dead time between dwell times may be present[16] and interrupt the time-resolved measurements causing partial losses of counts per particle. The occurrence of NPs between two dwells may cause one NP to be detected as two smaller ones, and with high PNC two or more particles may fall into one dwell time. Therefore, with millisecond dwell times, it is important to obtain a suitable PNC for measurements, because only one point is detected per NP. SP-ICP-MS can be performed with millisecond time resolution, however, more care should be taken to choose suitable PNC.

An approach to overcome the measurement artifacts is to use integration times that are significantly shorter than the duration of NPs ion clouds (in the

microsecond time scale). This way time-resolved profiles of the NP ion clouds could be obtained. The main challenge arises then in the data acquisition, storage, and handling. For example, if the dwell time would be 10 µs, then each 1 s 100,000 data points are obtained. Therefore, most of the systems require a special data processing for visualization and quantification. The signal per NP can then be obtained by the sum of the counts obtained for each detected NP (profile). The extraction of the NP ion clouds and their distinction from the BG play an important role in this case. To the best of authors´ knowledge, the first system for time-resolved particles analysis with ICP-MS was presented by T. Nomizu et al. in 2002.[23] The detection was performed with 20 µs time resolution for 1 min in the pulse-counting mode; however, it is stated that the measurement time was limited only by the computer hard disc space. Later, a system that allows data acquisition with up to 10 µs dwell times with no settling time between the dwells was introduced.[52, 77, 78] The NPs were extracted from the BG by applying a $3\times SD_{BG}$ criterion.[52] A system allowing to achieve up to 5 µs time resolution with continuous data acquisition was also developed.[11] The system allows to perform the acquisition for any measurement length (only limited by the hard disk space). It was used for continuous measurements of up to 60 min with the coupling of a separation technique.[18] The obtained data was processed by setting the thresholds to begin and end the extraction of an ion cloud.[11] SF-ICP-MS has also been used for the continuous data acquisition up to each 10 µs.[61, 62, 65, 66] The NPs were determined in the data by finding the peak maxima above a certain threshold.[61, 66] An additional peak recognition algorithm using 100 µs dwell time based on cluster detection has been also introduced.[62] Another mass analyzer, ICP-TOF-MS can be operated with up to 30 kHz to assure fast detection of NPs.[70]

First attempts have been done to distinguish NPs with different shapes and high aspect ratios. Microseconds time resolution was implemented to distinguish spherical NPs from nanorods and dimensional characterization of the NPs based on their ion cloud signal duration.[79] The composition of NPs of gold and silver alloys has been also assessed using profiles of the ion clouds.[80] The detection of silica colloids, which otherwise would require the use of a collision gas to remove

polyatomic interferences (from nitrogen dimer ions), has been simplified with microsecond time resolution detection.[81]

With microsecond time resolution, the BG is divided between adjacent dwells[11, 78], so the detection of NPs is possible in the wider range of PNCs and in the presence of higher BG and dissolved ions concentrations. It should be also noted that the data obtained with microsecond time resolution represent in most of the cases only several counts per dwell time (with 5-10 μs dwell times), so the Normal distribution statistics may not apply to this data, and Poisson statistics should be considered in order to differentiate NPs from the BG.[82]

2.2.7 Quantification Considerations

The principles of quantification with SP-ICP-MS were described in previous reviews in detail.[8-10] Briefly, in order to obtain particle size and size distributions with a pneumatic nebulizer, quantification can be performed using NPs standards of the same elemental composition or dissolved standards solutions of the element after taking into account the nebulization efficiency. The PNC determination requires a NP standard with the known PNC of the same element, or of a different element, if the same transport and nebulization efficiencies are assumed. The main limitations today is the fact that only a limited variety of the NPs standards of different composition and certified PNC exists[10], and difficulties in determination of the nebulization efficiency can occur.[83] Interlaboratory studies have shown that the determination of median particle diameter (2 – 5% repeatability SD, 15 –25% reproducibility SD) is much more repeatable and reproducible compared to the determination of PNC (7 – 18% repeatability SD, 70 –90% reproducibility SD). The lack of stability of the NPs in initial suspensions and different matrices depending on the handling and storage conditions may have a significant contribution to this fact.[83, 84] Recently, a metrological study assessing the determination and validation of Au NP size and size distribution was performed.[85] High-resolution scanning electron microscopy was used as one of the methods to validate the results obtained with SP-ICP-MS. Two methods show a good agreement with relative precision of 0.5%. It was emphasized that the NP size characterization provided by their

suppliers is not enough, and more characterization is needed, if the NPs are intended to be used in research. MDG[37-39], isotope dilution[68, 69], and flow injection[86, 87] allow to introduce new quantification approaches. However, still more studies on the metrology of the method are required to ensure accurate NPs analysis.

The counting stage of the electron multiplier is typically used up until 2×10^6 cps[34] because there is a detector dead time (in the order of 50 ns)[11] between the acquisitions caused by detector construction limitations. Because NPs result in short but intense ion signals, some of the counts per NP are lost due to the dead time (e.g. 6.2% for 40 nm and 24.4% for 60 nm Au NPs).[11] This phenomenon leads to a limited linear dynamic range (LDR) for NPs size detection. J. Liu et al. extended the LDR for Au NPs from 10 to 70 nm in "highest sensitivity mode" to 200 nm in "less sensitive modes".[56] The solution is to decrease the temporal signal of the NPs by the use of low extraction voltage[56] or collision-reaction cell.[56, 57] The effect of the plasma conditions on the LDR for Au NPs was investigated by W. - W. Lee and W.-T. Chan, 250 nm Au NPs were outside of the LDR.[88]

The size L_D depend on the sensitivity of the instrument, and the ideal L_D of one atom cannot be achieved nowadays with the current ICP-MS systems. The main reasons are a low nebulization efficiency, low ionization efficiencies of some elements in the argon plasma, and ion transfer into and inside the mass spectrometer. S. Lee et al. calculated the size L_D for 40 elements for an ICP-Q-MS.[72] Most of the elements still have L_D well above 10 nm[8, 72] that are quite high to assess the whole nanoscale from 1 to 100 nm.

PNC and size L_D both are based on a statistical evaluation of the data; therefore, data processing plays an important role in SP-ICP-MS. For millisecond time resolution, the size L_D is usually determined as $3\times SD_{BG}$ or $5\times SD_{BG}$ above the BG.[71, 89] Real world samples may have higher size L_D due to a continuous BG. If the blank is well known and no NP events are detected, then the PNC L_D was proposed to be three detected NP events by F. Laborda et al.[89] based on the L. A. Currie Poisson-Normal approximation ($2.71 + 3.29\sqrt{SD_{BG}}$ for a "well-known" blank). This PNC L_D may need recalculation, if some NP events are detected even

in blanks. The data obtained with microsecond time resolution usually requires even more data processing, because each NP is presented by several data points. Until now, there is still no established approach to extract NPs from the raw data, and each developed system utilizes its own algorithm (discussed in the previous chapter). Therefore, there is still a need to develop statistical approaches based on counting statistics for the quantitative extraction of NPs from the time-resolved data.

Another issue in NPs quantification is the differentiation of NPs from the BG. The continuous BG in ICP-MS may arise from dissolved ions, natural BG, or interferences. Bi et al. proposed an approach to differentiate NPs from the BG with the use of K-means clustering to improve the differentiation of the NPs from the BG compared to "traditional standard deviation approach".[90] G. Cornelis and M. Hassellöv developed an approach for data deconvolution taking into the account the noise components of the ICP-MS to differentiate the NP that are not fully resolved from the BG.[91] An approach that utilizes modelling of the BG based on the noise components with Monte Carlo simulation was developed for the data obtained with ICP-TOF-MS with 200 Hz resolution.[92] The method allows to distinguish small NPs from the BG, and the decision criteria for NP detection were revisited. Alternatively, dissolved ions can be removed with ion exchange resins[93] or the samples can be analyzed after dilutions.[94]

2.2.8 Coupling of SP-ICP-MS to Separation Techniques

A promising tool to obtain more information about the mixtures of NPs is the online coupling of SP-ICP-MS to a separation technique. As SP-ICP-MS is used for NPs size and size distribution determination, different separation techniques allow to get complimentary information about NPs. However, the main challenge is that SP-ICP-MS requires discrete detection of each NP, and separation techniques are usually based on local preconcentration of the analytes of a certain type. Additionally, separation techniques usually require a separation medium (mainly organic compounds), that is introduced into the ICP-MS and may cause

matrix effects. Therefore, the couplings require a careful method development to ensure that:

- the NPs are separated based on their properties but not focused to the extent that the detection of single NPs is significantly hindered;
- the organic buffer does not interfere with the NPs detection (instrumental parameters optimization);
- the suitable dwell time is chosen;
- the NPs do not undergo size transformations during the separation;
- the best size and PNC L_D are achieved.

An overview of the separation techniques that were coupled online to SP-ICP-MS is presented in Table 2.1, and the main features are highlighted. The first online coupling of SP-ICP-MS to hydrodynamic chromatography (HDC) was presented by S. A. Pergantis et al. in 2012, where Au NPs were separated by their size.[95] Later on in 2016, SP-ICP-MS was coupled online to field-flow fractionation (FFF) to fractionate the NPs by their size and also core-shell NPs (Ag core with SiO_2 shell) from mono-component NPs (Ag NPs).[96] Electrospray-differential mobility analysis (ES-DMA) was also coupled online to SP-ICP-MS.[97] This method allows to distinguish different sizes of NPs and assess their aggregation. The coupling of CE to SP-ICP-MS[98] allows to separate the NPs not only by their size, but also in some cases to separate NPs with different coatings.[99] According to Table 2.1, most of the separation method utilize surfactants, most commonly sodium dodecyl sulfate (SDS), to enhance the separation of NPs from each other. The coupling of separation techniques online to SP-ICP-MS has the potential to answer non-trivial questions in NPs mixtures analysis, where SP-ICP-MS alone does not provide sufficient information.

Table 2.1: An overview of the techniques coupled online to SP-ICP-MS for NPs analysis.

Technique coupled online	Analytes	Nebulizer and spray chamber	Plasma parameters	Dwell time	Separation features	Reference
CE	10, 20, 30, 40, 60 nm citrate-coated Au NPs	Microflow nebulizer with low volume spray chamber	RF power 1500 W, cooling gas 15 L min^{-1}, auxiliary gas 1 L min^{-1}, nebulizer gas 0.8 L min^{-1}, sampling position 7 mm	2 ms	70 mM SDS, 10 mM CAPS at pH 10 buffer	[98]
CE	20, 40, 60 nm citrate-coated Ag NPs	Microflow nebulizer with low volume spray chamber	RF power 1450 W, cooling gas 14 L min^{-1}, auxiliary gas 0.8 L min^{-1}, nebulizer gas 0.8 L min^{-1}, sampling position 3.5 mm	5 μs	60 mM SDS, 10 mM CAPS at pH 10 buffer, online preconcentration	[18]

Table 2.1: Continued.

Technique coupled online	Analytes	Nebulizer and spray chamber	Plasma parameters	Dwell time	Separation features	Reference
CE	20, 40, and 60 nm citrate-coated; 20, 40, and 60 nm PVP-coated; 40 and 60 nm PEG-coated; 40 nm BPEI-coated Ag NPs	Microflow nebulizer with low volume spray chamber	RF power 1450 W, cooling gas 14 L min^{-1}, auxiliary gas 0.8 L min^{-1}, nebulizer gas 0.8 L min^{-1}, sampling position 3.5 mm	5 µs	60 mM SDS, 10 mM CAPS at pH 10 buffer, online preconcentration, separation of NPs with different coatings	[99]
ES-DMA	30, 40, 60, 80, 100 nm Au NPs	n/s	n/s	10 ms	Ammonium acetate was used for electrospray, aggregates detection	[97]

Table 2.1: Continued.

Technique coupled online	Analytes	Nebulizer and spray chamber	Plasma parameters	Dwell time	Separation features	Reference
FFF	40, 60, 80, 100 nm citrate-coated Ag NPs, 60 nm citrate coated Au NPs, 51 nm Ag core and 21.6 nm SiO_2 shell citrate-coated NPs	Concentric nebulizer with cyclonic spray chamber	Nebulizer gas 0.88-0.96 L min^{-1}	5 ms	10 kDa regenerated cellulose membrane, 0.02% FL-70 carrier, separation of Au/SiO_2 core/shell NPs from Au NPs	[96]

Table 2.1: Continued.

Technique coupled online	Analytes	Nebulizer and spray chamber	Plasma parameters	Dwell time	Separation features	Reference
FFF	AgPURE® (<20 nm polyoxyethylene fatty acid ester-coated) in food simulants (water, 10% ethanol, 3% acetic acid) extracted from model films	Concentric nebulizer with cyclonic spray chamber	RF power 1550 W, cooling gas 14 L min^{-1}, auxiliary gas 0.8 L min^{-1}, nebulizer gas 1 L min^{-1}	5 ms	10 kDa regenerated cellulose membrane, ultrapure water as mobile phase	[100]
HDC	30, 60, 80, 100 nm citrate-coated Au NPs	V-groove nebulizer with double pass Scott spray chamber	n/s	10 ms	10 mM SDS at pH 11 eluent	[95]

Table 2.1: Continued.

Technique coupled online	Analytes	Nebulizer and spray chamber	Plasma parameters	Dwell time	Separation features	Reference
HDC	10, 30, 50, 100, 150, 250 nm citrate-coated Au NPs	PTFE spray chamber	RF power 1400 W, auxiliary gas 0.82 L min^{-1}, nebulizer gas 0.78 L min^{-1}, sampling position 40 mm	5 ms	2 mM Na_2PO_4, 60 mM formaldehyde, 1.8 mM SDS, 3.2 mM Brij L23, 3.2 mM Triton X-100 at pH 7.5-8 eluent	[101]
HDC	40, 80 nm Ag NPs spiked in Milli Q water, WWTP influents and effluents	n/s	n/s	100 µs	1 mM $NaNO_3$, 0.0013% w/w SDS, 0.0013% w/w Triton X-100 at pH 7.5 eluent	[102]

Abbreviations: BPEI – branched polyethylenimine, CAPS – 3-cyclohexylamoniuopropanesulfonic acid, CE – capillary electrophoresis, ES-DMA – electrospray-differential mobility analysis, FFF – field flow fractionation, HDC – hydrodynamic chromatography, n/s – not specified, PEG – polyethylene glycol, PTFE – polytetrafluoroethylene, PVP – polyvinylpyrrolidone, RF – radio frequency, SDS – sodium dodecyl sulfate, WWTP – waste water treatment plant.

2.3 Applications of SP-ICP-MS

There has been a significant increase in the number of published studies that utilize SP-ICP-MS in recent years (Figure 2.1) and the majority of these publications is dedicated to applications thereof. Table 2.2 summarizes the papers that include applications of SP-ICP-MS for analysis of different samples and different matrices (note that fundamental studies on SP-ICP-MS are not included). This table was compiled after a search was conducted in the Web of Science database with the following command: "SP-ICP-MS" OR "SP-ICPMS" OR "sp-ICPMS" OR "single particle ICPMS" OR "single particle ICP-MS" OR "single particle inductively coupled plasma mass spectrometry" OR "single particle inductively coupled plasma mass-spectrometry" (the characters are not register sensitive). The articles in Table 2.2 are grouped by the analysis matrix and then sorted by the year of publication. The Table 2.2 is a summary of the articles with a short description of the sample treatment and selected instrumental parameters. The reader is advised to check the original publications for more details.

It became apparent when compiling this table, that many publications do not include all experimental conditions that the author of this review considers important for SP-ICP-MS. As it was discussed above, the combination of RF power, sampling position, and carrier gas flow is crucial for best SP-ICP-MS performance. The parameters: dwell time and measured isotopes are very important as well. Most of the article state the dwell time that was used for the measurements, with microsecond time resolution (most frequently 0.1 ms dwell time) becoming more widely used in the last years. The majority of the articles do not include the sampling position or injector diameter in the experimental descriptions. Some articles cite their previous works and do not cite the exact conditions that were used for the study. The author would like to draw the attention of the younger and upcoming generation of scientists to this situation and encourage them to include more experimental details and conditions in their manuscripts to ensure the transparency of scientific research.

The majority of the SP-ICP-MS application papers (Table 2.2) utilize a method for direct analysis of aqueous media (exposure media, model and real

environmental water samples, etc.) with or without dilution. Dilution is an effective tool to reduce the matrix load. A filtration step is introduced frequently to avoid clogging of the nebulizer; however, this step may lead to partial loses of NPs due to interactions with the filter membrane materials, even if the NPs are smaller than the membrane pores.[103] Therefore, more research is required to determine suitable filter materials for NPs with different coating to reduce these interactions or identify membranes that show a somewhat reproducible adsorption behavior. When enzymatic or alkaline digestions are used for more complex matrices (tissue, plants, etc.), care must be taken to ensure that the NPs keep their initial state after these procedures. The ultimate goal of any sample preparation step must be a high particle recovery rate and little to no species transformation.

Table 2.2: Summary of peer-reviewed SP-ICP-MS nanoanalysis papers with selected experimental conditions, sample matrix, and particle size detection limit.

Year	NP types analyzed	Matrix	Sample preparation	Nebulizer and spray chamber	Plasma parameters	Mass analyzer	Measured isotopes	Dwell time	Size L_D (ESD)	Features	Reference
Animal Tissue											
2012	<20 nm NM-300K or <15 nm PVP-coated Ag NPs	Rat tissue	Enzymatic digestion with proteinase K	Babington nebulizer	RF power 1400 W	Q	$^{107}Ag^+$, $^{109}Ag^+$	3 ms	20 nm	Oral exposure to rats over a period of 28 days	104
2013	30, 80, 1500 nm Ag NPs powders, 30, 70 nm PVP-coated Ag NPs	*Lumbriculus variegatus* tissue	Sonication with water and 0.45 µm filtering	n/s	n/s	Q	n/s	n/s	n/s	NPs detected in tissue even after 48 h depuration	105
2013	100 nm PVP-coated Au NPs, 60 and 100 nm PVP-coated Ag NPs	Spiked ground beef, *Daphnia magna*, *Lumbriculus variegatus* tissues, aqueous samples	Alkaline digestion with TMAH	Glass nebulizer, cyclonic spray chamber	n/s	Q	n/s	10 ms	n/s		106
2013	Ag nanowires with PVP or aluminium doped SiO_2 coatings	*Daphnia magna* hemolymph, aqueous samples	Dilutions, where necessary	n/s	n/s	Q	$^{107}Ag^+$, $^{197}Au^+$	10 ms	<30 nm ESD		107

Table 2.2: Continued.

Year	NP types analyzed	Matrix	Sample preparation	Nebulizer and spray chamber	Plasma parameters	Mass analyzer	Measured isotopes	Dwell time	Size L_D (ESD)	Features	Reference
2014	60 nm Au NPs	Rat tissue	Alkaline TMAH digestion and enzymatic digestion with proteinase K	MicroFlow PFA nebulizer, cyclonic spray chamber	RF power 1550 W, cooling gas 14 L min^{-1}, auxiliary gas 0.8 L min^{-1}, nebulizer gas 0.96-0.99 L min^{-1}	Q	$^{197}Au^{+}$	3 ms	Only NPs >44 nm were considered	Intravenous administration of the NPs	108
2014	60 nm citrate-coated Ag NPs	Spiked chicken meat	Enzymatic digestion with proteinase K	Conical glass concentric nebulizer, quartz impact bead spray chamber	RF power 1400 W, cooling gas 13 L min^{-1}, auxiliary gas 0.7 L min^{-1}, nebulizer gas 1.1 L min^{-1}	Q	$^{107}Ag^{+}$	3 ms	n/s		109
2014	<25 nm anatase TiO_2	Rat spleen	Enzymatic digestion with proteinase K	PFA micronebulizer, heated cyclonic spray chamber, desolvation system	n/s	Q	$^{49}Ti^{+}$	3 ms	n/s	Oral exposure	110

Table 2.2: Continued.

Year	NP types analyzed	Matrix	Sample preparation	Nebulizer and spray chamber	Plasma parameters	Mass analyzer	Measured isotopes	Dwell time	Size L_D (ESD)	Features	Reference
2015	50 nm PVP-coated Ag NPs	Earthworms tissue	Enzymatic digestion with proteinase K	Conical glass concentric nebulizer, quartz impact bead spray chamber	RF power 1400 W, cooling gas 13 L min^{-1}, auxiliary gas 0.7 L min^{-1}, nebulizer gas 1.1 L min^{-1}	Q	$^{107}Ag^{+}$	3 ms	30 nm	In vivo exposure in soil	111
2015	42 nm PVP-coated Ag NPs	Spiked chicken meat	Reference to previous studies	Reference to previous studies	Reference to previous studies	n/s	n/s	n/s	n/s	Two laboratories carried out the analysis with different methods	112
2017	18-20 nm Ag NPs	Mouse maternal tissues, placentas, foetuses	Alkaline digestion with TMAH	Quartz concentric nebulizer, cyclonic spray chamber	n/s	Q	$^{107}Ag^{+}$	0.1 ms	13 nm	Nose-only inhalation of a NPs aerosol for pregnant mouse females	113

Table 2.2: Continued.

Year	NP types analyzed	Matrix	Sample preparation	Nebulizer and spray chamber	Plasma parameters	Mass analyzer	Measured isotopes	Dwell time	Size L_D (ESD)	Features	Reference
2017	20 nm PVP-coated Ag NPs	Hens livers and yolks	Enzymatic digestion with proteinase K	n/s	RF power 1000 W, cooling gas 15 L min^{-1}, auxiliary gas 1.2 L min^{-1}, nebulizer gas 1.1 L min^{-1}	SF mass analyzer was used in low resolution mode	$^{109}Ag^{+}$	2 ms	10 nm	Oral administration to hens	114
2017	30, 60 nm Au NPs	*Caenorhabditis elegans* nematode	Alkaline digestion with TMAH	C-type nebulizer, impact bead spray chamber	n/s	Q	$^{197}Au^{+}$	10 ms	n/s	Sucrose density gradient centrifugation was used to remove non-ingested NPs	115
2017	40 to 750 nm Pb NPs	Game meat	Enzymatic digestion with proteinase K	Low-flow concentric nebulizer, cyclonic spray chamber	RF power 1550 W, cooling gas 14 L min^{-1}, auxiliary gas 0.65 L min^{-1}, nebulizer gas 1.10 L min^{-1}	Q	$^{208}Pb^{+}$	5 ms	40 to 80 nm	Lead from the bullets; size L_D was reported to depend on the lead background	116

Table 2.2: Continued.

Year	NP types analyzed	Matrix	Sample preparation	Nebulizer and spray chamber	Plasma parameters	Mass analyzer	Measured isotopes	Dwell time	Size L_D (ESD)	Features	Reference
2017	26 nm Ag NPs	Chicken meat paste after in vitro model saliva, gastric, intestinal digestions	Dilution of digest extracts	MicroMist nebulizer, Scott-type spray chamber	RF power 1500 W, cooling gas 15 L min^{-1}, auxiliary gas 0.73 L min^{-1}, nebulizer gas 0.68 L min^{-1} (these conditions specified only for total silver analysis)	Q	$^{107}Ag^{+}$	10 ms	n/s		117
2017	15 to 75 nm PVP-coated Ag NPs	Spiked chicken muscle meat	Enzymatic digestion with proteinase K	Varied among the participants	Varied among the participants	Q or n/s	n/s	3 ms	15-20 nm	Interlaboratory method performance study with over 10 laboratories	83
2017	60, 80 nm Au NPs	LA-SP-ICP-MS imaging of mice heart, lung, spleen, liver, kidney	Intravenous injection	n/s	RF power 1400 W, nebulizer gas 0.7 L min^{-1}	Q	$^{197}Au^{+}$	1 ms	n/s		118

Table 2.2: Continued.

Year	NP types analyzed	Matrix	Sample preparation	Nebulizer and spray chamber	Plasma parameters	Mass analyzer	Measured isotopes	Dwell time	Size L_D (ESD)	Features	Reference
2018	CeO_2 NPs	Liver and lungs tissue of female mice	Enzymatic digestion with proteinase K	Low-flow concentric nebulizer, cyclonic spray chamber	RF power 1550 W, cooling gas 14 L min^{-1}, auxiliary gas 0.8 L min^{-1}, nebulizer gas 1.1 L min^{-1}	Q	$^{140}Ce^+$	3 ms	18 nm	Intravenous injection of NPs; no NPs in liver were detected after oral exposure	119
2018	30, 80 nm PVP-coated Ag and Au NPs	Liver, gill, intestine tissue of zebrafish (*Danio rerio*), aqueous samples	Alkaline digestion with TMAH	n/s	RF power 1550 W, nebulizer gas 1.14 L min^{-1}, sampling position 8.0 mm	Q	$^{107}Ag^+$, $^{197}Au^+$	1 ms	n/s		120
2018	50, 100 nm rutile TiO_2 NPs	Bivalve mollusk	Ultrasound assisted enzymatic digestion with pancreatine and lipase mixture	Glass concentric or PFA nebulizer (n/s clearly), cyclonic spray chamber	RF power 1600 W, cooling gas 16 L min^{-1}, auxiliary gas 1.2 L min^{-1}, nebulizer gas 0.95 L min^{-1}	Q	$^{49}Ti^+$	0.1 ms	24.4 - 30.4 nm		121

Table 2.2: Continued.

Year	NP types analyzed	Matrix	Sample preparation	Nebulizer and spray chamber	Plasma parameters	Mass analyzer	Measured isotopes	Dwell time	Size L_D (ESD)	Features	Reference
2018	TiO_2 and CeO_2 NPs	Spiked zebrafish (*Danio rerio*) (intestine, liver, gills, brain)	Enzymatic digestion with proteinase K, H_2O_2 treatment, SDS stabilization	Conical glass nebulizer, impact bead spray chamber	RF power 1400 W, cooling gas 13 L min^{-1}, auxiliary gas 0.7 L min^{-1}, nebulizer gas 1.1 L min^{-1}	Q	$^{48}Ti^+$, $^{140}Ce^+$	3 ms	100 nm TiO_2, 30-40 nm CeO_2	Method for NP extraction from tissue was optimized	122
Biological Applications											
2009	20, 40, 80 nm Au NPs	Immunoassay with NPs as tags to antibody	2% HNO_3 to release the tags, dilution	Glass concentric nebulizer, impact bead spray chamber	RF power 1400 W, cooling gas 13 L min^{-1}, auxiliary gas 0.8 L min^{-1}, nebulizer gas 0.85 L min^{-1}	Q	$^{197}Au^+$	10 ms	15 nm		123

Table 2.2: Continued.

Year	NP types analyzed	Matrix	Sample preparation	Nebulizer and spray chamber	Plasma parameters	Mass analyzer	Measured isotopes	Dwell time	Size L_D (ESD)	Features	Reference
2014	25 nm Au, 25 nm Ag, 20 nm Pt citrate-coated NPs	Multiplex DNA assay with NP tags	Melting wash, dilution	n/s	RF power 1200 W, cooling gas 13 L min^{-1}, auxiliary gas 0.8 L min^{-1}, nebulizer gas 0.82 L min^{-1}	Q	$^{107}Ag^+$, $^{197}Au^+$, $^{195}Pt^+$	0.5 ms			124
2015	80 nm citrate-coated Au NPs	Primary human umbilical vein endothelial cells	Alkaline digestion with TMAH	MicroFlow PFA nebulizer, cyclonic spray chamber	RF power 1550 W, cooling gas 14 L min^{-1}, auxiliary gas 0.8 L min^{-1}, nebulizer gas 0.96-0.99 L min^{-1}	Q	$^{197}Au^+$	10 ms	n/s		125
2016	7, 20 nm TiO_2 NPs; 50, 75 nm citrate-coated Ag NPs	Mouse neuroblastoma cells	Lysis in Triton X-100	n/s	RF power 1400 W, additional gas flow (Ar) 0.95 L min^{-1}	Q	$^{107}Ag^+$, $^{48}Ti^+$	3 ms	22 nm Ag, 69 nm TiO_2		126

Table 2.2: Continued.

Year	NP types analyzed	Matrix	Sample preparation	Nebulizer and spray chamber	Plasma parameters	Mass analyzer	Measured isotopes	Dwell time	Size L_D (ESD)	Features	Reference
2016	10, 30, 70 nm PEG- BPEI-, citrate-coated Ag NPs	OECD 201 culture medium with *Pseudokirchiniella subcapitata*	Filtration (0.45 µm pore size), dilution	n/s	n/s	TQ	$^{107}Ag^+$	3 ms	n/s		127
2018	18 nm Al NPs, 20 nm Al_2O_3 NPs, 25 nm TiO_2 NPs	Model cell culture medium	n/s	PFA nebulizer, cyclonic spray chamber	Cooling gas 13 L min^{-1}, auxiliary gas 0.7 L min^{-1}, nebulizer gas 0.89 L min^{-1}	Q	n/s	3 ms	54 nm Al, 50 nm Al_2O_3, 60-100 nm TiO_2	Several methods for NP characterization are described	128
2018	NPs formed from Cr^{III} salts	Medium for algal ecotoxicity testing	Dilution	MicroMist nebulizer	RF power 1500 W, cooling gas 13.5 L min^{-1}, auxiliary gas 0.77 L min^{-1}, nebulizer gas 0.87 L min^{-1}	Q	$^{52}Cr^+$	0.05 ms	90 nm $Cr(OH)_3$		129

Table 2.2: Continued.

Year	NP types analyzed	Matrix	Sample preparation	Nebulizer and spray chamber	Plasma parameters	Mass analyzer	Measured isotopes	Dwell time	Size L_D (ESD)	Features	Reference
Body Fluids and Tissue											
2012	60 nm citrate-coated Ag NPs	Model saliva, gastric, duodenal, bile juices with and without proteins	Dilution	Babington type nebulizer, impact bead spray chamber	RF power 1400 W, cooling gas 13 L min^{-1}, auxiliary gas 0.7 L min^{-1}, nebulizer gas 1.1 L min^{-1}	Q	$^{107}Ag^+$	n/s	n/s		130
2015	44.5±9.2 nm Citrate-coated Au NPs	Spiked whole blood of rats	Dilution	MicroMist glass nebulizer	Nebulizer gas 1.05 L min^{-1}	Q	$^{197}Au^+$	10 ms	n/s		131
2017	Respirable crystalline silica	Exhaled breath condensate		n/s	n/s	Q with KED (He)	$^{28}Si^+$	3 ms	300 nm		132
2017	10, 30, 50, 60, 80, 100 nm citrate- or carboxylic acid-coated Ag and Au NPs	Spiked human whole blood	Dilution with Triton X, TMAH, and water	Concentric glass nebulizer, conical spray chamber	Nebulizer gas 1.06 L min^{-1}	Q	$^{107}Ag^+$, $^{197}Au^+$	50 µs	30 nm		133

Table 2.2: Continued.

Year	NP types analyzed	Matrix	Sample preparation	Nebulizer and spray chamber	Plasma parameters	Mass analyzer	Measured isotopes	Dwell time	Size L_D (ESD)	Features	Reference
2018	40 nm PEG-coated Ag NPs, broadly distributed PEG-, sodium carboxylate-coated Ag NPs	Spiked human placental tissue	Alkaline digestion with TMAH, enzymatic digestion with Proteinase K	MicroMist nebulizer, Scott spray chamber	RF power 1550 W, cooling gas 15 L min^{-1}, nebulizer gas 1.03 L min^{-1}	TQ	$^{107}Ag^+$	3 ms	25 nm		134
2018	Broadly distributed PEG-, sodium carboxylate-coated Ag NPs	Human *ex vivo* placenta perfusion model	Enzymatic digestion with Proteinase K	MicroMist nebulizer, Scott spray chamber for TQ; MicroFlow PFA nebulizer, cyclonic spray chamber for Q	RF power 1550 W, cooling gas 15 L min^{-1}, nebulizer gas 1.03-1.05 L min^{-1}	Q, TQ	$^{107}Ag^+$	3 ms	25 nm		135
Carbon Nanotubes (CNTs)											
2013	Intercalated Co and Y NPs	Single walled CNTs dispersions	Dilution of dispersed CNTs	n/s	n/s	Q	$^{89}Y^+$, $^{59}Co^+$	10 ms	n/s	Detection of trace catalytic metals intercalated in the CNTs	136

Table 2.2: Continued.

Year	NP types analyzed	Matrix	Sample preparation	Nebulizer and spray chamber	Plasma parameters	Mass analyzer	Measured isotopes	Dwell time	Size L_D (ESD)	Features	Reference
2016	Intercalated Y	Single walled CNTs dispersions, *Daphnia magna* in Nanopure water after CNT exposure	Dilution and sonication for *Daphnia magna* samples	n/s	RF power 1600 W, cooling gas 16 L min^{-1}, auxiliary gas 1.02 L min^{-1}, nebulizer gas 0.85-1 L min^{-1}	Q	$^{89}Y^{+}$	0.1, 10 ms	n/s		137
2017	Intercalated Y	Single walled CNTs, release supernatants containing degradation products	Surfactant addition, sonication, dilution	n/s	n/s	Q	$^{89}Y^{+}$	0.1 ms	n/s	CNT fragments were released due to photodegradation of CNTs and polycaprolactone nanocomposite	138
Cosmetics											
2015	32 to 40 nm TiO_2 NPs	Sunscreens	Dispersion in Triton X-100, dilution	Cyclonic spray chamber, Meinhard nebulizer	RF power 1600 W, nebulizer gas 1.06-1.08 L min^{-1}	Q	$^{48}Ti^{+}$	0.1 ms	27-29 nm		139

Table 2.2: Continued.

Year	NP types analyzed	Matrix	Sample preparation	Nebulizer and spray chamber	Plasma parameters	Mass analyzer	Measured isotopes	Dwell time	Size L_D (ESD)	Features	Reference
2017	30 to 120 nm TiO_2 NPs	Cosmetics and personal care products	Defatting with hexane, suspension in water, dilution or suspension in SDS, dilution	Cyclonic spray chamber, Meinhard nebulizer	RF power 1450 W	Q	$^{48}Ti^+$, $^{197}Au^+$	0.1 ms	35 nm TiO_2	No Au NPs were found in the tested samples	140
2018	≤107 nm TiO_2 and ≤98 nm ZnO NPs	Cream and spray sunscreens	Dispersion in Triton X-100, dilution	PFA nebulizer	n/s	Q with KED (He)	$^{48}Ti^+$, $^{64}Zn^+$	5 ms	25 nm TiO_2, 50 nm ZnO		141
2018	TiO_2 NPs	Sunscreen	Defatting with hexane, filtration, dilution	Meinhard nebulizer, cyclonic spray chamber	n/s	Q	$^{48}Ti^+$	0.1 ms	32 nm		142
2018	TiO_2 and ZnO NPs	Sunscreen powder	Dispersion in Triton X-100, dilution	n/s	n/s	n/s	n/s	n/s	n/s		143
2018	Al_2O_3, TiO_2, SiO_2 NPs	AF4 fractions after toothpaste fractionation	Dilution, see the article for detailed sample preparation procedure	Low-flow concentric nebulizer, cyclonic spray chamber	RF power 1549 W, cooling gas 14 L min^{-1}, auxiliary gas 0.79 L min^{-1}, nebulizer gas 1.04 L min^{-1}	Q	$^{27}Al^+$, $^{47}Ti^+$	10 ms	55-65 nm Al_2O_3 and TiO_2 NPs		144

Table 2.2: Continued.

Year	NP types analyzed	Matrix	Sample preparation	Nebulizer and spray chamber	Plasma parameters	Mass analyzer	Measured isotopes	Dwell time	Size L_D (ESD)	Features	Reference
Model Environmental Aqueous Samples											
2013	Nanoparticulate Zn, Mo, Ag in leachates	Model freshwater, seawater, acidic rainwater	Leaching	n/s	RF power 1550 W, cooling gas 15 L min^{-1}, auxiliary gas 0.35 L min^{-1}, nebulizer gas 0.79 L min^{-1}	Q with KED (He)	$^{66}Zn^{+}$, $^{98}Mo^{+}$, $^{107}Ag^{+}$	30 ms	n/s	Leaching of CIGS and OPV cells into model waters was studied	145
2014	50 nm PVP-coated Ag NPs	Spiked littoral mesocosms on a lake	Spiking, dilution	n/s	n/s	Q	$^{107}Ag^{+}$	10 ms	30 nm		146
2014	60 and 100 nm citrate-, tannic acid-, PVP-coated Ag NPs	Spiked deionized, tap, surface, EPA moderately hard reconstituted laboratory waters	Spiking	n/s	n/s	Q	$^{107}Ag^{+}$	10 ms	25-30 nm	NPs dissolution kinetic study	147

Table 2.2: Continued.

Year	NP types analyzed	Matrix	Sample preparation	Nebulizer and spray chamber	Plasma parameters	Mass analyzer	Measured isotopes	Dwell time	Size L_D (ESD)	Features	Reference
2014	50 nm citrate-coated, 80 nm PVP-coated Ag NPs	Spiked purified water, waste water influent and effluent, river water	Filtration (0.45 µm pore size), spiking	Glass conical nebulizer, conical spray chamber with impact bead	RF power 1450 W, cooling gas 15 L min^{-1}, nebulizer gas 0.85 and 0.93 L min^{-1}	Q	$^{107}Ag^+$, $^{109}Ag^+$	5 ms	40 nm	Internal calibration with isotope dilution (^{109}Ag enriched silver standard) was used, both silver isotopes were monitored in one run with 1.9 ms settling time	68
2015	50 nm ZnO NPs and Zn-containing NPs	Spiked and unspiked surface water, effluent waste water (Des Prairies River, Montreal WWTP, Canada)	Spiking, dilution or IEC (Chelex 100)	Type C0.5 concentric glass nebulizer, cyclonic spray chamber	n/s	Q	n/s	0.5 ms	32 nm for Milli-Q water, 70 nm for river water, 126 nm for waste water		148
2016	80-200 nm ZnO NPs, 30-50 nm CeO_2 NPs, Zn- and Ce-containing NPs	Spiked river water after real and model drinking water treatment facility, river water	Spiking, water treatment, dilution; or no treatment	Meinhard concentric nebulizer, cyclonic spray chamber	RF power 1600 W, cooling gas 18 L min^{-1}, auxiliary gas 1.2 L min^{-1}, nebulizer gas 1.02-1.06 L min^{-1}	Q	$^{67}Zn^+$, $^{140}Ce^+$	0.1 ms	35-40 nm ZnO, 18-20 nm CeO_2		149

Table 2.2: Continued.

Year	NP types analyzed	Matrix	Sample preparation	Nebulizer and spray chamber	Plasma parameters	Mass analyzer	Measured isotopes	Dwell time	Size L_D (ESD)	Features	Reference
2016	Ti-containing NPs; 100, 160 nm TiO_2 NPs; 40, 70, 100 nm citrate-coated Ag NPs; 50, 80, 100 nm citrate-coated Au NPs	Spiked river water after real and model drinking water treatment facility, river water	Spiking, water treatment, dilution; or no treatment	Meinhard concentric nebulizer, cyclonic spray chamber	RF power 1600 W, cooling gas 18 L min^{-1}, auxiliary gas 1.2 L min^{-1}, nebulizer gas 1.02-1.06 L min^{-1}	Q	$^{47}Ti^+$, $^{197}Au^+$, $^{107}Ag^+$	0.1 ms	65-70 nm TiO_2, 21-23 nm Ag, 27-30 nm Au		150
2016	80 nm citrate- and PVP-coated Ag NPs	Spiked waste water effluent and mixed liquor	Filtration (0.45 µm pore size), spiking	Concentric glass nebulizer, cyclonic spray chamber	RF power 1600 W, cooling gas L min^{-1}, auxiliary gas L min^{-1}, nebulizer gas L min^{-1}, sampling position mm	Q	$^{107}Ag^+$	0.1 ms, 10 ms	10 nm for double deionized water		151
2016	20 and 50 nm citrate-, PVP-, lipoic acid-coated Ag NPs	Spiked lake water	Filtration (0.22 µm pore size), spiking	n/s	RF power 1550 W, cooling gas 15 L min^{-1}	Q	$^{107}Ag^+$, $^{109}Ag^+$	5 ms	24 nm		152

Table 2.2: Continued.

Year	NP types analyzed	Matrix	Sample preparation	Nebulizer and spray chamber	Plasma parameters	Mass analyzer	Measured isotopes	Dwell time	Size L_D (ESD)	Features	Reference
2016	30, 60, 80, 100 nm tannic acid-coated Au NPs	Spiked river and waste waters	Filtration (0.45 µm pore size), spiking	MicroMist nebulizer	RF power 1550 W, auxiliary gas 0.1 L min^{-1}, nebulizer gas 1.05 L min^{-1}	Q	$^{197}Au^{+}$	3 ms	19 nm for ultrapure water, 31 nm for 0.1 µg L^{-1} Au^{3+}		153
2016	75 nm PVP-coated Ag NPs	Reaction in aerated, sulfide-containing water and EPA moderately hard reconstituted water standard	Spiking, dilution	Microflow concentric PFA nebulizer, impact bead spray chamber,	n/s	Q	$^{107}Ag^{+}$	10 ms	15 nm		154
2016	40, 80 nm citrate-coated Ag NPs	Spiked waste water effluent and influent, river water	Filtration (0.45 µm pore size), spiking, HDC	Concentric nebulizer	n/s	Q	$^{107}Ag^{+}$	0.1 ms	24 nm		102
2016	50, 80 nm citrate- or PVP-coated Ag NPs	Spiked MilliQ water, chloride containing MilliQ water, MilliQ water at pH 5, 7, and 7.6	Spiking	Conical nebulizer, impact bead spray chamber	RF power 1450 W, cooling gas 15 L min^{-1}, nebulizer gas 0.85 L min^{-1}	Q	$^{107}Ag^{+}$	5 ms	40 nm without Ag^{+}	Ozonation was used for selected samples	155

Table 2.2: Continued.

Year	NP types analyzed	Matrix	Sample preparation	Nebulizer and spray chamber	Plasma parameters	Mass analyzer	Measured isotopes	Dwell time	Size L_D (ESD)	Features	Reference
2017	50 nm citrate-, tannic acid-coated Ag NPs	Spiked waste water effluent, MilliQ water, modified TAP medium	Spiking, dilution, IEC	n/s	n/s	Q	n/s	0.5 ms	17 nm		156
2017	10, 20, 30, 40, 50, 60, 70, 80, 100 nm PVP-coated Ag NPs	Spiked lake, tap waters; liquid consumer products, migration solutions from plasters	Spiking, dilution	Cyclonic spray chamber, Meinhard concentric nebulizer	n/s	Q	$^{107}Ag^+$	50 µs	12-15 nm		157
2017	20, 40, 80, 100, 200 nm PVP-coated and commercial Ag NPs	Spiked waste water effluent, environmental water	Spiking, centrifugation	n/s	n/s	Q	n/s	10 ms	n/s		158
2017	10-25 nm TiO_2 and 10-30 nm ZnO NPs	Spiked river water	Spiking, dilution	Reference to previous studies	Reference to previous studies	Q	$^{47}Ti^+$, $^{66}Zn^+$	0.1 ms	64 nm TiO_2, 43 nm ZnO		159
2017	30-50 nm PVP-coated Ag NPs	Spiked MilliQ and lake waters with gum arabic	Sonication, dilution	n/s	n/s	Q	$^{107}Ag^+$	5 ms	40 nm		160

Table 2.2: Continued.

Year	NP types analyzed	Matrix	Sample preparation	Nebulizer and spray chamber	Plasma parameters	Mass analyzer	Measured isotopes	Dwell time	Size L_D (ESD)	Features	Reference
2017	60 nm Ag-Ag core-shell NPs (30 nm core, 15 nm shell)	Spiked EPA moderately hard water with or without fulvic acid	Spiking	Cyclonic spray chamber, Meinhard concentric nebulizer	RF power 1600 W	Q	$^{107}Ag^+$, $^{197}Au^+$	0.1 ms	15.5 nm Ag		161
2017	40, 80, 100 nm citrate- or PVP-coated Ag NPs	Spiked wastewater biosolids (raw or supernatant)	Filtration (0.45 µm pore size), spiking	Cyclonic spray chamber, type C0.5 concentric glass nebulizer	n/s	Q	$^{107}Ag^+$	0.5 ms	n/s		162
2017	40, 60 nm BPEI- and PVP-coated Ag NPs	Spiked microcosm tanks with seawater	Spiking	Flow injection, pneumatic nebulizer	Reference to previous studies	Q	$^{107}Ag^+$	10 ms	n/s		163
2017	40 nm citrate-coated Ag NPs	Spiked WWTP mesocosm	Filtration (0.1 mm pore size), spiking	Cyclonic spray chamber, Burgener Mira Mist nebulizer	RF power 1205 W, cooling gas 15.01 L min^{-1}, auxiliary gas 0.75 L min^{-1}, nebulizer gas 0.520 L min^{-1}	SF	n/s	0.1 ms	From 5.4 nm to 30-40 nm		64

Table 2.2: Continued.

Year	NP types analyzed	Matrix	Sample preparation	Nebulizer and spray chamber	Plasma parameters	Mass analyzer	Measured isotopes	Dwell time	Size L_D (ESD)	Features	Reference
2018	Aged 34 nm citrate-coated Ag NPs, Ag-containing aggregates	Remobilization medium (remobilization from a model sediment)	Dilution, filtration (1 µm pore size) or no filtration	n/s	n/s	Q	$^{107}Ag^+$	5 ms	30 nm		164
2018	40, 70, 100 nm citrate-coated Ag; 50, 80, 100 nm citrate-coated Au; 100 nm TiO_2; 30-50 nm CeO_2; 80-200 nm ZnO NPs	Spiked river and lake waters with alum, ferric oxides, or ferric sulfate	Dilution	Reference to previous studies	Reference to previous studies	Q	$^{47}Ti^+$	0.1 ms	25 nm Ag, 30 nm Au, 70 nm TiO_2, 23 nm CeO_2, 44 nm ZnO		165
2018	25 nm PVP-coated Ag NPs, 5 nm TiO_2 NPs	Effluent of a lab-scale WWTP	Sonication, dilution	n/s	n/s	Q	$^{107}Ag^+$	3 ms	n/s		166
2018	30, 50, 80, 100 nm citrate-coated and 60, 100 nm PVP-coated Ag NPs	Spiked tap, river waters, waste water influent	Spiking, Ag^+ was adsorbed by magnetic reduced graphene oxide	n/s	RF power 1550 W, cooling gas 15 L min^{-1}	Q	$^{107}Ag^+$	3 ms	20 nm		167

Table 2.2: Continued.

Year	NP types analyzed	Matrix	Sample preparation	Nebulizer and spray chamber	Plasma parameters	Mass analyzer	Measured isotopes	Dwell time	Size L_D (ESD)	Features	Reference
2018	30-50 nm PVP-coated Ag NPs	Spiked surface water of a boreal oligotrophic lake	Lake spiking	Reference to previous studies	Reference to previous studies	SF	$^{107}Ag^+$	50 µs	12 nm		168
2018	30-50 nm PVP-coated Ag NPs	Spiked surface water of a boreal oligotrophic lake	Lake spiking	Glass conical nebulizer	RF power 1450 W, cooling gas 15 L min^{-1}	Q	$^{107}Ag^+$	5 ms	45±5 nm		169
2018	50 nm zero-valent iron NPs, Cd^{2+} sorbed to the NPs	Spiked Milli-Q water, synthetic and effluent waste waters	Spiking, shaking	Scott spray chamber	RF power 1550 W, cooling gas 15.0 L min^{-1}, auxiliary gas 0.90 L min^{-1}, nebulizer gas 1.09 L min^{-1}, sampling position 8 mm	TQ	$^{56}Fe^+$, $^{111}Cd^+$	3 ms	36 nm	H_2 was used as a reaction gas	170

Table 2.2: Continued.

Year	NP types analyzed	Matrix	Sample preparation	Nebulizer and spray chamber	Plasma parameters	Mass analyzer	Measured isotopes	Dwell time	Size L_D (ESD)	Features	Reference
2019	20,40, 60 nm citrate-coated Ag NPs	Spiked Milli-Q water, spiked wastewater	CPE	PFA Microflow nebulizer, cyclonic spray chamber	RF power 1600 W, cooling gas 18.0 L min^{-1}, auxiliary gas 1.2 L min^{-1}, nebulizer gas 0.83 L min^{-1}	Q	$^{107}Ag^{+}$	0.1 ms	>20 nm	Optimization of CPE was performed	171
Environmental Aqueous Samples											
2014	TiO_2 NPs released from sunscreen products	Suspended particulate matter of Old Danube Lake, Vienna, Austria	Dilution	n/s	n/s	Q	$^{47}Ti^{+}$	10 ms	130 nm	Interference of $^{48}Ti^{+}$ with $^{48}Ca^{+}$	172
2015	50 nm ZnO NPs and Zn-containing NPs	Spiked and unspiked surface water, effluent waste water (Des Prairies River, Montreal WWTP, Canada)	Spiking, dilution or IEC (Chelex 100)	Type C0.5 concentric glass nebulizer, cyclonic spray chamber	n/s	Q	n/s	0.5 ms	32 nm for Milli-Q water, 70 nm for river water, 126 nm for waste water		148

Table 2.2: Continued.

Year	NP types analyzed	Matrix	Sample preparation	Nebulizer and spray chamber	Plasma parameters	Mass analyzer	Measured isotopes	Dwell time	Size L_D (ESD)	Features	Reference
2016	Ag-containing NPs	WWTP and surface waters from the River Isar, Germany; pre-alpine lakes water, Germany	CPE, dilution	n/s	n/s	Q	$^{107}Ag^+$	3 ms	14 nm		173
2016	Citrate-coated Ag NPs, tannic acid-coated Au NPs, Ag- and Au-containing NPs	Spiked filtered natural and waste waters, unspiked natural water (Guiyu and Xiangjiang Rivers and Chendian Lake, China) and waste water (HuNan University, China)	Filtration with nylon membrane (0.45 and 0.22 µm pore size) before spiking; dilution for unspiked samples	MicroMist nebulizer	RF power 1550 W, auxiliary gas 0.1 L min^{-1}, nebulizer gas 1.05 L min^{-1}, sampling position 8 mm	Q	$^{107}Ag^+$, $^{197}Au^+$	3 ms	20 nm Ag, 19 nm Au		103

Table 2.2: Continued.

Year	NP types analyzed	Matrix	Sample preparation	Nebulizer and spray chamber	Plasma parameters	Mass analyzer	Measured isotopes	Dwell time	Size L_D (ESD)	Features	Reference
2017	71 and 145 nm TiO_2 NPs	Influent sewage, aeration tank contents of WWTP (Hyderabad, India)	Microwave digestion (HNO_3 and H_2O_2), filtration with cellulose acetate membrane (0.22 µm pore size), sonication	n/s	RF power 1550 W, nebulizer gas 1.05 L min^{-1},	n/s	$^{47}Ti^+$	3 and 10 ms	n/s		174
2017	Ti-containing NPs	Surface water of Clear Creek in Golden, Colorado, USA	n/s	n/s	n/s	Q, SF	$^{49}Ti^+$ at quadrupole, $^{48}Ti^+$ at SF	3 ms	79 nm TiO_2 for Q, 42 nm TiO_2 for SF	SF measurements were presented as a proof of concept	175
2018	Ti-containing natural NPs and engineered TiO_2 NPs	Water samples from Old Danube Lake, Vienna, Austria	Sonication, centrifugation for TQ; sonication, dialysis for TOF	n/s	n/s	TQ, TOF	$^{63}TiNH^+$ for TQ, MA for TOF	4 ms for TQ, 3 ms for TOF	81 nm TiO_2 for TQ	NH_3 and He were used as reaction/collision gases	75

Table 2.2: Continued.

Year	NP types analyzed	Matrix	Sample preparation	Nebulizer and spray chamber	Plasma parameters	Mass analyzer	Measured isotopes	Dwell time	Size L_D (ESD)	Features	Reference
2018	Ag-containing NPs	Water from Vltava, Prague, Czech Republic	1% (w/w) gelatin for stabilization	PTFE concentric nebulizer, cyclonic spray chamber	RF power 1100 W, cooling gas 11 L min^{-1}, auxiliary gas 1.0 L min^{-1}, nebulizer gas 0.85 L min^{-1}	Q	$^{107}Ag^{+}$	0.1 ms	15 nm		176
2018	Ag-containing NPs	Bottom sediments and labile sediments from Lake Ontario, Canada, freeze-dried samples	Sonication with water, centrifugation, filtration (0.45 µm pore size)	Reference to previous studies	Reference to previous studies	SF mass analyzer was used in low resolution mode	$^{107}Ag^{+}$	50 µs	16 nm		177
2018	Ag, CeO_2, TiO_2 NPs	Surface water of Meuse and Ijssel Rivers, the Netherlands	Sonication	MicroFlow PFA nebulizer, cyclonic spray chamber	RF power 1550 W, cooling gas 14 L min^{-1}, auxiliary gas 0.8 L min^{-1}, nebulizer gas 1.1 L min^{-1}	Q	$^{107}Ag^{+}$, $^{140}Ce^{+}$, $^{48}Ti^{+}$, $^{139}La^{+}$	3 ms	14 nm Ag, 10 nm CeO_2, 100 nm TiO_2	Multi-elemental analysis was used with 100 µs dwell time to detect $^{140}Ce^{+}$ and $^{139}La^{+}$	178

Table 2.2: Continued.

Year	NP types analyzed	Matrix	Sample preparation	Nebulizer and spray chamber	Plasma parameters	Mass analyzer	Measured isotopes	Dwell time	Size L_D (ESD)	Features	Reference
2018	Ti-containing NPs	Water from Salt River, pools, Arizona, USA	Filtration (0.7 µm pore size)	n/s	n/s	Q	$^{49}Ti^+$	10 ms	148 ± 3 nm for river water, 173 ± 15 nm for pool water		179
2018	Ag-containing NPs	Water from Lake Königssee and Lake Waginger See, Bavaria, Germany	CPE, dilution	n/s	n/s	Q	$^{107}Ag^+$	0.1 ms	10 nm		180
2018	Pb-, Fe-, Sn-, Cu-, Ag-, Ti-containing particles	Tap water from Phoenix, Arizona, USA		n/s	n/s	Q with KED for $^{56}Fe^+$	$^{208}Pb^+$, $^{56}Fe^+$, $^{118}Sn^+$, $^{107}Ag^+$, $^{65}Cu^+$, $^{49}Ti^+$	10 ms	11.3 nm Pb, 55 nm Fe, 26 nm Sn, 40 nm Cu, 75 nm Ti, 13 nm Ag	No Ti- and Ag-containing NPs were discovered	181
Model Food Samples											
2014	20, 40, 100 nm PVP-coated Ag NPs	Food simulants (distilled water, 10% ethanol)	Dilution	Varied among the participants	Varied among the participants	n/s	n/s	3 ms	Varied among the participants	Interlaboratory method performance study with over 23 laboratories	84

Table 2.2: Continued.

Year	NP types analyzed	Matrix	Sample preparation	Nebulizer and spray chamber	Plasma parameters	Mass analyzer	Measured isotopes	Dwell time	Size L_D (ESD)	Features	Reference
2014	30, 60 nm citrate-coated Au NPs, 60 nm citrate-coated Ag NPs	Spiked Milli-Q water, chicken digest (enzymatic digestion)	Dilution	Varied among the participants	Varied among the participants	n/s	$^{107}Ag^+$, $^{197}Au^+$	3 ms	Varied among the participants	Interlaboratory method performance study with over 9 laboratories, 3 of which used SP-ICP-MS	182
2016	60 nm PVP-coated Ag NPs	Food simulants (water, 10% ethanol, 3% acetic acid)	Dilution	MicroMist nebulizer	RF power 1550 W, cooling gas 15 L min^{-1}	Q	$^{107}Ag^+$	3 ms	n/s		183
2016	10, 30, 50, 60, 100 nm Ag NPs, 10, 20, 30, 50, 60, 70, 80 nm Au NPs	Spiked water, orange juice, apple juice	Dilution	n/s	n/s	Q	$^{107}Ag^+$, $^{197}Au^+$	50 µs	31-34 nm	The coatings were not specified for each size of the NPs. Citrate-, PVP-coated Ag NPs; citrate-, carboxylic acid-coated, PBS-buffered Au NPs were used.	184

Table 2.2: Continued.

Year	NP types analyzed	Matrix	Sample preparation	Nebulizer and spray chamber	Plasma parameters	Mass analyzer	Measured isotopes	Dwell time	Size L_D (ESD)	Features	Reference
2018	40 nm PEG-, citrate-coated Ag NPs	Food simulants (10%, 20%, 50% ethanol; 3% acetic acid, olive oil), low fat cow milk, 2% NaCl	Dilution, Triton X-100 was used to create olive oil emulsion in water	Low-flow concentric nebulizer, cyclonic spray chamber	RF power 1550 W, cooling gas 14 L min^{-1}, auxiliary gas 0.80 L min^{-1}, nebulizer gas 0.96 L min^{-1}	Q	$^{107}Ag^+$	3 ms	10-20 nm		185
Food											
2014	TiO_2 NPs	Food grade TiO_2 (E171), food and personal care products	Food grade TiO_2 suspension in BSA, heating with H_2O_2 and resuspension in BSA for other products	Conical glass concentric nebulizer	RF power 1400 W	Q	$^{48}Ti^+$	3 ms	50 nm		186
2015	Ag NPs	Decoration of pastry (“pearls”)	Dissolution in water, dilution	MicroMist nebulizer	n/s	Q	$^{107}Ag^+$	3 ms	13 nm		187

Table 2.2: Continued.

Year	NP types analyzed	Matrix	Sample preparation	Nebulizer and spray chamber	Plasma parameters	Mass analyzer	Measured isotopes	Dwell time	Size L_D (ESD)	Features	Reference
2018	TiO_2 NPs	Candy products	Sonication in water, dilution	MicroMist nebulizer, cyclonic spray chamber	RF power 1550 W, cooling gas 14 L min^{-1}, auxiliary gas 0.8 L min^{-1}, nebulizer gas 1.03 L min^{-1}	TQ	$^{48}Ti^+$ with O_2 gashad the highest sensitivity	10 ms	26 nm	Optimization of TQ detection was performed with different gases	59
2018	TiO_2 NPs	Coating of chocolate candies	Extraction with water, sonication, filtration, dilution	Meinhard nebulizer, cyclonic spray chamber	n/s	Q	$^{48}Ti^+$	0.1 ms	32 nm		142
2018	TiO_2, Cu, Ag NPs	Drinks and food	Sample preparation varied depending on the product	Meinhard nebulizer, cyclonic spray chamber	n/s	Q	$^{107}Ag^+$, $^{63}Cu^+$, $^{48}Ti^+$	0.1 µs	32 nm TiO_2, 30 nm Ag		188

Table 2.2: Continued.

Year	NP types analyzed	Matrix	Sample preparation	Nebulizer and spray chamber	Plasma parameters	Mass analyzer	Measured isotopes	Dwell time	Size L_D (ESD)	Features	Reference
2018	Al-containing NPs	Chinese noodles	Enzymatic digestion with α-amylase	Low-low concentric nebulizer, cyclonic spray chamber	RF power 1550 W, cooling gas 13.9 L min^{-1}, auxiliary gas 0.79 L min^{-1}, nebulizer gas 1.07 L min^{-1}	Q	$^{27}Al^+$	3 ms	54-83 nm Al_2O_3		189
2019	TiO_2 NPs	Surimi (crab sticks)	Enzymatic digestion with pancreatin and lipase, dilution with 1% glycerol, sonication	n/s	RF power 1600 W, cooling gas 16 L min^{-1}, auxiliary gas 1.2 L min^{-1}, nebulizer gas 0.95 L min^{-1}	Q	$^{49}Ti^+$	0.1 ms	31.3-37.1 nm		190

Table 2.2: Continued.

Year	NP types analyzed	Matrix	Sample preparation	Nebulizer and spray chamber	Plasma parameters	Mass analyzer	Measured isotopes	Dwell time	Size L_D (ESD)	Features	Reference
Plants exposure											
2015	40 nm PVP-coated; 10, 12, 15, 20, 30, 40, 50, 80, 100 nm citrate-coated Au NPs	Tomato plants	Enzymatic digestion with Macerozyme R-10, dilution	Meinhard nebulizer, cyclonic spray chamber	RF power 1600 W, cooling gas 18 L min^{-1}, auxiliary gas 1.2 L min^{-1}, nebulizer gas 1.08 L min^{-1}	Q	$^{197}Au^{+}$	0.1 ms	20 nm		191
2016	10 nm citrate-coated Ag NPs	*Arabidopsis thaliana* plants´ roots and shoots	Enzymatic digestion with Macerozyme R-10, dilution	n/s	n/s	Q	$^{107}Ag^{+}$	0.05 ms	10 nm		192
2016	30-50 nm, 50-100 nm CeO_2 NPs	Shoots of cucumber (*C. sativus*), tomato (*S. lycopersicum L.*), soybean (*Glycine max*), pumpkin (*Cucurbita pepo*)	Enzymatic digestion with Macerozyme R-10	Meinhard nebulizer, cyclonic spray chamber	RF power 1600 W, cooling gas 18 L min^{-1}, auxiliary gas 1.2 L min^{-1}, nebulizer gas 1.06 L min^{-1}	Q	$^{140}Ce^{+}$	0.1 ms	23-25 nm		193

Table 2.2: Continued.

Year	NP types analyzed	Matrix	Sample preparation	Nebulizer and spray chamber	Plasma parameters	Mass analyzer	Measured isotopes	Dwell time	Size L_D (ESD)	Features	Reference
2016	70 nm citrate-coated Pt NPs	*Lepidium sativum*, *Sinapis alba* plants	Enzymatic digestion with Macerozyme R-10, filtration (0.45 µm pore size), dilution	Meinhard glass microconcentric nebulizer, cyclonic spray chamber	RF power 1450 W, cooling gas 15.0 L min^{-1}, auxiliary gas 1.0 L min^{-1}, nebulizer gas 0.98 L min^{-1}	Q	$^{195}Pt^{+}$	0.1 ms	n/s		194
2017	Cu-containing NPs from fungicide residues (copper oxychloride)	Vine leaves	Rainfall washoff, throughfall sampling, filtration (0.45 µm pore size), dilution	n/s	n/s	Q	$^{63}Cu^{+}$	0.1 ms	8-60 nm Cu		195
2017	17 nm PVP-coated Ag NPs	Soybean, rice (root and foliar exposures)	Enzymatic digestion with Macerozyme R-10, dilution	Meinhard nebulizer, cyclonic spray chamber	n/s	Q	$^{107}Ag^{+}$	0.05 ms	14 nm		196
2017	PVP-coated Ag_2S	Dicotyledonous cucucmber (*Cucumis sativus*), monocotyladonous wheat (*Triticum aestivum* L.)	Enzymatic digestion with Macerozyme R-10, dilution	n/s	n/s	TQ	$^{107}Ag^{+}$	3 ms	20-25 nm		197

Table 2.2: Continued.

Year	NP types analyzed	Matrix	Sample preparation	Nebulizer and spray chamber	Plasma parameters	Mass analyzer	Measured isotopes	Dwell time	Size L_D (ESD)	Features	Reference
2018	20-100 nm CuO NPs	Leaves of vegetables, kale (*Brassica oleracea*, var. *Acephala Lacinato*), lettuce (*Lactuca sativa* var. *green leaf cultivar*), collard green (*Brassica oleracea*, var. *Acephala)*	Exposure to NPs, rinsing with ultrapure water or enzymatic digestion with Macerozyme R-10, dilution	Glass concentric nebulizer	RF power 1550 W, nebulizer gas 0.67 L min^{-1}, sampling position 8.0 mm	Q	$^{63}Cu^{+}$	0.1 ms	n/s		198
2018	Pd NPs	*Sinapis alba* leaves, stems, roots	Enzymatic digestion with Macerozyme R-10, filtration (0.45 µm pore size), dilution	Meinhard glass microconcentric nebulizer, cyclonic spray chamber	RF power 1450 W, cooling gas 15.0 L min^{-1}, auxiliary gas 0.9 L min^{-1}, nebulizer gas 1.10 L min^{-1}	Q	$^{105}Pd^{+}$	0.1 ms	25-30 nm		199

Table 2.2: Continued.

Year	NP types analyzed	Matrix	Sample preparation	Nebulizer and spray chamber	Plasma parameters	Mass analyzer	Measured isotopes	Dwell time	Size L_D (ESD)	Features	Reference
2018	"Green synthesis" of Ag NPs	Leaf sap extract from *Aloe arborescens*	$AgNO_3$ addition to the leaf sap extract induces the formation of Ag NPs under sunlight, centrifugation, dilution	Concentric quartz nebulizer, baffle-type cyclonic spray chamber	RF power 1500 W, cooling gas 17 L min^{-1}, auxiliary gas 1.4 L min^{-1}, nebulizer gas 0.8 L min^{-1}	Q	$^{107}Ag^+$	5 ms	n/s		200
2018	Isotopically labelled Ag, Cu, ZnO NPs	*Arabidopsis thaliana* shoot and roots	Macerozyme R-10, filtration (0.22 µm pore size), dilution	MicroMist nebulizer	Cooling gas 15 L min^{-1}, auxiliary gas 1.0 L min^{-1}, nebulizer gas 1.05 L min^{-1}	Q	$^{107}Ag^+$, $^{65}Cu^+$, $^{70}Zn^+$	3 ms	n/s	Cu, ZnO NPs were not detected in shoots or roots because of the high background	201
2019	"Green synthesis" of Ag NPs	Cucumber leaf extract	$AgNO_3$ addition to the leaf extract, pH 10.0, 4 h at 80 °C	n/s	RF power 1550 W, nebulizer gas 0.67 L min^{-1}, sampling position 8.0 mm	Q	$^{107}Ag^+$	0.1 ms	n/s		202

Table 2.2: Continued.

Year	NP types analyzed	Matrix	Sample preparation	Nebulizer and spray chamber	Plasma parameters	Mass analyzer	Measured isotopes	Dwell time	Size L_D (ESD)	Features	Reference
Model Soil Samples											
2014	25 nm PVA-coated Ag NPs, 30 nm ZnO NPs, 42 nm TiO_2 NPs, 35 nm CeO_2 NPs	Soil spiked with biosolids that were enriched with NPs	Spiking, water extraction, centrifugation, filtration (0.45 µm pore size)	n/s	n/s	Q	n/s	10 ms	18 nm Ag, 70-80 nm TiO_2, 10 nm CeO_2		203
2015	CuO NPs	Spiked topsoil colloid extracts	Extraction, dilution, spiking	MicroMist nebulizer	RF power 1550 W, cooling gas 15 L min^{-1}, auxiliary gas 0.15 L min^{-1}, nebulizer gas 0.98 L min^{-1}	Q with KED (He)	$^{63}Cu^{+}$	5 ms or 0.1 ms	15±10 nm		204
2017	10, 30, 60 nm citrate-coated Au NPs, 30 nm BPEI- and PVP-coated Au NPs	Spiked soil colloid extracts	Water extraction, centrifugation, filtration (0.45 µm pore size), spiking, CPE	Concentric MicroMist nebulizer, Scott spray chamber	n/s	Q	$^{197}Au^{+}$	10 ms	n/s		205

Table 2.2: Continued.

Year	NP types analyzed	Matrix	Sample preparation	Nebulizer and spray chamber	Plasma parameters	Mass analyzer	Measured isotopes	Dwell time	Size L_D (ESD)	Features	Reference
2017	40 nm PVP-coated Ag NPs	Natural sandy loam soil spiked with biosolids that were enriched with NPs	Spiking, TSPP extraction, gravimetric sedimentation, dilution	Low pressure PFA nebulizer	RF power 1600 W, nebulizer gas 1.04 L min^{-1}	Q	$^{107}Ag^{+}$	0.05 µs	20 nm		206
2017	40 nm PVP-coated Ag NPs	Nanopure water with $NaNO_3$ and KNO_3, filtered sandy loam soil extracts with $NaNO_3$ and KNO_3	KNO_3 extraction, centrifugation, filtration (0.45 µm and 0.22 µm pore size), spiking, dilution	Low pressure PFA nebulizer, cyclonic spray chamber	RF power 1600 W, nebulizer gas 1.04 L min^{-1}	Q	$^{107}Ag^{+}$	0.05 µs	19 nm		207
2017	25, 40 nm PVP-coated Ag NPs	Spiked sandy loam soils and biosolids extracts	Spiking, TSPP extraction, sonication, filtration (0.45 µm and 0.22 µm pore size), dilution	Low pressure PFA nebulizer, cyclonic spray chamber	RF power 1600 W, nebulizer gas 1.04 L min^{-1}	Q	$^{107}Ag^{+}$	0.05 µs	19 nm	Optimization of the NPs extraction conditions from soil, only the most efficient conditions were mentioned	208

Table 2.2: Continued.

Year	NP types analyzed	Matrix	Sample preparation	Nebulizer and spray chamber	Plasma parameters	Mass analyzer	Measured isotopes	Dwell time	Size L_D (ESD)	Features	Reference
2018	30 nm citrate-, BPEI-, PVP-, PEG-, NOM-coated Au NPs	Standard soils water extracts, estuarine sediment in moderately hard water	Spiking, moderately hard water extraction, centrifugation, dilution	Concentric nebulizer, Scott spray chamber	n/s	Q	$^{197}Au^{+}$	10 ms	n/s		209
2018	40, 100 nm citrate-coated; 75, 100 nm PVP- and PEG-coated Ag NPs	Consumer product (band aid) water extracts, spiked soil water extracts	Spiking, Milli-Q water extraction, filtration (0.45 µm pore size)	n/s	RF power 1500 W, cooling gas 15 L min^{-1}	Q	$^{107}Ag^{+}$	10 ms	n/s		210
Solid Environmental Samples											
2016	As-containing NPs	Leachate from mine wastes	Leaching with 1 mM KCl, centrifugation	Glass concentric slurry nebulizer, cyclonic spray chamber	RF power 1200 W, cooling gas 15 L min^{-1}, auxiliary gas 1.2 L min^{-1}, nebulizer gas 1.0 L min^{-1}	Q	$^{75}As^{+}$	5 ms	117 nm $Fe^{III}As^{V}O_4 \cdot 2H_2O$	Settling time of 3 ms	211

Table 2.2: Continued.

Year	NP types analyzed	Matrix	Sample preparation	Nebulizer and spray chamber	Plasma parameters	Mass analyzer	Measured isotopes	Dwell time	Size L_D (ESD)	Features	Reference
2017	Zn-, Fe-, Ti-containing NPs	Sewage sludge	Acetic acid extraction, dilution	n/s	n/s	Q with KED for $^{56}Fe^+$	$^{47}Ti^+$, $^{66}Zn^+$, $^{56}Fe^+$	0.1 ms	15-20 nm Ti, 15-16 nm Zn, 12-17 nm Fe		212
2017	Ce-containing natural NPs and <50 nm CeO_2 NPs	Spiked topsoil samples	Spiking, shaking, wet-sieving (32 µm pore size), freeze-drying, aqueous colloid extraction, dilution	Pneumatic nebulizer, cyclonic spray chamber for TOF; Miramist nebulizer for Q	RF power 1400 W, cooling gas 16 L min^{-1}, auxiliary gas 1.1 L min^{-1}, nebulizer gas 1.2 L min^{-1} for TOF; RF power 1550 W, cooling gas 15 L min^{-1}, auxiliary gas 0.4 L min^{-1}, nebulizer gas 0.8 L min^{-1} for Q	TOF at 33 kHz complete mass spectrum in 300 µs, Q	MA for TOF; $^{140}Ce^+$ and $^{139}La^+$ for Q	n/a for TOF, 5 ms for Q	0.10-0.17 fg Ce, 0.13 fg La for TOF; 0.13-0.57 fg Ce, 0.21-0.34 fg La for Q	Natural and engineered NPs were identified with multi-element fingerprinting	74

Table 2.2: Continued.

Year	NP types analyzed	Matrix	Sample preparation	Nebulizer and spray chamber	Plasma parameters	Mass analyzer	Measured isotopes	Dwell time	Size L_D (ESD)	Features	Reference
2018	Pt NPs	Road dust leachate, catalyst material	Ultrasonic extraction with stormwater runoff, filtration (0.45 µm pore size)	Quartz nebulizer	n/s	Q	$^{195}Pt^{+}$	5 ms	7.4 nm		213
Model Water Samples											
2013	1-10 nm sodium polyacrylate-coated; 20, 40, 80 Ag NPs	NPs water suspensions	Dilution	n/s	n/s	Q	n/s	3 ms	20 nm		214
2015	100 nm citrate-coated Ag NPs; 60, 100 nm Au NPs; Au/Ag 48 nm core/ 15 nm shell	Spiked water with laundry detergents	Spiking, filtration or no filtration, dilution	Type-C MiraMist nebulizer, cyclonic spray chamber	n/s	Q	n/s	3 ms	30 nm Ag		215

Table 2.2: Continued.

Year	NP types analyzed	Matrix	Sample preparation	Nebulizer and spray chamber	Plasma parameters	Mass analyzer	Measured isotopes	Dwell time	Size L_D (ESD)	Features	Reference
2015	252 nm DNA/SiO_2 NPs, 350 nm SiO_2 NPs	Spiked ultrapure and drinking waters	Dilution	Quartz MicroMist nebulizer, cyclonic spray chamber	RF power 950 W, cooling gas 16 L min^{-1}, auxiliary gas 0.6 L min^{-1}, nebulizer gas 1.2 L min^{-1}	SF	$^{28}Si^{+}$	5 ms	n/s		216
2017	60, 100 nm citrate- and PVP-coated Ag NPs and their aggregates	$NaNO_3$ or $NaNO_3$ and $Ca(NO_3)_2$	Dilution or dialysis	MicroMist nebulizer	RF power 1400 W, cooling gas 18.0 L min^{-1}, auxiliary gas 1.30 L min^{-1}, nebulizer gas 1.44 L min^{-1}	Q	n/s	10 ms	n/s		217
Other Applications											
2016	Cu_2O NPs	Antifouling paint	Dilution, sonication	n/s	n/s	Q	n/s	0.1 ms	n/s		218

Table 2.2: Continued.

Year	NP types analyzed	Matrix	Sample preparation	Nebulizer and spray chamber	Plasma parameters	Mass analyzer	Measured isotopes	Dwell time	Size L_D (ESD)	Features	Reference
2016	Ag NPs	Release from plastic food containers into food simulants (Milli-Q water, 10% ethanol, 3% acetic acid)	Incubation	n/s	Sampling position 7 mm	n/s	n/s	3 ms	n/s		219
2016	Ag NPs	Release from plastic food containers and baby feeding bottle into food simulants (Milli-Q water, 10% and 90% ethanol, 3% acetic acid)	Incubation, sonication, evaporation of ethanol and reconstitution in Milli-Q water	MicroMist Nebulizer, Scott spray chamber	RF power 1550 W, cooling gas 15 L min^{-1}, auxiliary gas 1.2 L min^{-1}, nebulizer gas 1 L min^{-1}	Q	$^{107}Ag^{+}$	10 ms	n/s		220
2016	Ag NPs	Release from nanosilver conductive ink, ink itself	Ink dilution	n/s	n/s	Q	n/s	0.1 ms	n/s		221

Table 2.2: Continued.

Year	NP types analyzed	Matrix	Sample preparation	Nebulizer and spray chamber	Plasma parameters	Mass analyzer	Measured isotopes	Dwell time	Size L_D (ESD)	Features	Reference
2017	Ag NPs	Glass slides coated with Ag NPs, structured SiO_2-based nanocomposites with a single layer of Ag NPs	Ultrapure water extraction and dilution for glass slides; MOPS extraction, algae treatment, centrifugation, dilution for nanocomposites	Glass concentric slurry nebulizer, cyclonic spray chamber	RF power 1200 W, cooling gas 15 L min^{-1}, auxiliary gas 1.2 L min^{-1}, nebulizer gas 1.0 L min^{-1}	Q	$^{107}Ag^+$ and $^{109}Ag^+$	5 ms	24 to 40 nm		222
2017	10, 20, 30, 40, 50, 60, 70, 80, 100 nm PVP-coated Ag NPs	Spiked lake, tap waters; liquid consumer products, migration solutions from plasters	Extraction with in pure water by ultrasonication or in sweat simulants for plasters, dilution	Cyclonic spray chamber, Meinhard concentric nebulizer	n/s	Q	$^{107}Ag^+$	50 µs	12-15 nm		157
2017	Ag NPs	Toothbrushes	Release of NPs to tap water	n/s	Sampling position 7 mm	n/s	n/s	3 ms	35 nm		223

Table 2.2: Continued.

Year	NP types analyzed	Matrix	Sample preparation	Nebulizer and spray chamber	Plasma parameters	Mass analyzer	Measured isotopes	Dwell time	Size L_D (ESD)	Features	Reference
2017	TiO_2 NPs	Textiles (table placemats, wet wipes, microfiber cloths, baby bodysuits)	Release of NPs to deionized water, sonication, shaking, dilution and addition of Triton-X	n/s	n/s	n/s	$^{48}Ti^+$, $^{44}Ca^+$	0.1 ms	27-33 nm		224
2017	Iron based Fe_2O_3 nanopigment	Nanopigments in polymer matrix: release from cryo-milled debris into Milli-Q water, moderately hard water, water with a humic acid	Rotation end over end	MicroMist nebulizer	RF power 1550 W, cooling gas 15 L min^{-1}, auxiliary gas 0.19 L min^{-1}, nebulizer gas 0.98 L min^{-1}	Q with KED (H_2)	$^{56}Fe^+$	5 ms	n/s		225
2017	Ag NPs	Release from antibacterial leather and leatherette into Milli-Q water	Milli-Q water extraction	n/s	n/s	Q	$^{107}Ag^+$	0.05 ms	n/s		226

Table 2.2: Continued.

Year	NP types analyzed	Matrix	Sample preparation	Nebulizer and spray chamber	Plasma parameters	Mass analyzer	Measured isotopes	Dwell time	Size L_D (ESD)	Features	Reference
2017	TiO_2, Al_2O_3, Cu-phthalocyanine, CuO NPs	Tattoo inks	Dilution	PFA-ST nebulizer	RF power 1400 W, cooling gas 15 L min^{-1}, auxiliary gas 1.2 L min^{-1}, nebulizer gas 1.05 L min^{-1}	Q with KED (He)	$^{27}Al^+$, $^{63}Cu^+$, $^{47}Ti^+$	5 ms	n/s		227
2017	Mo-, Fe-containing NPs	Asphaltene solutions	Dilution with *o*-xylene, sonication	Concentric glass nebulizer	RF power 1600 W, nebulizer gas 0.35 L min^{-1}, option gas 0.35 L min^{-1} (Ar, 80%; O_2, 20%), sampling position 10 mm	TQ	$^{51}V^+$, $^{56}Fe^+$, $^{60}Ni^+$, $^{95}Mo^+$	0.1 ms	n/s		228

Table 2.2: Continued.

Year	NP types analyzed	Matrix	Sample preparation	Nebulizer and spray chamber	Plasma parameters	Mass analyzer	Measured isotopes	Dwell time	Size L_D (ESD)	Features	Reference
2017	Pt/SiO_2 nanocomposite with ultra small Pt NPs	Pt/SiO_2 nanocomposite	Dilution	MicroMist pneumatic nebulizer, Scott-type spray chamber	RF power 1500 W, nebulizer gas 1.05 L min^{-1}, sampling position 8.0 mm	Q with KED (He)	$^{195}Pt^+$	10 ms	17.2 nm Pt		229
2018	Al-, Si-, Ti-containing NPs	Release from ceramic cookware during simulated linear abrasion	Wash with Liquinox, release to 3% acetic acid, dilution	MicroMist nebulizer	n/s	TQ	$^{27}Al^+$, $^{28}Si^+$, $^{48}Ti^+$	3 ms	n/s	H_2 was used as a reaction gas	230
2018	Ag NPs	Consumer sprays	Dilution	n/s	n/s	Q	n/s	10 ms	17.3-35.3 nm		231

Table 2.2: Continued.

Year	NP types analyzed	Matrix	Sample preparation	Nebulizer and spray chamber	Plasma parameters	Mass analyzer	Measured isotopes	Dwell time	Size L_D (ESD)	Features	Reference
2018	Sb-, Pb-, Ba-containing NPs	Gunshot residue wash from shooters´hands	Wash with ultrapure water with 0.2% formaldehyde or hand swabbing with cotton swabs and sonication	n/s	n/s	Q	$^{121}Sb^+$, $^{137}Ba^+$, $^{208}Pb^+$, $^{121}Sb^+$ and $^{137}Ba^+$, $^{121}Sb^+$ and $^{208}Pb^+$, $^{137}Ba^+$ and $^{208}Pb^+$, $^{206}Pb^+$ and $^{208}Pb^+$, $^{207}Pb^+$ and $^{208}Pb^+$, $^{206}Pb^+$ and $^{207}Pb^+$	29 µs, 30 µs for lead isotopes	n/s	Single and dual element modes were used. Two isotopes monitoring with 145 µs settling time, 150 µs settling time for lead isotopes	232
2018	As-containing NPs	Cigarette smoke	Smoke collection with electrostatic trapping, wash with methanol, dilution with deionized water	Dual-port spray chamber	n/s	Q	$^{75}As^+$	0.1 ms	n/s	No As-containing NPs were found	233

Table 2.2: Continued.

Year	NP types analyzed	Matrix	Sample preparation	Nebulizer and spray chamber	Plasma parameters	Mass analyzer	Measured isotopes	Dwell time	Size L_D (ESD)	Features	Reference
2018	Biogenic Se NPs; 50, 100 nm Se NPs	Se-rich yeast	Enzymatic digestion with Driselase, protease	Concentric nebulizer, cyclonic spray chamber	RF power 1550 W, cooling gas 15 L min^{-1}, auxiliary gas 0.9 L min^{-1}, nebulizer gas 1.10 L min^{-1}	Q with KED (H_2)	$^{78}Se^+$, $^{80}Se^+$	5 ms, 0.1 ms	18 nm		234
2018	Cu NPs	*Cuprum metallicum*, *Gelsemium sempervirens* homeopathy medicines	n/s	n/s	n/s	Q	n/s	n/s	45 nm Cu, 52 nm Cu_2O		235
2019	Niobium and titanium carbonitride particles	Microalloyed steel	Etching in H_2SO_4 and Disperbyk-2012, centrifugation to remove dissolved iron, dilution	Pneumatic nebulizer, cyclonic spray chamber	n/s	TOF at 555 Hz	MA, $^{48}Ti^+$, $^{93}Nb^+$	n/a	27.5 nm NbCN, 50.5 nm TiNbCN		236

Abbreviations:

AF4 – asymmetrical flow field-flow fractionation, BPEI – branched polyehyleneimine, BSA – bovine serum albumin, CIGS – copper indium gallium selenide cells, CNT – carbon nanotube, CPE – cloud point extraction, DMEM – Dulbecco's modified eagle medium, EPA – Environmental Protection Agency, ESD – equivalent spherical diameter, HDC – hydrodynamic chromatography, IEC – ion-exchange column, KED – kinetic energy discrimination, LA – laser ablation, L_D – detection limit, MA – multielemental analysis, MOPS – 3-morpholinopropane-1-sulfonic acid, n/a – not applicable, n/s – not specified, NOM – natural organic matter, OECD – The Organization for Economic Co-operation and Development, OPV – organic photovoltaic cells, PBS – phosphate buffered saline, PEG – polyethylene glycol, PFA – perfluoroalkoxy alkane, PTFE – polytetrafluoroethylene, PVA – polyvinyl alcohol, PVP – polyvinylpyrrolidone, Q – quadrupole, RF – radio frequency, SDS – sodium dodecyl sulfate, SF – sector field, TAP – tris-acetate-phosphate, TMAH – tetramethylammonium hydroxide, TOF – time-of-flight, TQ – triple quadrupole, TSPP – tetrasodium pyrophosphate, WWTP – waste water treatment plant.

Note that the entries are grouped by the matrix that is the main focus of an article. The table does not contain the paper on SP-ICP-MS method development.

2.4 Conclusion

The past two decades have witnessed the commercial realization of new and powerful ICP-MS instrumentation and methods, including instruments with faster data acquisition, enhanced detection power, alternative mass analyzers, off-the-shelf interfaces to couple LC, CE etc. to ICP-MS, and novel separation and fractionation methods. While these instruments were successfully used for nanomaterials characterization and the numbers of SP-ICP-MS papers are steadily increasing, there are some remaining challenges that have to be addressed to ultimately reach the top of the peak.

Total consumption microflow nebulizers or droplet generators are attractive due to a high particle transport efficiency. However, microflow nebulizers sometimes suffer from clogging (in the presence of agglomerates or organic matter) and commercially available droplet generators reportedly suffer from a limited day-to-day reproducibility and can not be coupled to autosamplers today. Future research in the area of sample introduction for both stand-alone SP-ICP-MS and when interfaced to separation methods (e.g. CE-SP-ICP-MS) is encouraged to address these and other challenges with the ultimate goal of a high-throughput and robust sample introduction system for single particle (and single-cell) ICP-MS. While sample introduction is a potential source of error, sample preparation play is often overlooked but may even play a bigger role, especially when PNC ought to be determined. Here, more fundamental studies on potential analyte losses and species transformation (oxidation, release of ions, change of size, agglomeration) during sampling, storage, and sample preparation are required. For example, a common sample preparation step is filtration to remove unwanted organic matter and larger particle fractions. However, particle losses might occur depending on the particle size and surface coating interaction with the filter material and are often overlooked when PNCs are reported. Similarly to conventional analytical methods, the analyte (particle) recovery should become a parameter that is always reported in future SP-ICP-MS studies.

Based on the publications discussed in this chapter, the author would like to stress that a careful optimization of the plasma conditions and dwell time is

required to achieve better NP size detection limits and accurate particle size and number information, respectively. In addition, instrumental developments to improve the ion sampling/transfer efficiency in ICP-MS would help to further decrease the size detection limits for single particles and also to gain access to information on NPs of mixed elemental composition and core/shell materials.

While quadrupole-based ICP-MS systems were widely used in past SP-ICP-MS studies, we assume that mass analyzers that provide fast time-resolved and multi-elemental detection such as ICP-time-of-flight-MS systems will play in important role in this field in the future. However, even the best instrument is worthless if it cannot be calibrated properly, and the community of SP-ICP-MS users is often discussing the lack of appropriate reference materials at scientific conferences. In the future, the field would benefit from more well-characterized and certified nanomaterials to assure accurate and precise quantification.

It can be concluded that SP-ICP-MS is a very useful method for NPs analysis today but there is still room for fundamental studies, instrumental improvements, and methodological advances to come closer to what would be the “ideal method” for nanomaterials characterization.

Chapter 3

Implementation of Online Preconcentration and Microsecond Time Resolution to CE-SP-ICP-MS

Based on:

D. Mozhayeva, I. Strenge, C. Engelhard, Implementation of Online Preconcentration and Microsecond Time Resolution to Capillary Electrophoresis Single Particle Inductively Coupled Plasma Mass Spectrometry (CE-SP-ICP-MS) and its Application in Silver Nanoparticle Analysis,

Anal. Chem., 2017, **89**, 7152-7159.

3.1 Introduction

ICP-MS is a sensitive elemental analysis technique that can be utilized for NP analysis. Different separation techniques can be coupled to ICP-MS for size separation and, in some cases, speciation of NP mixtures. Liquid chromatography (LC) coupled to ICP-MS for NP analysis enables speciation of ionic metal species from NPs.[237-240] Helfrich *et al.*[237, 238] introduced LC-ICP-MS for the analysis of Au NPs and were able to separate ionic gold, 5, 10, and 20 nm sized NPs from each other. Soto-Alvaredo *et al.*[239] applied the technique for Ag and Au NPs mixtures up to 40 nm in size. In LC-ICP-MS analyses, however, any possible unwanted interaction of NPs with the stationary phase should be carefully taken into consideration. Also, the limited applicable NP size range and the chromatographic resolution currently achieved may be a concern for the analysis of suspensions containing NPs of vastly different sizes or more complex mixtures. HDC can also be coupled to ICP-MS for NP analysis[95, 101, 102, 241-244] and applied for NP separation over a wide size range (e.g., from 3 to 250 nm sized Au NPs).[241] Similar to LC-ICP-MS, however, the method is currently limited by a relatively low resolution. FFF is widely used for NP online fractionation prior to ICP-MS analysis.[245-253] FFF provides size dependent NP fractionation, for that reason NP size distributions information can also be obtained at a wide size range from 10 to 110 nm for Ag NPs.[248] Although quantification is not straightforward in FFF, Meermann *et al.*[249] introduced an approach using online isotope dilution and achieved L_D of 0.5 µg L^{-1} for Ag.

CE can be used to separate NP based on their size due to different electrophoretic mobilities that are directly proportional to particles' charge-to-size ratio. Therefore, a relatively high resolving power can be achieved because the separation is not only governed by size, but additionally by the NP charge. Capillary zone electrophoresis (CZE), which will be referred to as CE in this thesis, is one of the prominent CE separation modes. Separation of polystyrene latex particles in the mixtures containing seven different types of particles from 30 to 1160 nm in diameter with CE was accomplished already in 1990 by Jones and Ballou.[254] In 2004, Liu and Wei[255] reported that the addition of SDS to a 3-cyclohexylamoniuopropanesulfonic acid (CAPS) buffer improves the separation

power of the method for Au NPs mixtures analysis, and 5.3 and 19 nm sized Au NPs were successfully separated. Later it was found that SDS in the separation buffer also assists Ag NPs separation.[256] The presence of SDS surfactant with a concentration higher than the critical micelle concentration in the separation buffer changes the separation mode to micellar electrokinetic chromatography (MEKC). A strong electroosmotic flow (EOF) towards the cathode (outlet vial), which is generated under basic conditions, is faster than the flow of micelles (towards the anode). Thus, smaller NPs have shorter migration times (MTs) in an electropherogram, compared to larger ones.

Due to the fundamental principles of CE (typically only thin capillaries with 50 to 100 μm inner diameter are used), only a relatively low sample injection volume in the nL-range is used, which ultimately dictates the method's lower L_D. There are two ways to improve this: one way is to use a more sensitive detector compared to the widely used UV/vis absorbance detector, the other way is to pre-concentrate the analytes. Coupling of CE to ICP-MS for Au and Ag NP analysis was introduced recently:[257] the developed method enabled the separation of 5, 20, and 50 nm sized Au NPs along with the speciation of ionic gold from NPs with the use of penicillamine as a complexing agent. The separation buffer composed of 10 mM CAPS and 60 mM SDS at pH 10 was chosen as an optimal one.

In recent years, a number of online preconcentration approaches in CE have appeared. These techniques and their applications are frequently reviewed.[258, 259] One of the techniques that can be used for NP preconcentration is the REPSM, which was developed for MEKC in 1994,[260] and its fundamental principles were described in detail later by Quirino and Terabe.[261] REPSM preconcentration was successfully applied for Au NPs allowing to increase the injection time first to 24 s,[262] and then to 50 s.[263-265] REPSM injection time optimization showed that CE injection times longer than 50 s resulted in a decrease of the number of theoretical plates and resolution in a study of Au NPs analysis (using a diode array detector).[265]

The underlying concepts and recent applications of SP-ICP-MS were summarized in a recent reviews.[8-10] Because the signal of a particle's ion cloud that

is detected is considered to be proportional to the particle's mass, the size of a NP may be deduced (assuming spherical shape, bulk material density, etc.). The two most common approaches for PNC determination in SP-ICP-MS are external calibration with standards of known PNC[7] or the determination of the analytes transport efficiency.[266] The performance and data quality of SP-ICP-MS heavily depends on the selection of the DT (literature reports between 0.1 and 10 ms) and the following data processing. For example, if the DT is too short, one NP signal may be recorded only partially (split-particle events), and, if the DT is too long, two or more NPs may be detected as one (particle coincidence). To overcome these and other artifacts, a data acquisition system was developed in the group that allows recording the signals for one isotope continuously with up to 5 µs time resolution with a 100% duty cycle. It was further demonstrated that the prototype -µsDAQ helps to decrease the BG signal in SP-ICP-MS size distribution diagrams, and to extend the PNC-range of suspensions that can be measured without artifacts.[11]

The main challenge for coupling NP separation techniques to SP-ICP-MS is the fact that the separation channel increases the number of particles that are entering the ICP in rapid succession (e.g., short elution periods in a chromatogram that result in sharp peaks). Because the probability of particle coincidence now drastically increases, the choice of DT and separation conditions is crucial to obtain accurate particle information. A proof-of-principle study for HDC-SP-ICP-MS was performed by Pergantis et al.,[95] where 30 and 60 nm sized Au NPs were separated (DT of 10 ms). Coupling of electrospray - differential mobility analysis to SP-ICP-MS provides a possibility to separate Au NPs from 30 to 100 nm in size also using 10 ms DT.[97] The first results on CE coupled to SP-ICP-MS were obtained by Franze et al. in an example of Au NPs (10, 30, 60 nm) analyses, still with a rather long DT of 2 ms.[98]

In the current chapter, a sensitive method for Ag NPs separation and characterization that is based on CE-SP-ICP-MS combined with a novel prototype data acquisition system (µsDAQ) providing microsecond time-resolution was developed. Separation and coupling conditions were carefully optimized to allow the introduction and optimization of a REPSM online preconcentration technique prior to CE separation.

3.2 Experimental Section

3.2.1 Sample Preparation

Monodisperse spherical Ag NPs with nominal diameters of 20 (18.5 ± 3.4) nm, 40 (39 ± 4) nm, and 60 (62 ± 7) nm stabilized in 2 mM citrate were acquired from nanoComposix (San Diego, CA, U.S.A.; 0.020 g L^{-1} initial Ag concentration). The samples were stored at 4 °C in darkness prior to analysis and shaken for 30 s prior dilution. Dilutions to desired concentrations were performed with bi-distilled deionized water on the day of analysis.

The buffer for CE separation contained 60 mM SDS (99.5% pure for electrophoresis, Carl Roth, Karlsruhe, Germany), 10 mM CAPS (99%, Carl Roth, Karlsruhe, Germany), and 10 µg L^{-1} Cs (Inorganic Ventures, Christiansburg, VA, U.S.A.) at pH 10, adjusted by addition of 1 M NaOH (98.8%, Th. Geyer, Renningen, Germany), and controlled by a pH meter (Multi 340i/SET, WTW, Weilheim in Oberbayern, Germany). Buffer and 1 M NaOH (used for capillary activation) were filtered with 0.45 µm polytetrafluoroethylene (PTFE) syringe filters (VWR International, Darmstadt, Germany). A fresh buffer was prepared once per week and stored at 4 °C in darkness prior to analysis. Sheath liquid consisted of 10 µg L^{-1} indium (Inorganic Ventures, Christiansburg, VA, U.S.A.) and 2% HNO_3 (70%, Fisher Scientific, Loughborough, U.K.). $NaNO_3$ (99%, J.T. Baker, Deventer, The Netherlands) was used for the preparation of NPs Na^+ matrix matched standards in SP-ICP-MS measurements.

3.2.2 Instrumentation

A model G7100A (Agilent Technologies, Waldbronn, Germany) CE system with polyimide-coated fused-silica capillary (75 (77.7. ± 0.2) µm i.d., 375 µm o.d., 70 cm length; Polymicro Technologies, Phoenix, AZ, U.S.A.) was coupled to a model iCAP Qc (Thermo Fisher Scientific, Bremen, Germany) quadrupole ICP-MS instrument. The coupling was performed by connecting the CE capillary outlet to the inlet of a model DS-5 microflow nebulizer (Teledyne CETAC Technologies, Omaha, NE, U.S.A.) via a 1.00 mm bore polyether ether ketone (PEEK) crosspiece

(Macherey-Nagel, Düren, Germany) (Figure 3.1). The self-aspirating nebulizer is supplied with a low-volume spray chamber. The crosspiece serves to merge the CE flow with sheath liquid to provide stable aspiration and to close the CE electrical circuit via an electrical cable from the outlet electrode attached to a stainless-steel wire (the upper crosspiece inlet). The contact of sheath liquid with the wire in the crosspiece ensures grounding. The CE instrument was controlled with the Agilent OpenLab CDS (C.01.07, Agilent Technologies), the ICP-MS instrument with the Qtegra ISDS (2.4.1800.192, Thermo Fisher Scientific) software.

ICP-MS operating conditions were chosen to achieve high sensitivity for NPs. Therefore, a second roughing pump (Sogevac SV40 BI, Leybold, Cologne, Germany) was connected to the first pump in order to achieve a lower interface pressure of 1.22 ± 0.06 mbar. Additionally, a high sensitivity skimmer insert (insert "2.8", Glass Expansion, Melbourne, Australia) was installed. The most important ICP-MS parameters are listed in Table 3.1.

The CE system was operated at voltages from 10 to 25 kV with hydrodynamic injection at 50 mbar for 3 s without polarity switching and for 10 to 150 s in REPSM. Implementation of REPSM preconcentration after injection is achieved by switching the voltage to negative polarity with the same absolute value as in the corresponding CE run. The measured current will then steadily

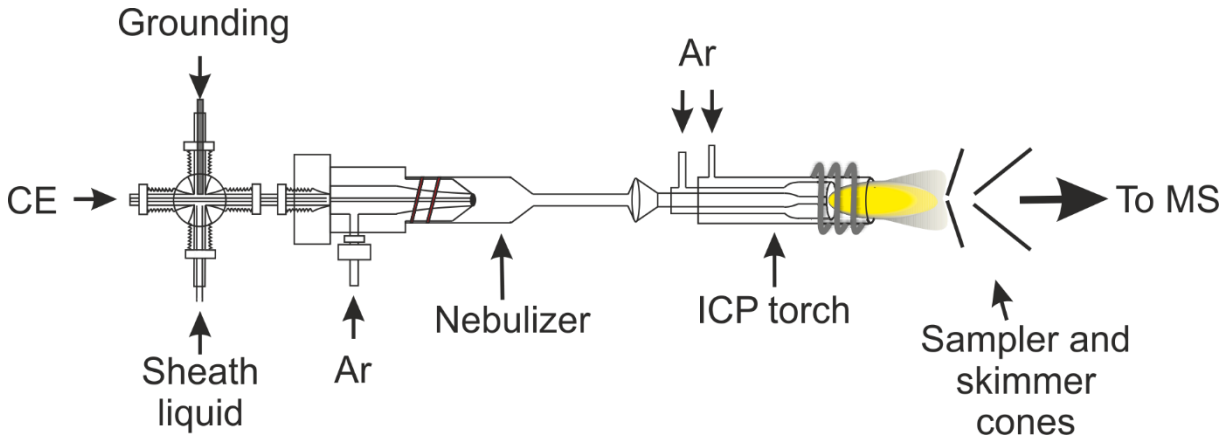

Figure 3.1: CE-ICP-MS coupling setup schematic.

increase. When the current reaches 90-95% of the typical value, the voltage polarity is switched again, and a positive voltage is applied throughout the CE run.

Before the first measurement of a day, capillaries were activated by rinsing them with 1 M NaOH, bi-distilled deionized water, and separation buffer for 10 min each. Before each run the capillary was flushed with the running buffer at 950 mbar for 1 min. To ensure that the sheath liquid flow is restored after the flushing step, a decrease of the $133Cs^+$ signal (separation buffer) and an increase of the $^{115}In^+$ signal (sheath liquid) to their initial values were monitored before the start of each measurement.

Table 3.1: Main ICP-MS instrumental parameters.

Parameter	**Value**
RF power	1450 W
Ar cooling gas flow	14 L min^{-1}
Ar auxiliary gas flow	0.8 L min^{-1}
Ar nebulizer flow	0.8 L min^{-1}
Sampling position	3.5 mm
Torch injector inner diameter	1.5 mm

3.2.3 CE Injection Volume Determination

To determine the CE injection volume from hydrodynamic injection, an indium-free 2% HNO_3 sheath liquid was utilized, and 10 µg L^{-1} indium was added into a sample vial. The sample was injected at 50 mbar until $^{133}Cs^+$ would interchange with $^{115}In^+$ signal from the sample. The period of time between $^{133}Cs^+$ signal rise and $^{115}In^+$ signal rise was recorded 12 times. With a known capillary length (70 cm), the sample velocity during the 50 mbar injection was calculated to be 1.57 ± 0.03 mm s^{-1}. Knowing the injection time and the dimensions of the capillary, the injection volume was calculated and used to determine the number of injected particles in selected experiments using the PNC of the NP suspensions (as provided by the manufacturer).

3.2.4 Data Acquisition and Data Processing

Two different data acquisition strategies were used simultaneously. The vendor DAQ/software was used to monitor several isotopes between the CE runs (sheath liquid stability check, etc.). The home-built µsDAQ[11] was used with 5 µs DT during $^{107}Ag^{+}$ isotope detection throughout each CE run, and data were acquired continuously, e.g., for up to 40 min. All CE-SP-ICP-MS measurements were performed in triplicates, if not specified otherwise.

With a DT of 5 µs the signal of each particle (which typically appears as a series of counts in quick succession) is expected to be spread out over a number of consecutive dwells. Therefore, additional processing of the data acquired with the µsDAQ is necessary to obtain information on a per-particle basis. The application of a simple threshold criterion has been found to be suitable for the identification of virtually all particle-related signals in the time-resolved data from CE runs: A particle is registered anytime the number of counts in a certain number of dwells exceeds a predefined threshold limit. Subsequent consecutive dwells are treated as belonging to this transient until the threshold condition is not fulfilled anymore. The combined signal for each particle is obtained by summing up the signal of all consecutive 5 µs dwells throughout the corresponding event. Processing of the raw data was performed with a command line tool written in "C".[11] The resulting dataset for each CE run contained a list of the exact points in time a particle occurred, the combined signal for each particle, as well as the corresponding time-resolved ion cloud profile. Further data processing and graphical representation of the results was done in Origin 2015 (OriginLab Corporation, Northampton, MA, U.S.A.).

Size calibration was performed every day by measurements of individual 20, 40, and 60 nm sized Ag NPs suspensions with SP-ICP-MS, and construction of a calibration curve with linear fit ($R^2 = 0.9987 \pm 0.0011$) using the mean particle size provided by the manufacturer. After size calibration, data sets were further reduced by binning the data in size and time dimensions and counting the number of NP events that fall into each bin. Bins of 2 nm × 10 s were found to be optimal for Ag NPs analysis. After binning, visual representation of the results is possible

by construction of two-dimensional color maps. Construction of a conventional CE-ICP-MS diagram is still possible by subsequently reducing the time resolution of acquired SP-ICP-MS data. To obtain a desired DT, the corresponding signals of multiple consecutive dwells are simply summed up (Figure A.1B).

3.3 Results and Discussion

3.3.1 The Effect of CE Separation Conditions on NP Ion Clouds Profiles

When CE is coupled to ICP-MS, matrix effects, which can change the signal response of NPs events, may arise from the introduction of the separation buffer (organic matrix) into the plasma. Additionally, SDS contains sodium, which has a low ionization potential. The presence of easily ionizable elements (EIE) such as sodium from a 60 mM SDS buffer in the plasma may suppress the ionization of elements with higher ionization potentials such as silver. To ensure that the ionization efficiency of Ag NPs is not affected by the presence of organic compounds and Na^+ in the ICP, ion cloud profiles and the average duration of ion clouds were compared for 20, 40, and 60 nm sized Ag NPs during a CE run and with stand-alone SP-ICP-MS measurements of Ag NPs in different matrices (bi-distilled water, and 4.7 mM $NaNO_3$ solution). The latter was chosen as a sodium matrix-matched standard, because it featured a similar $^{23}Na^+$ response in the ICP-MS, compared to the $^{23}Na^+$ signal during a CE separation. It was found that when Ag NPs were analyzed in the presence of Na^+ in suspension, the average size of NPs and the average NP ion cloud duration did not change significantly. However, the Ag BG signal slightly increased, compared to NPs suspensions prepared in water. Ten time-resolved ion cloud profiles of particle events that show a signal close to the mean of the corresponding signal distribution were compared more closely for each analyzed suspension. As exemplarily shown for the 60 nm sized Ag NPs (Figure 3.2), it was found that the duration of these ion clouds did not change significantly with the different sample matrices (see above). This indicates that the CE separation conditions do not cause a significant change in response, i.e. broadening of the NPs ion clouds, and, in turn, a size calibration in CE-SP-ICP-

MS can be performed by the analysis of Ag NPs suspensions in water with SP-ICP-MS.

3.3.2 CE-SP-ICP-MS Capabilities

Coupling of a NP separation technique to SP-ICP-MS provides valuable additional information on the separation features of the technique. Figure 3.3 presents all qualitative and quantitative information that can be obtained from two-dimensional CE-SP-ICP-MS color maps. Due to an additional size domain in CE-SP-ICP-MS, CE migration profiles and average MT can be extracted at each desired size or size range, for example, the CE profile at 39 nm is presented in

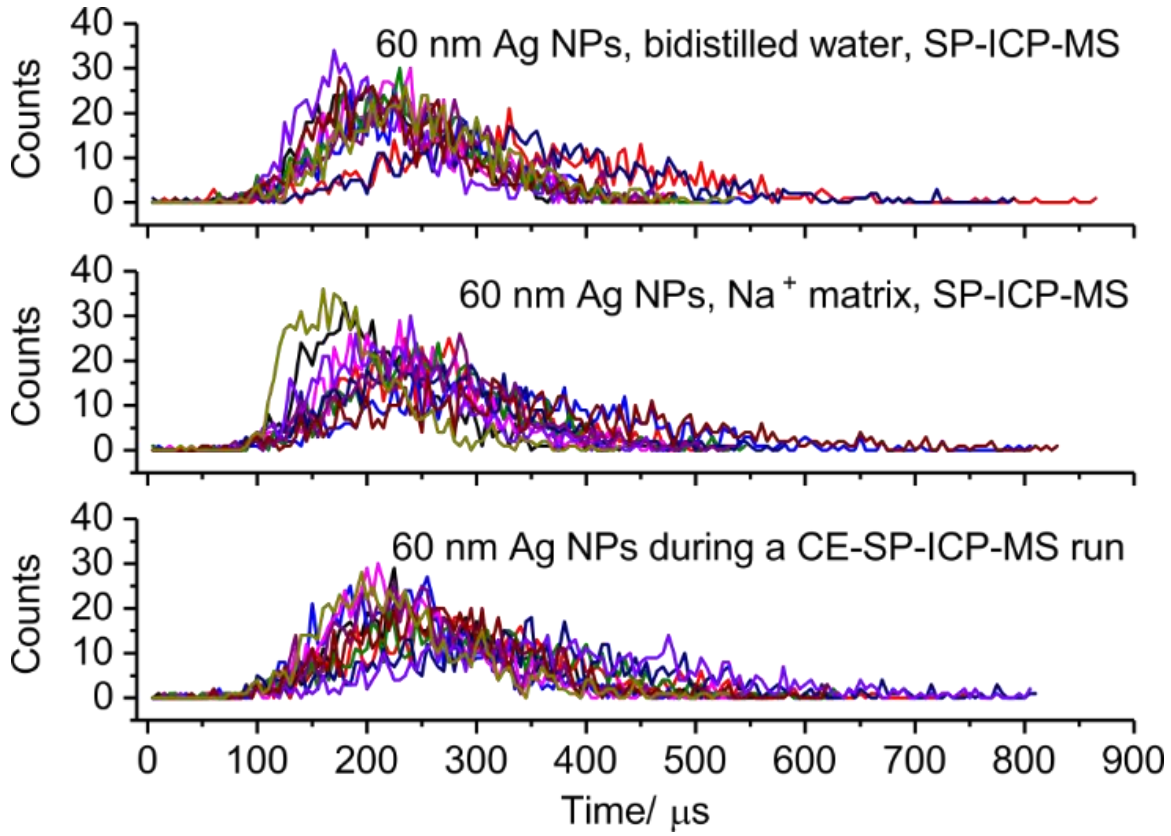

Figure 3.2: Ion clouds profiles (n = 10, $^{107}Ag^{+}$) of 60 nm sized Ag NPs obtained by SP-ICP-MS analysis of NPs diluted in bi-distilled water (top), in 4.7 mM Na^{+} matrix (middle) both with standard sample introduction, and during a CE-SP-ICP-MS run (bottom). Data was acquired with the µsDAQ and a DT of 5 µs, each ion cloud consists of approximately 730 counts.

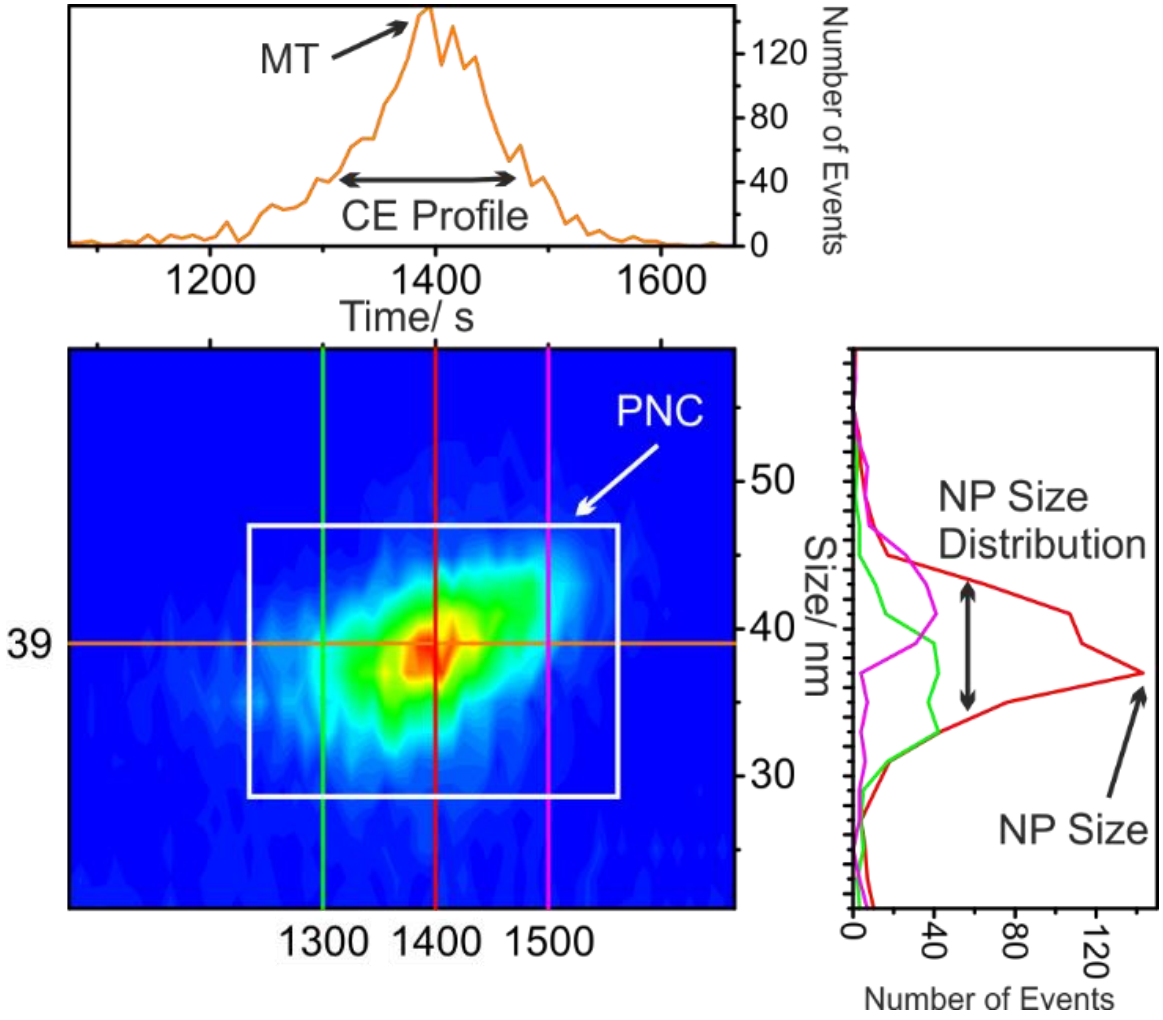

Figure 3.3: CE-SP-ICP-MS data evaluation capabilities and obtained characteristics presented for 40 nm sized Ag NPs. Total number of particles in boxed-in area: approximately 10,000.

Figure 3.3 (top insert). This feature provides a complementary tool to judge the CE separation quality and to check whether or not peaks are symmetrical, with no tailing or fronting. In addition, the NPs size profile on the y-axis gives information on the average NP size and the size distribution. Size distributions can also be extracted at different points in time during a CE run. Three different size distribution plots are shown (Figure 3.3, right insert), which indicate that the mean size of the NPs migrating at 1300 s (line in green color) is smaller compared to NPs at 1400 s (line in red color). Consequently, the NPs with even larger sizes migrate at 1500 s (line in magenta color), which indicates that the investigated

citrate-capped Ag NPs migrate according to their size. The number of events detected in each 2 nm × 10 s bin is presented by different colors in the diagram, with the highest number detected at 39 nm and 1400 s. As the CE profile and the NP size distribution have finite shapes, the total number of detected NPs at chosen size and time intervals (boxed-in by white frame in Figure 3.3) can be related to PNC (assuming stable nebulizer conditions and analyte transfer efficiency, etc.). In order to perform PNC quantification, calibration with known PNC is required. CE-SP-ICP-MS increases the resolution between the studied NPs approximately twice compared to CE-ICP-MS. Conventional CE-ICP-MS diagrams can also be derived by summing up all particle events in a certain time frame (Figure A.1A), or all signals (vendor software) in a certain time frame (Figure A.1B).

Consequently, CE-SP-ICP-MS, compared to separation techniques coupled to ICP-MS, provides not only separation of NPs by means of CE but also the straightforward capabilities to determine NP size and PNC in each chosen region.

3.3.3 REPSM Method Development

Preconcentration techniques in CE, REPSM in particular, further increase the local concentrations of analytes in comparison with conventional CZE separation. Therefore, optimization of REPSM conditions is required in order to achieve SP detection in CE-SP-ICP-MS with minimum time-overlap of individual ion clouds. Typically, CZE utilizes short hydrodynamic injections (usually only a few seconds), and analytes migrate as thin zones during separation, therefore, their separation can be achieved. When a sample is injected for a longer time duration into the capillary (e.g., injection with 100 s at 50 mbar fills a length of 15.7 ± 0.3 cm of a 70.0 ± 0.5 cm capillary with an aqueous sample), the dimensions of the capillary do not allow the analytes to be separated from each other, so they migrate as one front. One approach to achieve the separation of analytes even when using a long injection time is to pre-concentrate the analytes at the beginning of the capillary by matrix removal using REPSM. Additionally, the use of MEKC enhances the separation process because the analytes are interacting with the pseudostationary micellar phase, and the preparation of samples in a low

conductivity matrix promotes the stacking process because the sample plug experiences a higher field strength in comparison with a buffer.

In the early publications on REPSM,[260, 261] a negative voltage (with respect to the outlet vial) was applied to the inlet vial after a sample was injected to remove the sample matrix (until current reaches 97-99% of the typical current at given experimental conditions) and to pre-concentrate the sample at the beginning of the capillary. If the current exceeds the current values that are typical for CE running conditions, this implies that analytes are starting to migrate into the inlet vial. In the context of this chapter, this would lead to an underestimation of the number of detected particles. Therefore, REPSM conditions were optimized as follows. It was found at injection time durations longer than 50 s, if the current reaches a level of 97-99% during preconcentration, the migration profiles of the large particles (namely 60 nm sized Ag NPs) change, become extremely narrow, and particle detection results in SP-ICP-MS are distorted. In order to avoid a high local NP count increase, the preconcentration was performed only until the current reaches 90-95% of the usual value. At these conditions, NPs CE profiles become slightly broader, and particle coincidence during detection can be prevented for a wider NP concentration range. In order to determine an optimum NP injection time with REPSM, the number of detected particles was determined for each NP size and injection times between 10 and 150 s (Figure 3.4). The number of detected NPs increases for all analyzed NP types with increasing injection time. Nevertheless, at injection times higher than 90 s, the rate of the increase reduces, that is why a logistic function was used for fitting of the data. When a 150 s injection time was used, current instabilities during runs started to occur. This is why higher injection times were not tested. This phenomenon may be explained by disruption of the electrical double layer on the surface of the capillary (created by a charged buffer) by long injections of low conductivity sample suspensions.

The resolution between the investigated NPs in CE-SP-ICP-MS two-dimensional diagrams stays at the same level at each tested injection time with REPSM. To avoid current instabilities during the measurements but to still achieve a significant increase in the number of detected particles compared to 3 s injection, an injection time of 110 s was chosen for further REPSM experiments

with the injection length being 17.3 ± 0.3 cm of the total capillary length. This relatively long injection time was feasible also because CE-SP-ICP-MS provides increased resolving power. This is an approximately two-fold longer injection time compared to previously published work (50 s injection time, REPSM mode) on Au NPs.[264, 265]

Applied voltage in CE is one of the factors that determine the separation rate, the analytes' MT, and the resolution between the compounds in a mixture. Therefore, the effect of the applied voltage during NPs analysis with REPSM was studied from 10 to 25 kV (Figure A.2). The relation between applied voltage and generated current was found to be linear from 10 to 20 kV. At 25 kV the generated current was slightly higher than expected (assuming constant resistivity), and less stable (7.4% relative standard deviation, RSD). The latter effect is assumed to be due to Joule heat, which is generated in the buffer with high ionic strength, but not dissipated as efficiently as at lower currents.

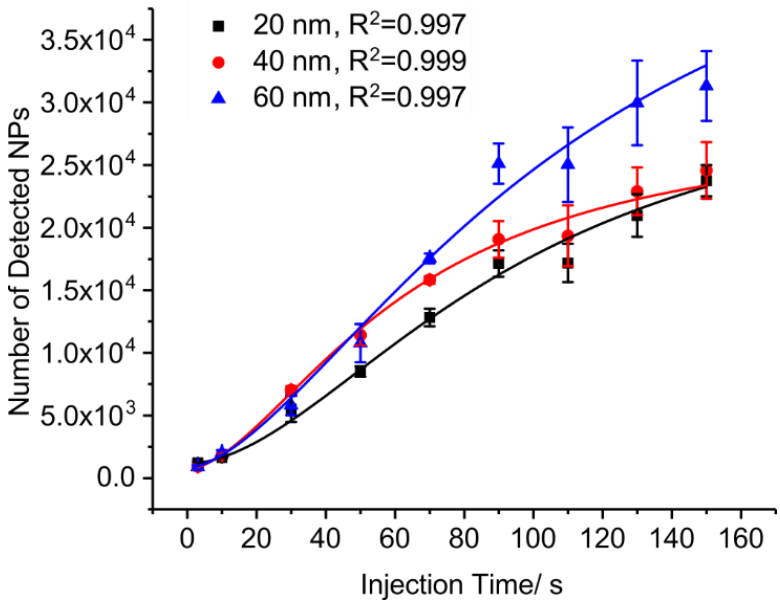

Figure 3.4: Influence of the REPSM injection time on the number of detected particles for a mixture of 5 µg L^{-1} 20 nm sized, 35 µg L^{-1} 40 nm sized, and 200 µg L^{-1} 60 nm sized Ag NPs analyzed at 20 kV (logistic fit).

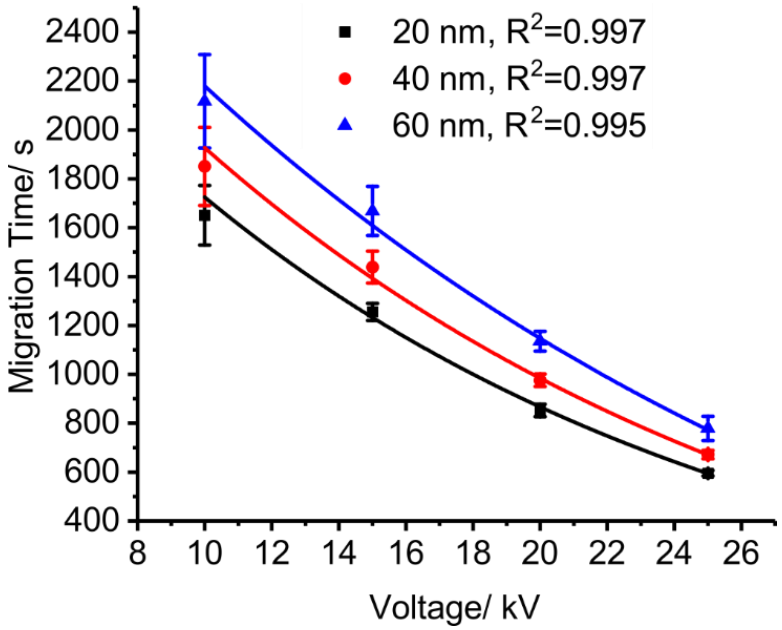

Figure 3.5: Influence of applied voltage on NPs CE MT for a mixture of 10 µg L^{-1} 20 nm sized, 35 µg L^{-1} 40 nm sized, and 100 µg L^{-1} 60 nm sized Ag NPs analyzed using 110 s injection time in REPSM (exponential decay fit).

As the current increases, the mobility of charged species in the buffer and EOF rises. In turn, the MT of NPs is reduced, which could be proved experimentally here for all investigated Ag NPs (Figure 3.5). Variations in MT (indicated by error bars in Figure 3.5) were found to increase with decreasing voltage. This is assumed to be due to stronger longitudinal diffusion towards longer MTs. Although a higher applied voltage of 25 kV results in shorter total analysis time, a value of 20 kV was selected here for further experiments discussed below because of a more effective heat dissipation and stable NP MTs. The stability of MT decreases with increased NP size (MT RSD being 1.9% for 20 nm sized, 2.4% for 40 nm sized, and 6.4% for 60 nm sized Ag NPs).

After method optimization, the optimum conditions for Ag NP preconcentration and separation were determined to be 110 s hydrodynamic injection at 50 mbar, REPSM mode with -20 kV applied (until current reaches 90-95% of the normal current value, approximately 55 s for the tested mixture), and

separation at 20 kV. Total analysis time including the preconcentration step was approximately 28 min.

3.3.4 Quantification of NPs in Mixtures

The developed method was used for the analysis of 20, 40, and 60 nm sized NPs that are simultaneously present in the same mixture. Due to the lack of PNC certified NPs suspensions, PNCs for the used NP suspensions were calculated from Ag mass concentration provided by the manufacturer, taking into account the average NP size determined by TEM, silver bulk density (10490 kg m^{-3}), and respective dilutions. The injection volume for 110 s at 50 mbar hydrodynamic injection was determined to be 819 ± 17 nL. The number of injected particles was therefore calculated from the injection volume and PNC of a suspension that was analyzed. Linear calibration plots could be obtained (Figure 3.6), if the number of detected particles that correspond to each NP size were plotted against the number of injected particles or PNC. The slopes of the obtained linear fits represent the average particle recovery (percentage of NPs detected vs. NPs injected), with values of 12.2 ± 1.4% for 20 nm sized, 17.7 ± 1.5% for 40 nm sized, and 12.2 ± 0.8% for 60 nm sized Ag NPs. The values are relatively low, which might be due to particle losses not only in the CE capillary, but also in the nebulizer/interface and a limited transport efficiency into the ICP-MS. Separate determination of the recovery of only CE separation with the use of REPSM, however, is beyond the scope of this thesis, because the development of an additional method would be required: as the concentrations of NPs are held comparably low to avoid capillary overload and assure particle by particle detection, the fraction collection of specific MT periods would be needed to be performed several times (at least 10) to result in a detectable dissolved silver concentration after digestion. Additionally, the buffer used during CE separation gets into the collected fractions and creates matrix interferences in ICP-MS by artificially increasing the Ag^+ signal. The use of a higher NP concentration to determine the capillary recovery with REPSM, however, will possibly result in capillary overload, leading to increased NP adsorption to capillary walls and, ultimately, to distorted results.

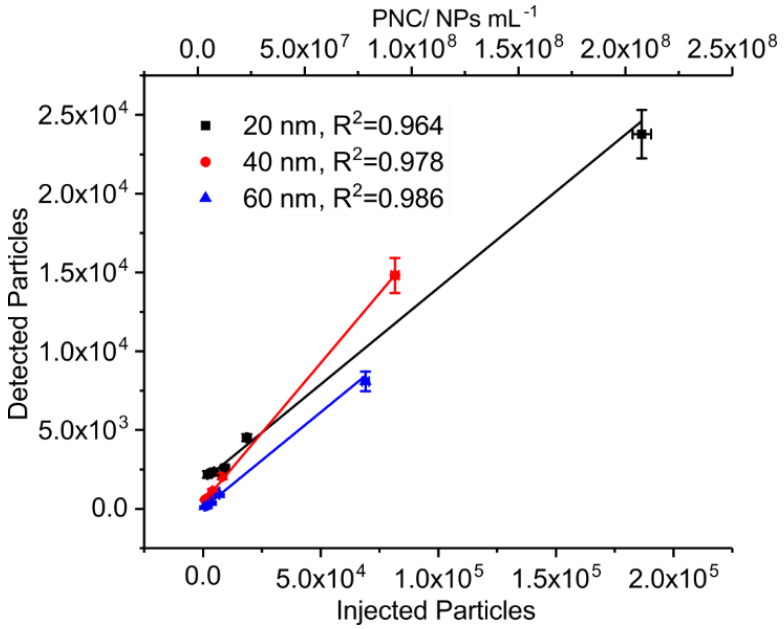

Figure 3.6: The dependence of number of detected particles on number of injected particles and PNC in NPs mixtures for the mixtures of 20 nm sized, 40 nm sized, and 60 nm sized Ag NPs analyzed using 110 s injection time in REPSM at 20 kV (linear fit).

In order to determine the L_D using the calibration curves slopes (Figure 3.6), a blank bi-distilled water sample was measured 10 times with CE-SP-ICP-MS. Consequently, the L_D were determined to be 0.71 µg L^{-1} for 20 nm sized, 0.48 µg L^{-1} for 40 nm sized, and 0.67 µg L^{-1} for 60 nm sized Ag NPs. The higher L_D value for 20 nm sized Ag NPs can be explained by BG noise during SP-ICP-MS detection. Application of other types of preconcentration approaches in CE and improvements in ICP-MS transport efficiency may help to further decrease the obtained L_D in the future and to make the method applicable to all types of environmental samples. The analysis of highly concentrated NP samples (e.g., mg L^{-1}-range) can be performed without a preconcentration step using a conventional short injection time or simple sample dilution.

3.3.5 Preconcentration Efficiency in CE-SP-ICP-MS for Ag NPs Mixtures

The use of REPSM with 110 s injection time allows to pre-concentrate NPs before CE-SP-ICP-MS with higher resolution compared to CE-ICP-MS (Figure A.1). If one compares the results of CE-SP-ICP-MS analysis of a 20, 40, and 60 nm sized Ag NPs mixture with conventional 3 s injection (Figure 3.7A) and 110 s injection with REPSM (Figure 3.7B), the effectiveness of the preconcentration step is apparent. Although, the BG of the measurements stayed the same, it was possible to detect 14 ± 2 times more 20 nm sized, 21 ± 4 times more 40 nm sized, and 28 ± 5 times more 60 nm sized Ag NPs in comparison with 3 s injection. All three NP types are fully resolved, taking into account the broadening in the size dimension due to initial NP size distribution and in the MT dimension due to longitudinal diffusion, especially at longer MTs (60 nm sized Ag NPs). Resolution in two-dimensional color maps was determined by extracting a plane that contains the maxima of both inspected NP profiles and calculating resolution between the two extracted peaks. Although NP resolution slightly decreased with 110 s injection time and the fact that the preconcentration was performed until the current reaches only 90-95% of the typical value (from 1.51 ± 0.48 to 1.28 ± 0.04 between 20 nm and 40 nm sized NPs, from 1.91 ± 0.52 to 1.61 ± 0.18 between 40 nm and 60 nm sized NPs), it is still sufficient to fully resolve the investigated NPs.

Despite the fact that coupling of CE to SP-ICP-MS results in a higher silver BG compared to SP-ICP-MS (due to the organic matrix), it was possible to completely separate 20 nm Ag NPs from the BG.

A further increase in ICP-MS sensitivity and transport efficiency will help to enhance the particle size L_D. Moreover, new strategies to selectively preconcentrate 60 to 100 nm sized NPs could possibly extend the applicability of REPSM to the whole nanoscale. Analysis of dissolved metals along with NPs in CE-SP-ICP-MS still presents a challenge, because the addition of penicillamine as a complexing agent[257] not only affects metal ions but also disrupts SP-ICP-MS detection. Simultaneous multi-isotope detection with high time resolution would allow for the analysis of NPs with different elemental composition to be carried out

in a single run. After further developments CE-SP-ICP-MS using REPSM with the possibility to detect a wider range of NPs of different composition may be used for commercial products and environmental samples analysis, laboratory studies, or production quality control. With the present improvements and further research, it would be possible to analyze samples with unknown NP content and composition to get species specific information on both the size and the concentration of NPs in complex mixtures.

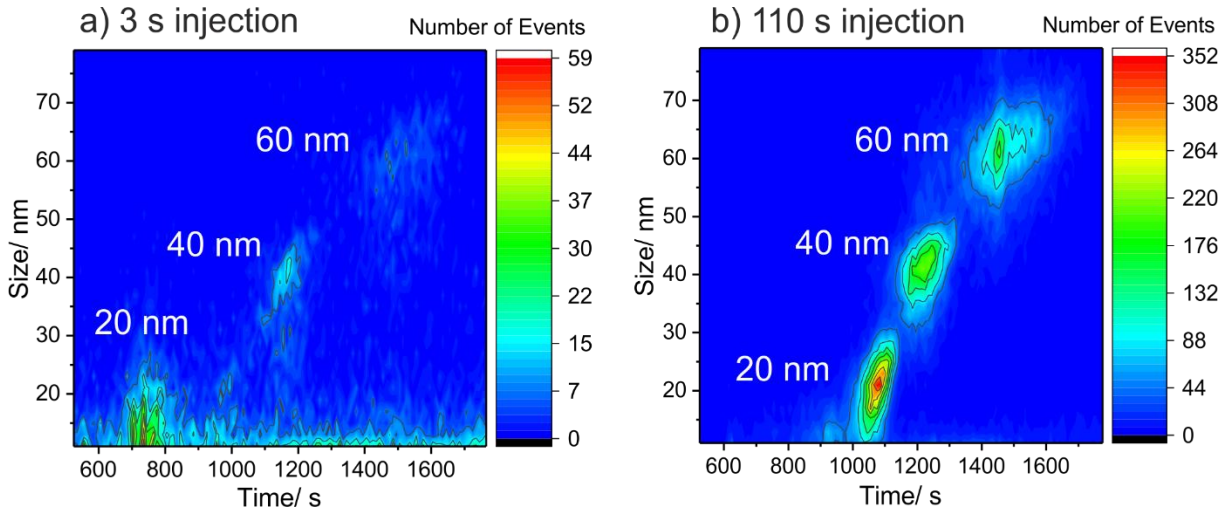

Figure 3.7: Two-dimensional color maps of CE-SP-ICP-MS analysis ($^{107}Ag^{+}$) of a mixture of 5 µg L^{-1} 20 nm sized, 35 µg L^{-1} 40 nm sized, and 200 µg L^{-1} 60 nm sized Ag NPs analyzed using 3 s injection without REPSM (A) and 110 s injection time in REPSM (B) at 20 kV (note that different color scales are used for (A) and (B); the BG in (A) is also present in (B), but not apparent due to the scale; time axis in (B) includes 110 s injection and 55 s REPSM preconcentration).

3.4 Conclusion

In this chapter, a nanoparticle characterization method based on REPSM online preconcentration, CE-SP-ICP-MS, and a prototype μsDAQ was developed and applied for the analysis of Ag NPs mixtures. Particle-by-particle information was obtained by continuously monitoring individual ion clouds from NPs that were introduced into the ICP with high time-resolution (5 μs, 100% duty cycle). SP-ICP-MS adds another dimension to CE separation, as NPs size information can be obtained for each of the >60,000 detected particles per CE run, and increases the resolution between NPs twice compared to CE-ICP-MS. After optimization of the preconcentration conditions, 110 s injection with REPSM and a CE separation at 20 kV were found to be the optimum for the present setup. With 110 s injection followed by REPSM it was possible to detect 14 ± 2 times more 20 nm sized, 21 ± 4 times more 40 nm sized, and 28 ± 5 times more 60 nm sized Ag NPs in comparison with 3 s injection. The capability of CE-SP-ICP-MS to do quantitative analysis was demonstrated, and linear calibration curves could be obtained with the detection limits in sub-microgram-per-liter-range. CE-SP-ICP-MS makes it possible to separate NPs by size and get information on NPs average size, size distribution, and PNC at any chosen time period during a CE separation. The data can be visualized with two-dimensional color maps, simplifying data evaluation and representation.

Chapter 4

Separation of Silver Nanoparticles with Different Coatings by CE-SP-ICP-MS

Based on:

D. Mozhayeva, C. Engelhard, Separation of Silver Nanoparticles with Different Coatings by Capillary Electrophoresis Coupled to ICP-MS in Single Particle Mode, *Anal. Chem.*, 2017, **89**, 9767-9774.

4.1 Introduction

According to the Derjaguin, Landau, Verwey, and Overbeek (DLVO) theory[267, 268] the stability of colloids is dependent on Van der Waals attraction and electrostatic repulsion between them. Therefore, the surface charge and the radius of the colloids along with the ionic strength of the suspension affect their stability. The surface coating of NPs typically consists of organic molecules or macromolecules that are bound to their surface either chemically or physically, and it determines the NPs reactivity in the surrounding medium. Surface coatings can increase the dimensions and the surface charge of NPs and, thus, enhance the NPs stability. Virtually all commercially available NPs, including certified reference materials (e.g., from the National Institute of Standards and Technology (NIST), Gaithersburg, MD, U.S.A.), and NPs suspensions (e.g., from nanoComposix, San Diego, CA, U.S.A.), are produced with surface coatings to ensure the stability of the NP size distribution over time. Once NPs enter the environment or a test medium, the surface coating may be partially or totally replaced by other organic molecules to form a complex particle corona. Also, varying pH values of a suspension may induce changes to the NPs surface charge. Consequently, aggregation or dissolution of NPs may occur when the coating is destabilized, and Van der Waals attraction between NPs prevails. Additionally, the kinetics of chemical or biochemical processes that include NPs may significantly change, affecting their bioavailability and environmental pathways. It is difficult to describe all of the processes that may happen to NPs in the environment or in living organisms, nevertheless, the processes governing the stability and aggregation of NPs in cell culture medium have been recently reviewed.[269] For quantum dots it was shown that the charge of NP surface coating affects their cytotoxicity, with the neutral NPs being less toxic for all tested NP sizes compared to the positively and negatively charged NPs, however, the cellular uptake of NPs was independent of the surface coating.[270] For these reasons, characterization of NPs only by chemical composition and size is not sufficient to determine their properties and environmental toxicity, hence, additional information on the composition of NPs surface coating and different NP species present in a mixture is required.

CE provides a unique separation mechanism, where the separation occurs not only due to the differences in NP size, but also due to the differences in NP surface charge. Electrophoretic mobility (μ) of a spherical particle in an electric field can be determined in the following way:

$$\boldsymbol{\mu = \frac{q}{6\pi\eta r}} \qquad \textbf{(Equation 4.1)}$$

where q is the net change of the NP, η is the viscosity of the surrounding medium, and r is the radius of the NP. Therefore, electrophoretic mobility of a spherical NP is directly proportional to its surface charge and inversely proportional to its radius or C/S:

$$\boldsymbol{\mu \propto \frac{q}{r}} \qquad \textbf{(Equation 4.2)}$$

Only few attempts were made in literature to differentiate NPs by their shape and surface charge. Huang et al. were able to separate quantum dots from their bovine serum albumin conjugates by CE.[271] Streptavidin (a protein) and biotin quantum dots conjugates were also separated in a mixture from each other.[272] Hanauer et al. successfully applied gel electrophoresis to separate Au and Ag NPs of different forms, additionally, it was shown that NPs with different surface coatings have different MTs.[273] Zhang et al. have shown that CdTe NPs with three different surface coatings (thyoglycolic acid, L-cysteine, and reduced glutathione) have different MTs when analyzed individually, however, they could not be separated from each other when injected in a mixture.[274] Later, cationic bifunctional maghemite/silica core/shell particles synthesized with different ratios of surface coating compounds (different surface charge) were separated in mixtures.[275] Li et al. were able to visualize the movement of Au NPs during a CE separation using dark field microscopy.[276] It was visually confirmed that the cetyltrimethylammonium bromide (CTAB) capped Au NPs with positive surface charge and the SDS capped Au NPs with negative surface charge have different velocities during the separation of the mixture. It was also recently confirmed that NPs with different coatings have different migration patterns in CE when injected individually.[277] To the best of author´s knowledge, the separation of NPs with

different coatings simultaneously present in a mixture still presents a challenge, and the separation of Ag NPs with different surface coatings has not been performed before by CE. Low variations in the C/S between Ag NPs with different surface coatings require a sensitive detection technique that will allow to achieve high resolution in the separation, compared to conventional CE detectors.

In comparison with the typical ICP-MS analysis, where analyte signals are typically constant over time, SP-ICP-MS can be used for sensitive NP detection with each NP detected individually as a short transient signal spike (atop the BG) with a definite intensity, if the sample is sufficiently diluted. The number of counts recorded per spike is later used to determine the size of a NP, because it is proportional to the NP mass. The advancements in fundamental studies and applications of SP-ICP-MS has been recently reviewed, showing that the technique is becoming a powerful tool to obtain NP average size, size distribution, and PNC.[8, 9]

Coupling of CE to SP-ICP-MS is associated with a challenge of assuring that only one NP is detected at a selected detection time window (basic principal of SP-ICP-MS), when NPs are focused during the separation in temporally short intervals.[18] A home-built data acquisition system with 5 μs time resolution allows to obtain the ion cloud profile of each NP that gets to the detector continuously over the course of a CE run.[11] Therefore, CE-SP-ICP-MS allows to add an additional NP size dimension to conventional CE separation and to increase the resolution between NPs during analysis. In addition, it was recently demonstrated that a combined approach of CE-SP-ICP-MS with online sample preconcentration helps to separate and quantify citrate-coated Ag NPs of different sizes in a mixture down to the sub-μg L^{-1} concentration range[18]. In the chapter, CE-SP-ICP-MS is used to investigate the behavior of more complex mixtures during CE separation, which contain Ag NPs with different surface coatings and sizes.

4.2 Experimental Section

4.2.1 Sample Preparation

Monodisperse spherical 20, 40, 60 nm sized citrate-coated; 20, 40, 60 nm sized PVP-coated; 40, 60 nm sized PEG-coated; and 40 nm sized branched polyethylenimine (BPEI)-coated Ag NPs were attained from nanoComposix (San Diego, CA, USA). Table A.1 represents the particle sizes obtained by TEM by the manufacturer. The suspensions were kept at 4 °C in darkness prior to analysis and shaken for 30 s prior dilution. The concentration of the NPs stock solutions was 0.020 g L^{-1}, desired dilutions were carried out with bi-distilled deionized water on the day of analysis. The CE separation buffer consisted of 60 mM SDS (99.5% pure for electrophoresis, Carl Roth, Karlsruhe, Germany), 10 mM CAPS (99%, Carl Roth, Karlsruhe, Germany), and 10 µg L^{-1} Cs (Inorganic Ventures, Christiansburg, VA, USA) at pH 10. The pH value of the buffer was regulated by addition of 1 M NaOH (98.8%, Th. Geyer, Renningen, Germany) and measured by a pH-meter (Multi 340i/SET, WTW, Weilheim in Oberbayern, Germany). The buffer and 1 M NaOH (used for capillary activation) were filtered with 0.45 µm polytetrafluoroethylene (PTFE) syringe filters (VWR International, Darmstadt, Germany). Buffers were prepared weekly and kept at 4 °C in darkness prior to analysis. Sheath liquid consisted of 10 µg L^{-1} indium (Inorganic Ventures, Christiansburg, VA, USA) and 2% HNO_3 (70%, analytical reagent grade, Fisher Scientific, Loughborough, UK).

4.2.2 Instrumentation

A model G7100A (Agilent Technologies, Waldbronn, Germany) CE system with polyimide-coated fused-silica capillary (75 (73.5 ± 0.7) µm i.d., 375 µm o.d., 70 cm long; Polymicro Technologies, Phoenix, AZ, USA) was coupled to a model ICAP Qc (Thermo Fisher Scientific, Bremen, Germany) ICP-MS quadrupole instrument. The coupling was performed by connecting the CE capillary outlet to the inlet of a model DS-5 microflow self-aspirating nebulizer (Teledyne CETAC Technologies, Omaha, NE, USA) via a 1.00 mm bore polyether ether ketone

(PEEK) crosspiece (Macherey-Nagel, Düren, Germany). The crosspiece serves to merge the CE flow with sheath liquid and to close the CE electrical circuit via an electrical cable from the outlet electrode attached to a stainless-steel wire in one of the outlets of the crosspiece. The contact of sheath liquid with the wire in the crosspiece ensures grounding. The CE instrument was controlled with Agilent OpenLab CDS (C.01.07, Agilent Technologies), and ICP-MS – with Qtegra ISDS software (2.4.1800.192, Thermo Fisher Scientific).

To achieve higher sensitivity for NPs detection, the ICP-MS was operated with a second roughing pump (Sogevac SV40 BI, Leybold Vacuum Cologne, Germany) in order to achieve lower interface pressure of 1.19 ± 0.02 mbar, and a high sensitivity skimmer insert (insert "2.8", Glass Expansion, Melbourne, Australia). The most important ICP-MS parameters are presented in Table 4.1.

Table 4.1: Main ICP-MS instrumental parameters.

Parameter	**Value**
RF power	1450 W
Ar cooling gas flow	14 L min^{-1}
Ar auxiliary gas flow	0.8 L min^{-1}
Ar nebulizer flow	0.8 L min^{-1}
Sampling position	3.5 mm
Torch injector inner diameter	1.5 mm
Dwell time	5 μs
Monitored isotope	$^{107}Ag^{+}$

Before the start of a first measurement of a day, capillaries were activated by rinsing them with 1 M NaOH, bi-distilled deionized water, and separation buffer for 10 min each. Before each run the capillary was flushed with the running buffer at 950 mbar for 1 min. The CE separation was performed at 20 kV with hydrodynamic injection at 50 mbar for 110 s followed by a REPSM preconcentration step, which was optimized specially for CE-SP-ICP-MS along

with the data acquisition and processing in the previous work.[18] In short, during REPSM -20 kV is applied to the capillary after initial sample injection. The current will then steadily increase up to a point where it reaches 90-95% of the typical value for the chosen conditions. Then, the polarity is switched, and +20 kV is applied to perform the sample separation. ICP-MS was operated in single particle mode and data was acquired with microsecond time resolution (5 µs) monitoring $^{107}Ag^{+}$ continuously for up to 40 min. Each analysis was repeated three times.

4.2.3 Data Processing

The data processing and graphical representation of results was done in Origin 2017 (OriginLab Corporation, Northampton, MA, USA). Size calibration was performed every day by measurements of individual 20, 40, and 60 nm sized citrate-coated Ag NPs suspensions with SP-ICP-MS, when the corresponding NP size was analyzed. External calibration for mixtures that contain different NP sizes was performed using a linear fit ($R^2 = 0.9997 \pm 0.0004$) with the size data provided by the manufacturer (Table A.1). The data was grouped to 2 nm × 10 s bins, and CE-SP-ICP-MS two-dimensional color maps diagrams with the CE MT on x-axis, the NP size determined with SP-ICP-MS on y-axis, and the color intensity representing the number of detected NPs per spot were obtained.

4.3 Results and Discussion

4.3.1 Theoretical Considerations on NPs Migration Order

The migration order in capillary zone electrophoresis is governed by the electrophoretic mobility of the charged analyte species and EOF. When a surfactant, in particular SDS, is added to the separation buffer at a concentration higher than the surfactants' critical micelle concentration, micelles are formed and act as a pseudostationary phase, and, in turn, the separation mode changes to MEKC. Analytes are then partitioning between the aqueous phase and the negatively charged micelles. In MEKC, the mechanism of analyte partitioning can be explained by ionic attraction between the analytes and the micelles, the degree

of analyte hydrophobicity, and hydrogen bonding.[278] As a result, MEKC can help to improve the resolution compared to standard CE conditions when a mixture of charged species shall be analyzed, and it also enables the separation of neutral analytes (given different interactions with the micelles). Due to the fact that the EOF prevails against the micelles partitioning mechanism (pH 10), positively charged analytes will have the lowest MT, followed by neutral and then negatively charged species. It is, therefore, theorized here that MEKC analysis of a mixture of NPs with similar sizes but different surface charges will result in the following migration order (at MEKC conditions described above): first, positively charged NPs (e.g., BPEI-coated) will reach the detector; second, NPs with relatively low negative surface charges will follow (e.g., PEG and PVP-coated) in the migration order. Lastly, NPs with a higher negative charge (e.g., citrate-coated) will reach the detector. If this type of migration order could be obtained in a mixture of NPs, then it would be a confirmation of the assumption that coatings/surface chemistry plays an important role and that differently coated NPs behave differently during the CE separation. The hypothesis was evaluated experimentally in this chapter and the results are discussed in detail below.

4.3.2 Separation of 20 nm Sized NPs with Different Coatings

A mixture of 20 nm sized citrate- and PVP-coated Ag NPs was analyzed by CE-SP-ICP-MS. It was found that both types of NPs migrated at the same time (1088±15 s, data not shown), which was similar to the MT of the individual NPs suspensions (PVP-coated NPs at 1085±10 s and citrate-coated NPs at 1062±12 s). The reason as to why a comigration was obtained is presumably the C/S. It is assumed that the difference in the C/S of the two 20 nm sized NPs species was too low to separate them from each other at the present conditions, because the initial concentrated individual NPs suspensions differed in zeta potential only by 6.4 mV and in average diameter only by 2.7 nm (Table A.1). Both types of NPs are negatively charged; thus, electrostatic attraction between them can be excluded.

4.3.3 Separation of 40 nm Sized NPs with Different Coatings

When a mixture of four types of 40 nm sized Ag NPs with different coatings was analyzed, the result was a relatively broad event in the electropherogram in CE-SP-ICP-MS (data not shown). The resolution of the technique was not sufficient to separate all four types of NPs in a single run. As a result, less complex two-component mixtures were analyzed. In Figure 4.1, CE-SP-ICP-MS analysis results are presented for all possible two-component combinations of 40 nm sized Ag NPs with BPEI, PEG, PVP, and citrate surface coatings, respectively. The composition of NPs in each separate two-dimensional color map can be found in the header of the corresponding columns/rows (note: when labels in a column and row are identical, the analysis result of a single type of NP material is presented). The MT of the one-component dispersions are presented in Table A.1, and of the two-component dispersions in Table A.2.

4.3.3.1 Single standard analyses.

When individual NPs suspensions were analyzed, it was found that the MT increased in the following order of coatings: BPEI-coated Ag NPs (peak maximum at 958±21 s, Figure 4.1A) and PEG-coated Ag NPs (peak maximum at 958±32 s, Figure 4.1E), PVP-coated Ag NPs (peak maximum at 1048±15 s, Figure 4.1H), and citrate-coated Ag NPs (peak maximum at 1275±115 s, Figure 4.1J). This experimental observation confirmed the theoretical considerations on NP migration proposed at the beginning of this sub-chapter (except for the MT of the BPEI-coated Ag NPs that was expected to be lower). Clearly, the nature of the surface coating affects the MT of NPs, and the migration profiles (Figure 4.1A, E, H, J) of different types of NPs differ from each other. The citrate-coated NPs have a skewed profile (Figure 4.1J), where the NPs with lower sizes migrate to the detector slightly faster than the NPs with relatively larger sizes (approximately 5 nm range). Interestingly, only citrate-coated NPs, which have the largest negative surface charge (Table A.1), were found to experience this sub-fractionation, whereas the peaks from other types of NPs did not feature a significant skewness. For example, migration profiles of BPEI-coated NPs

(Figure 4.1A) and PVP-coated NPs (Figure 4.1H) are symmetric in their CE profile. The PEG-coated NPs (Figure 4.1E) show a slight fronting.

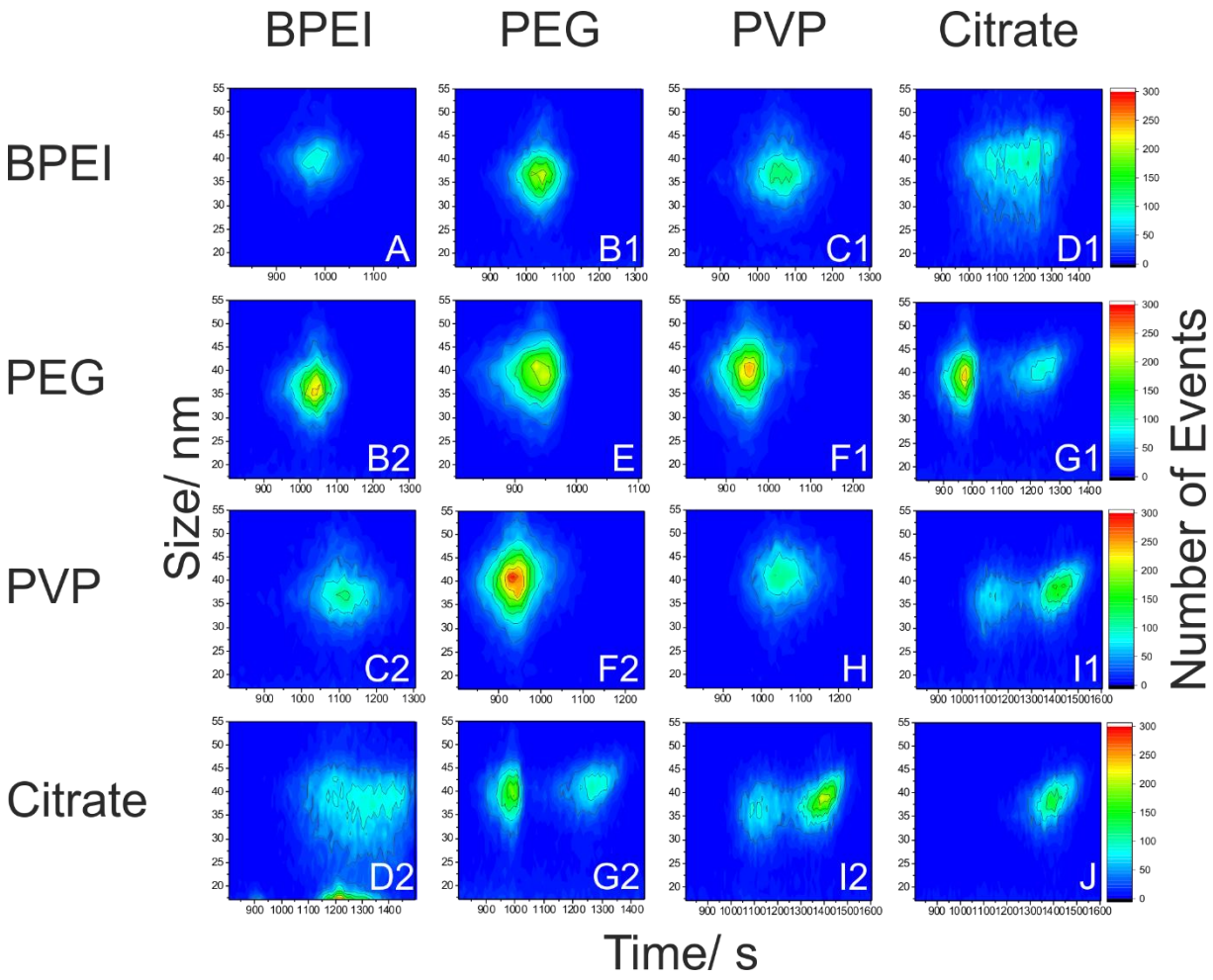

Figure 4.1: Separation of two-component mixtures and analysis of individual types of 40 nm sized Ag NPs with BPEI, PEG, PVP, and citrate surface coatings of 35 µg L^{-1} (approximately 1×10^8 particles per mL) each. Heat maps show the number of detected particles (monitored at $^{107}Ag^+$, 5 µs DT) at different MTs during a CE-SP-ICP-MS run. The composition of the mixture of different nanomaterials is given in the header of the columns/rows (First row, from left to right: BPEI only; mixture of BPEI and PEG; mixture of BPEI and PVP; etc.). Labels 1 and 2 represent repetitive measurements of the same mixture.

4.3.3.2 Two-component mixture analyses.

Compared to the single NP runs described above, it was found during the analyses of NP mixtures that the migration profiles do not necessarily stay the same but that they may change depending on the composition of the mixture. Also, the MT of NPs changed in many cases when NPs were injected in a mixture (Figure 4.1 and Table A.2). This phenomenon was reported also in the literature[279] and may be explained by the fact that NPs dimensions (1-100 nm) are only 750 to 75000 times smaller compared to the 75 µm capillary diameter; therefore, steric hindrance may be the reason of MT shifts.

The citrate-coated NPs were separated from two out of three types of NPs, namely, from the PEG-coated (Figure 4.1G) and PVP-coated ones (Figure 4.1I). During these separations, the individual profiles of these NPs did not change significantly. All of these three types of NPs are negatively charged (Table A.1); thus, when NPs of similar sizes in a mixture have a significant difference in surface charge, their separation should be feasible with CE-SP-ICP-MS (11 and 24 mV zeta potential difference between the initial (concentrated) NPs suspensions of citrate/PVP-coated NPs, and citrate/PEG-coated NPs, respectively). Separation of the negatively charged citrate-coated NPs from the positively charged BPEI-coated NPs (Figure 4.1D) was not successful, and it resulted in both broad MT and migration size profiles. This effect is not observed in all other separations and can be presumably attributed to the strong attraction between the NPs of opposite charges. As the SDS micelles are less than 4 nm in diameter,[280] they may be too small to separate NPs with at least 10 times higher diameter (excluding the size of the surface coating) that have attracted each other during the separation. It also should be noted that no increase in detected NPs size was observed. If the NPs formed aggregates, then a significant number of the NPs with sizes higher than 40 nm would have been detected. Instead, a significant number of NPs with sizes around 30 nm was detected, which is not the case for other mixtures containing the BPEI-coated NPs. The profiles of individual NPs ion clouds were reevaluated to confirm the absence of artifacts after the NPs ion clouds extraction algorithm. The partial decrease in NP size may confirm the hypothesis of specific interactions between the citrate- and BPEI-coated NPs during the separation. NPs may

partially dissolve already during the separation, and result in the detection of a high number of 30 nm sized or smaller NPs as well as elevated BG from ionic silver; however, future investigations would be needed to elucidate the process that is happening.

In general, it was not possible to separate the BPEI-coated NPs from any other negatively charged NPs (Figure 4.1B, C, D), and the PVP-coated from the PEG-coated NPs (Figure 4.1F). It is assumed that when both negatively and positively charged NPs are present in a sample, the interaction of the positively charged BPEI-coated NPs with the negatively charged NPs is preferable over the partitioning with the micelles. Both the PVP and PEG coatings are polymeric in nature, so the stability of this type of coatings is higher compared to the citrate-coated NPs. The partitioning of the negatively charged NPs with a stable surface coating with the micelles of the same charge is not favorable; consequently, the separation is only based on the C/S, which has similar values for both the PVP- and PEG-coated 40 nm sized NPs.

4.3.4 Separation of 60 nm Sized NPs with Different Coatings

In Figure 4.2, the result of a CE-SP-ICP-MS analysis of all possible combinations of two-component mixtures containing 60 nm sized Ag NPs with PEG, PVP, and citrate coatings is presented. The profiles of individual types of the 60 nm sized NPs (Figure 4.2) are similar to those obtained for the 40 nm sized NPs (Figure 4.1). PEG-coated NPs (Figure 4.2A) show a slight fronting and fast decline towards the end of the event. PVP-coated NPs (Figure 4.2D) have a rather concentric profile, while citrate-coated NPs (Figure 4.2F) feature a slightly skewed profile due to a size dependent separation. When PVP- and citrate-coated NPs are injected in a two-component mixture (Figure 4.2E), the separation is feasible; however, a baseline-resolved electropherogram could not be achieved. In order to obtain the same mobility as it was obtained for the 40 nm sized NPs, according to C/S separation principle in Equation 4.1 with the higher NP size the charge difference between NPs should be higher. In contrast to results with 40 nm sized NPs (Figure 4.1G), the mixture of PEG- and citrate-coated 60 nm sized NPs

(Figure 4.2C) was not resolved. This phenomenon could not be explained in the context of this chapter. In general, a lower resolving power could be obtained in the analysis of mixtures containing the 60 nm sized Ag NPs compared to the 40 nm sized NPs. Also, other tests were performed but data are not shown. For example, the separation of NPs with different negatively charged coatings in a mixture with three components was not successful but will be studied in more detail in the future.

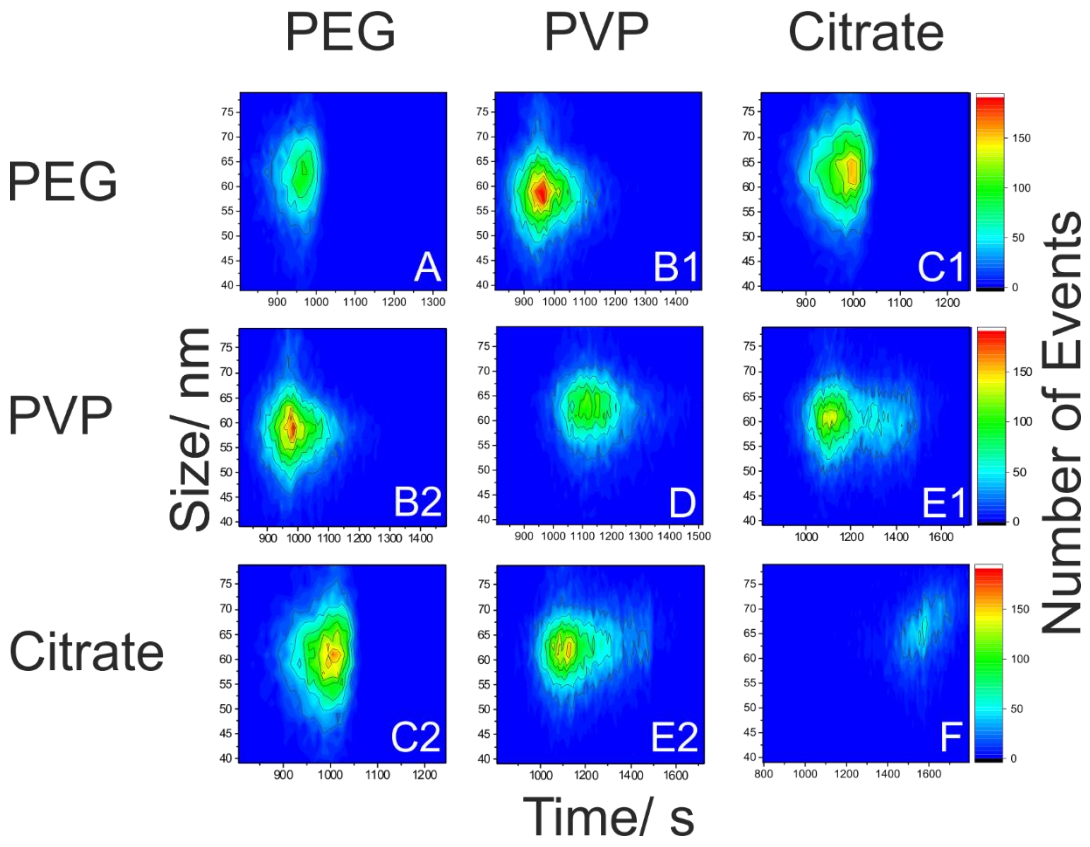

Figure 4.2: Separation of two-component mixtures and analysis of individual types of 60 nm sized NPs with PEG, PVP, and citrate surface coatings of 100 µg L^{-1} (approximately 8×10^7 particles per mL) each. Heat maps show the number of detected particles (monitored at $^{107}Ag^+$, 5 µs DT) at different MTs during a CE-SP-ICP-MS run. The composition of the mixture of different nanomaterials is given in the header of the columns/rows (First row: PEG only; mixture of PEG and PVP, etc.). Labels 1 and 2 (e.g. B1, B2) represent repetitive measurements of the same mixture.

4.3.5 Separation of Complex Mixtures with CE-SP-ICP-MS

The composition of environmental samples is usually unknown, and they may contain NPs with both different sizes and different coatings. Therefore, the separation and detection of NPs with CE coupled to conventional ultraviolet-visible spectroscopy or ICP-MS may be misleading, because NPs with different sizes and coatings may co-migrate. Here, the separation of NPs with different coatings in mixtures that contain also different sizes of NPs simultaneously was conducted to check the feasibility of CE-SP-ICP-MS to resolve more complex mixtures and to understand the separation principles of NPs in more detail. For this purpose, a mixture of selected NPs (coatings/sizes that could be resolved successfully, see above, namely, 20, 40, and 60 nm sized citrate-coated and 40 and 60 nm sized PVP-coated Ag NPs) was analyzed with both CE-ICP-MS and CE-SP-ICP-MS (Figure 4.3). Clearly, CE-ICP-MS provides only limited information (Figure 4.3A): only three peaks appear and without baseline-resolution. Further, no information is provided on the size of the NPs. With the added benefit of microsecond time resolution at the detector CE-SP-ICP-MS is capable of distinguishing all species in this five-component mixture (Figure 4.3B). Both the 40 and 60 nm sized PVP-coated NPs could be distinguished from the citrate-coated NPs of the same size, with the 60 nm sized PVP and citrate-coated NPs having much higher resolution, compared to a simpler two-component mixture (Figure 4.2E). This experimental result proves once again[279] that NPs have different MTs depending on a mixture, in which they are injected. For this reason, characterization of NPs only by their MT in CE-ICP-MS without SP-ICP-MS detection is not sufficient to be able to identify and characterize NPs, because, e.g., citrate- and PVP-coated NPs have different MTs, depending on the composition of a mixture that is analyzed.

CE-SP-ICP-MS results (Figure 4.3B) reveal a different behavior of the citrate-coated NPs versus PVP-coated NPs during separation. Both the 40 and 60 nm sized PVP-coated NPs elute from the capillary in the same time window and together with the 20 nm sized citrate-coated NPs. This is why only one peak could be detected with CE-ICP-MS (Figure 4.3A). More importantly, this peak could mistakenly be assigned only to 20 nm sized citrate-coated NPs, if no additional information on the sample mixture would be available. The polymeric PVP coating

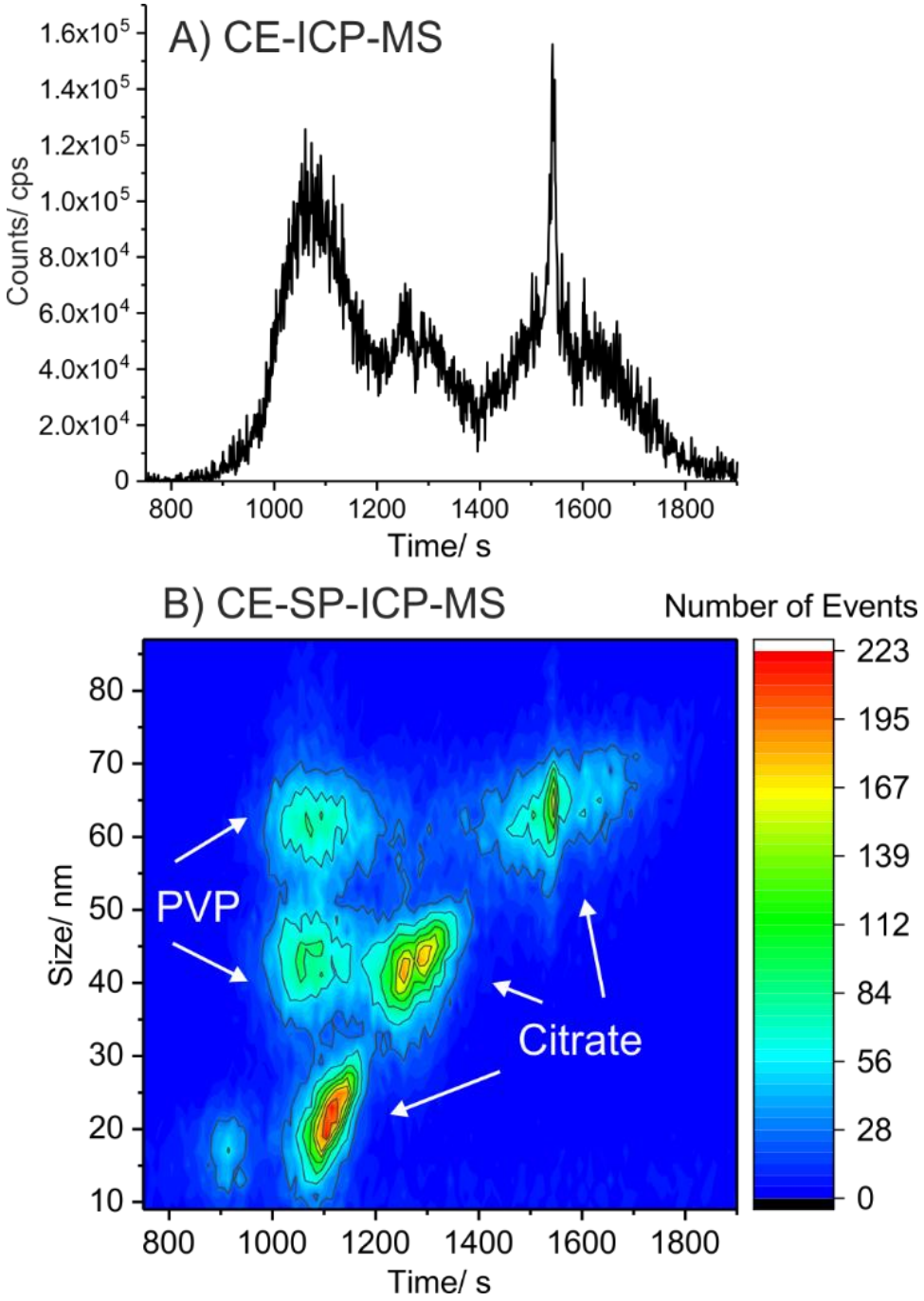

Figure 4.3: Comparison of a standard CE-ICP-MS plot (**A**) and first CE-SP-ICP-MS two-dimensional color map (**B**) acquired from a complex five-component mixture of different nanomaterials (5 µg L^{-1} citrate-coated 20 nm sized, 35 µg L^{-1} each citrate- and PVP-coated 40 nm sized, 100 µg L^{-1} PVP-coated 60 nm sized, and 200 µg L^{-1} citrate-coated 60 nm sized Ag NPs). The analysis was conducted by monitoring at $^{107}Ag^{+}$ with 5 µs DT, using 110 s injection and REPSM at 20 kV.

appears to be chemically stable in the micellar separation buffer, and the degree of interactions with the micelles is low, as a result no size separation could be obtained. This behavior may occur because negatively charged NPs do not partition with negatively charged micelles at pH 10, when negatively charged groups are above their pK_a, due to ionic repulsion. The resolution between these types of NPs cannot be increased with the use of SDS micelles, and the C/S mechanism seems not to be enough to obtain different MTs for the 40 and 60 nm sized PVP-coated Ag NPs because their coating is not substituted during the separation. Only CE-SP-ICP-MS with microsecond time resolution allows to obtain NP size information and to distinguish between the 20 nm sized citrate-coated and the 40 and 60 nm sized PVP-coated Ag NPs that comigrate in a narrow time window of approximately 200 s.

Attempts to understand the mechanism of NPs separation with the use of SDS in the buffer have been made before.[255] Liu and Wei[255] suggested that the coating is replaced while the hydrophobic tail of the SDS molecule would attach to the NP surface; however, the nature of this interaction was only explained by an increased adsorption of Au NPs to the C_{18}-modified silica gel. These results indicate that the separation mechanism may vary depending on the type of nanomaterial and coating. Specifically, it was observed that the separation mechanism of citrate-coated NPs is different from NPs that feature a polymeric PVP coating (see Figure 4.3B).

In the experiments, the larger citrate-coated NPs (60 nm sized) show a higher mobility towards the anode compared to smaller NPs (20 nm sized). Due to the strong EOF, the net flow of the NPs is directed towards the cathode; therefore, the 60 nm sized citrate-coated NPs have the longest MT (Figure 4.3B). Theoretically, according to the C/S separation principle, if the surface charges did not have high variation, the increasing NP radius would result in a lower NP mobility, which is not the case for the analyzed mixture. Therefore, a significant difference in the NPs charge is required in order for the 60 nm sized citrate-coated NPs to inhibit a higher mobility towards the anode compared to the 40 nm sized ones. However, the difference in zeta potential between the 40 nm and 60 nm sized NPs is relatively small (3 vs. 4 mV for PVP- and citrate-coated NPs, respectively;

measured in the initial concentrated NP suspensions, see Table A.1), and, in turn, the difference in surface charge between the two species is very likely to be small. These small differences are assumed not to be the predominate factor that is responsible for the experimentally observed particle size separation. Therefore, it is suggested that the separation of the citrate-coated NPs is not only occurring due to a C/S difference but also due to partitioning with the micelles. Because no electrostatic attraction between the negatively charged NPs and negatively charged micelles should occur, the following effect is assumed: The citrate coating is adsorbed to the metal surface in a form of dihydrogen citrate anions with the central carboxylate group attached to the metal surface. Hydrogen bonding exists between the terminal carboxylic acid groups and adjacent molecules.[281] As the citrate coating is labile and not polymeric, it may detach from the NPs surface, especially when being in direct contact with a surfactant. It was proven earlier that the addition of a negatively charged surfactant to negatively charged Ag NPs further decreases the zeta potential of the suspension.[282] Therefore, it can be expected that the sulfate groups of SDS can also adsorb to the Ag NPs surface as the carboxylate groups of citrate do. The adsorption of one layer of SDS would result in a net increase of the NPs hydrophobicity because the hydrophobic tales of the surfactant molecules would be oriented towards the surrounding medium. Thus, the hydrophobic tales of the first layer of SDS experiences hydrophobic interactions with the second layer of SDS. Labile citrate molecules are supposedly partially replaced during the CE separation by SDS molecules, which form bilayers on the NP surface and, in turn, enhance the negative charge on the surface. This phenomenon facilitates the size separation of the citrate-coated NPs and explains the experimentally observed migration order, because larger NPs have higher surface area for SDS adsorption; therefore, these NPs experience greater charge enhancement and longer MT.

4.4 Conclusion

CE-SP-ICP-MS was used for the first time to separate mixtures of silver nanomaterials with different coatings in the liquid phase. Different CE migration profiles and MTs for the NPs with different coatings were successfully obtained. It was found here that NPs with polymeric coatings migrate with their coatings attached to the NP surface and have relatively short MTs. NPs with a monomeric citrate coating may experience partitioning with SDS molecules and, in turn, can be separated with high size resolution but at longer MTs. On the basis of these results, it can be concluded that the characterization of NPs simply by their size is not sufficient and that the coating should also be considered, especially when NP standards are used for calibration of the CE-ICP-MS method. The NP size dimension that is provided by SP-ICP-MS (with microsecond time resolution) helps one to identify NPs size irrespective of the NP coating and MT because every NP event is recorded. It was found here that CE-SP-ICP-MS is able to distinguish every NP type in a five-component mixture of 20, 40, and 60 nm sized citrate-coated NPs and 40 and 60 nm sized PVP-coated NPs by resolving NPs with similar MTs due to the additional SP-ICP-MS NP size domain. Polymeric coatings are more chemically stable compared to citrate coatings and may therefore decrease the reactivity and transformation of NPs in the environment. It was demonstrated here that CE-SP-ICP-MS allows to distinguish between stable polymeric coatings (shorter MTs) and more reactive species with displaceable coatings (longer MTs). This feature of the method may provide more information about the state of NPs in the environment, help to better understand toxicity of various types of NPs, and provide a tool of extensive NPs characterization during or after their production.

Chapter 5

A Quantitative Nanoparticle Extraction Method for Microsecond Time Resolved SP-ICP-MS Data in the Presence of High Background

Based on:

D. Mozhayeva, C. Engelhard, A Quantitative Nanoparticle Extraction Method for Microsecond Time Resolved Single-Particle ICP-MS Data in the Presence of High Background,

J. Anal. At. Spectrom., 2019, DOI: 10.1039/c9ja00042a.

5.1 Introduction

The release of ionic silver from Ag NPs may cause the increased toxicity of this type of NPs.[283, 284] However, even though a significant amount of publications report on the mechanism of Ag NPs toxicity, they might use NPs with different sizes, surface coatings and exposure media, and in different organisms/cell cultures; thus, it is still not clear, to which degree toxicity stems from silver ions and NPs, respectively.[285] Advanced analytical methods are required to assess the presence and the quantity of different silver species, especially at environmentally relevant concentration. Centrifugal ultrafiltration and membrane filtration could be used for separation of Ag^+ from Ag NPs, however, the methods are limited by the membrane pore size, possible Ag^+ adsorption, and possible changes in the initial state of NPs.[286]

Techniques based on ICP-MS can be used to separate and directly analyse the NPs and dissolved metals. LC coupled to ICP-MS[237-239] and CE coupled to ICP-MS[18, 99, 257] both can be used for this type of separation, yet these methods still require an experienced operator. Ideally, in SP-ICP-MS NPs can be distinguished from the BG as pulses, if the BG is low. Frequently, this is not the case, and BG increase hinders the detection of NPs, because of increased SD of the BG; therefore, the L_D for NP size drastically deteriorates. Laborda et al. could detect Ag NPs from 40 to 80 nm (with DT of 5 ms) in the presence of the Ag^+ BG below 1 μg L^{-1}; however, the presence of already 300 ng L^{-1} of Ag^+ resulted in the increase of the calculated particle size L_D from 18 nm (in ultrapure water) to 32 nm (with 300 ng L^{-1} of Ag^+).[7] TiO_2 NPs could be distinguished from the continuous BG, where up to 0.5 μg L^{-1} of Ti (IV) was added.[287] Schwertfeger et al. introduced an approach for NPs and dissolved analyte quantification, where three dilutions were implemented for detection of gold and silver NPs in the presence of the dissolved ions.[94] First, the solution without any dilutions was measured to quantify the dissolved metal; afterwards, two dilutions were done for single NPs measurements. Without the dilution, it was shown that the presence of already 1 μg L^{-1} of dissolved silver lead to errors (size overestimation, lower number of particles detected) in the detection of 30 nm Ag NPs.

In conventional multi-elemental analysis with ICP-Q-MS a signal at a selected m/z is recorded for a certain DT (typically in the low to sub-millisecond range for NPs detection and up to 1 s during homogeneous samples analysis). As NPs result in relatively short ion signal events in the ICP-Q-MS (e.g. the ion signal duration for one 60 nm Ag NP was approximately 500 µs in the previous study)[18], the choice of an appropriate DT is crucial to assure a correct detection. The use of a DT on the microsecond time scale allows to acquire several data points per NP[11, 52, 61, 62, 65, 66, 77, 78, 81] and helps to avoid incorrect detection, when e.g. one NP event is splitted between two DT (split-particle event). An approach to use a 5 µs DT without a significant dead time (other than the SEM dead time) between consequent dwells was introduced by the group earlier.[11] When the µsDAQ is used, the counts that would otherwise be counted in e.g. 3 ms, are split into 600 dwells of 5 µs each; then, the counts detected per NP are summed up to get a signal reading per particle. This approach helps to minimize particle coincidence and split-particle events. Meanwhile, the BG is also split, and e.g. 100,000 cps of constant BG signal would theoretically correspond to only 0.5 counts in 5 µs; however, the counts that are recorded are positive integer numbers, so some of the readings would be 0 and others 1. This type of data should be described with a Poisson distribution, and not the Gaussian type. In this way, the low BG allows to extend the concentration range of dissolved metals, in the presence of which NPs can still be detected and quantified. The data obtained with the µsDAQ are later processed to extract NPs with an optimized algorithm. In the algorithm, a NP event starts when a count value exceeds a certain threshold, and ends, when a second but lower threshold is reached.[11] However, there is a challenge: a high BG (e.g. 100,000 cps) can adversely influence the total counts per extracted NP ion cloud because the BG is extracted together with the NPs and the extraction conditions (thresholds) have to be carefully selected. In addition, the ICP-MS user has to decide, which signal should still be counted as a signal from a NP and which signal should be counted as BG fluctuation when working at the low count level (a single 20 nm Ag NP can result in a signal of approximately 30 counts with an optimized ICP-Q-MS). Additionally, a new L_D definition is required to tackle this

issue based on Poisson and not solely on normal statistics, and the approach is presented in detail further below.

Typically, researchers use the three times the SD of the BG ($3\times SD_{BG}$) based on normal distribution of the data to differentiate NP signal distributions from the BG when ICP-MS data is obtained with millisecond time resolution.[9, 10, 89] Cornelis and Hassellöv reported a deconvolution approach to differentiate the NPs that are not fully separated from the BG by modelling the noise contribution in ICP-Q-MS.[91] Recently, Gundlach-Graham et al. used a Monte Carlo simulation approach to obtain the signal distribution of the noise and low-count signals in ICP-TOF-MS data at a mass spectral acquisition rate of 200 Hz. In their study, thresholds for the detection of NPs were determined using Poisson statistics.[288] Beginning in 2014, ICP-Q-MS instruments became commercially available that feature DT settings down into the hundred-microsecond regime and up to 25 µs DT. However, a standardized data processing approach for microsecond-time resolved data in ICP-Q-MS is not established so far. Data processing is also limited by the software of current ICP-MS instruments, where only a few million data points can be recorded and/or processed per measurement, causing a limitation in the available total analysis time. Researches are still evaluating different types of data processing and the possibilities that a higher time resolution might provide. For example, with 100 µs microsecond time resolution, the NPs were separated from BG signal by applying the $3\times SD_{BG}$ criterion.[52, 289] M. D. Montaño et al. [81] used 25, 50, and 100 µs DTs to distinguish a $^{28}Si^{+}$ signal from a high $[^{14}N^{14}N]^{+}$ BG during silica colloids analysis. In their study, an iterative algorithm with an initial threshold according to the $3\times SD_{BG}$ criterion, subsequent smoothing, and BG subtraction was used. An algorithm based on outlier detection was presented by J. Tuoriniemi et al. for data with 100 µs time resolution.[62] A different approach reported by Donard et al. utilizes the detection of peak maxima.[61, 66]

In the present chapter, a data processing method based on Poisson statistics for simultaneous quantification of NPs and dissolved ions (recorded with a prototype µsDAQ) is reported. The method is rapid and can be used to process ICP-MS measurements of any duration. Ag NPs are selected as a model sample because they are widely discussed in the literature on SP-ICP-MS. A general algorithm for

analysis of NPs and dissolved ions is developed that is not limited to silver ions and NPs, but can also be used for ions and NPs with different elemental composition. Throughout the discussion below, the term "NP size" refers to the calculated NP size, if not stated otherwise.

5.2 Experimental Section

5.2.1 Sample Preparation

Monodisperse spherical Ag NPs with nominal diameters of 20, 40, 60, and 100 nm with citrate coating and an initial concentration of 0.020 g L^{-1} were bought from nanoComposix (San Diego, CA, USA). The diameters of the NPs determined by TEM by the manufacturer were 18.5 ± 3.4, 39 ± 4, 62 ± 7, and 98 ± 10 nm, respectively. The suspensions were preserved at 4 °C in darkness before analyses and manually shaken for 30 s prior dilution. No data was provided from the manufacturer on the content of silver ions in the suspensions. Dilutions were done with bi-distilled deionized water directly prior the analyses to achieve the PNC of approximately 2.5×10^5 NP mL^{-1}. Ag^+ solution (999 ± 5 mg L^{-1}, Inorganic Ventures, Christiansburg, VA, USA) was diluted for external calibration and added to NPs suspensions with nine different concentrations from 10 ng L^{-1} to 7.5 µg L^{-1} (with experimental dilution uncertainty). $NaNO_3$ (≥99%, analytical reagent grade, Carl Roth GmbH, Karlsruhe, Germany) and HNO_3 (70%, analytical reagent grade, Fisher Scientific, Loughborough, UK) were used for the matrix modification of bi-distilled water.

5.2.2 Instrumentation

All measurements were done on a model ICAP Qc (Thermo Fisher Scientific, Bremen, Germany) ICP-Q-MS instrument. The instrument was controlled by Qtegra ISDS software (2.4.1800.192, Thermo Fisher Scientific). The ICP-Q-MS was equipped with a model ESI SC-2 DX autosampler (ESI Elemental Service & Instruments GmbH, Mainz, Germany), a model MicroFlow PFA-50 nebulizer (Thermo Fisher Scientific, Bremen, Germany) with self-aspiration flow rate of

around 65 µL min^{-1} at 1 L min^{-1} Ar (manufacturers data), and a Peltier-cooled cyclonic quartz spray chamber held at 3 °C. A second roughing pump (Sogevac SV40 BI, Leybold Vacuum Cologne, Germany) allowed to achieve a lower interface pressure of 1.36 ± 0.02 mbar, and together with a high sensitivity skimmer insert (insert "2.8", Glass Expansion, Melbourne, Australia) and nickel cones helped to increase the sensitivity of the instrument. The main instrumental parameters of the ICP-MS are presented in Table 5.1.

Table 5.1: ICP-MS instrumental parameters.

Parameter	**Value**
RF power	1450 W
Ar cooling gas flow	14 L min^{-1}
Ar auxiliary gas flow	0.8 L min^{-1}
Ar nebulizer flow	0.6 L min^{-1}
Sampling position	2 mm
Skimmer type	Ni (insert version)
Insert type	Skimmer cone insert "2.8"
Torch injector inner diameter	1 mm
Dwell time for µsDAQ	5 µs
Dwell time for vendor software	10 ms
Monitored isotope	$^{107}Ag^{+}$

5.2.3 Data Acquisition and Data Processing

The µsDAQ (5 µs DT) was operated simultaneously with the vendor software (10 ms DT). All NPs suspensions were analysed for 3 min in triplicates, and the dissolved ionic standard calibration was performed once per day by measuring each calibration standard for 1 min. After each measurement the probe was washed in 2% HNO_3 for 45 s to ensure no carry-over between the samples. To guarantee the continuous detection with the µsDAQ, the detection was performed only in the counting mode of the SEM. The maximum concentration of Ag^{+} was

chosen to be 7.5 µg L^{-1} resulting in approximately 10^6 cps, which does not lead to detector saturation. The graphical representation of results was done in Origin 2017 (OriginLab Corporation, Northampton, MA, USA).

5.2.3.1 Millisecond Time Resolution

The data obtained with the 10 ms DT from the Ag NPs suspensions with and without additions of the Ag^+ and from the calibration standards were binned to obtain signal distribution diagrams. Gaussian fitting was used both for NPs and for the continuous BG fitting. The maximum of Gaussian distribution was taken as an average counts value. Also, the width of the distribution ("W") parameter that equals to two SDs was used in the calculations.

5.2.3.2 µsDAQ Data Processing

With the 5 µs time resolution, 200,000 data points are generated per second, and several data points are obtained per NP; therefore, to reduce the number of data points, extract the NP ion clouds events from the BG, and reduce the size of the data file; the ion clouds extraction is needed. As there are only e.g. 5000 NPs distributed more or less homogeneously over a 180 s ICP-MS measurement (3.6×10^7 data points), the majority of the data collected is the BG. As it was described earlier[11], the ion cloud extraction was done with a command line tool written in "C". The basis of the ion cloud extraction mechanism is to set three parameters; namely, "S" (how many data points should be grouped and summed up to judge, if the chosen threshold conditions are reached), "T" (a threshold value; when it is reached, an ion cloud extraction begins), "E" (an end threshold; when it is reached, the ion cloud extraction ends). Only positive integer numbers were used as thresholds, since the output of the detector (acquired data) contain only positive integer numbers. The counts obtained per particle are summed up; and the output contains time stamps of the ion cloud beginning and end, duration of each ion cloud, the number of counts per ion cloud, along with the time-resolved profiles of the extracted ion clouds. To reduce the number of variables in the current study, S = 5 was used in all of the tested extraction conditions combinations. Specific examples are described below. In order to test different sets of extraction

parameters, another command line tool was used to process file batches with different extraction conditions.

Different ion clouds extraction conditions were tested only on one data set out of the three replicates, because the number of NPs per 3 min run was always higher than 3500 for 40, 60, and 100 nm NPs. The number of detected NPs was considered to be sufficient to construct a size distribution with statistical significance (also because the determination of PNC was not the goal of the chapter). External size calibration was made daily with 20, 40, 60, and 100 nm Ag NPs without addition of dissolved silver. To have a starting point for the investigation of the influence of the extraction conditions on the calculated NP size the external size calibration has been performed with S = 5, T = 5, and E = 1 extraction conditions (when 5 counts (T = 5) were detected in 25 µs (S = 5) an ion cloud starts; and when there was only 1 count (E = 1) in 25 µs, the ion cloud ends). These values were calculated using the formulas from Table 5.2, when average BG is low (see Table 5.3 and further sections for details). The BG was subtracted, and the linear fit resulted in $R^2 = 0.996 \pm 0.002$ based on the sizes provided by the manufacturer. High correlation coefficient is an evidence of the stability of the NP in the suspensions. After size calibration and BG subtraction, the size distribution diagrams were constructed by binning the data into 2 nm bins. Fitting of all obtained size distributions was performed with a Gaussian model. This allows to easily compare the maxima of the distributions, which is not always straightforward with other fitting models (e.g. Poisson distribution). In this chapter, different criteria including BG maximum, mean NP size, width of the size distribution, total number of detected NPs, and size starting from which the NP size distribution can be distinguished obtained from the constructed size distributions were used to compare different extraction conditions (see Chapter A. 1 and Figure A.3).

5.3 Results and Discussion

5.3.1 Quantification of Ionic Silver in the Presence of NPs with Millisecond Time Resolution

The goal of this chapter is to develop a method that is capable to determine both the concentration of dissolved metal and NP size. First, the possibility to quantify ionic silver in the presence of NPs was evaluated. Quantification of Ag^+ in solution was performed with ICP-Q-MS and 10 ms DT. L_D ($3.29 \times SD_{BG}$) calculated from ionic standards analysis was 16 ± 2 ng L^{-1}, and the limit of quantification (L_Q) ($10 \times SD_{BG}$) was 47 ± 6 ng L^{-1}. The data obtained with the µsDAQ could also be used for quantification of the BG signal; however, the data processing would take a lot of time. Each 3 min measurement results in 3.6×10^7 data points, and this amount of data points could not be visualized with the software available to us nowadays (limited to only a few millions data points). Thus, data with millisecond time resolution was used to determine the BGs throughout this chapter. The BGs obtained with 10 ms DT in counts per second were recalculated to average BGs in 5 and 25 µs in order to be used in the further data evaluation. Computers with more computational power and software able to handle more input data will make the extraction of the average BG from the microsecond time resolution data much faster in the future.

5.3.2 Matrix Effects in the Plasma

In order to verify that the BG obtained in the presence of NPs corresponds to the concentration of Ag^+ in the suspension, the mean BG signal obtained with 10 ms DT for Ag^+ in the presence of Ag NPs of different diameters was compared with the mean BG signal obtained from Ag^+ calibration solutions at different concentrations (Figure 5.1). The mean BG signal was found to be typically higher in the presence of NPs compared to the mean BG signal from a neat Ag^+ calibration solution (up to 1 µg L^{-1}) (Figure 5.1A). Among the different NPs under investigation, larger particles (60 nm, 100 nm) had a greater effect and resulted in

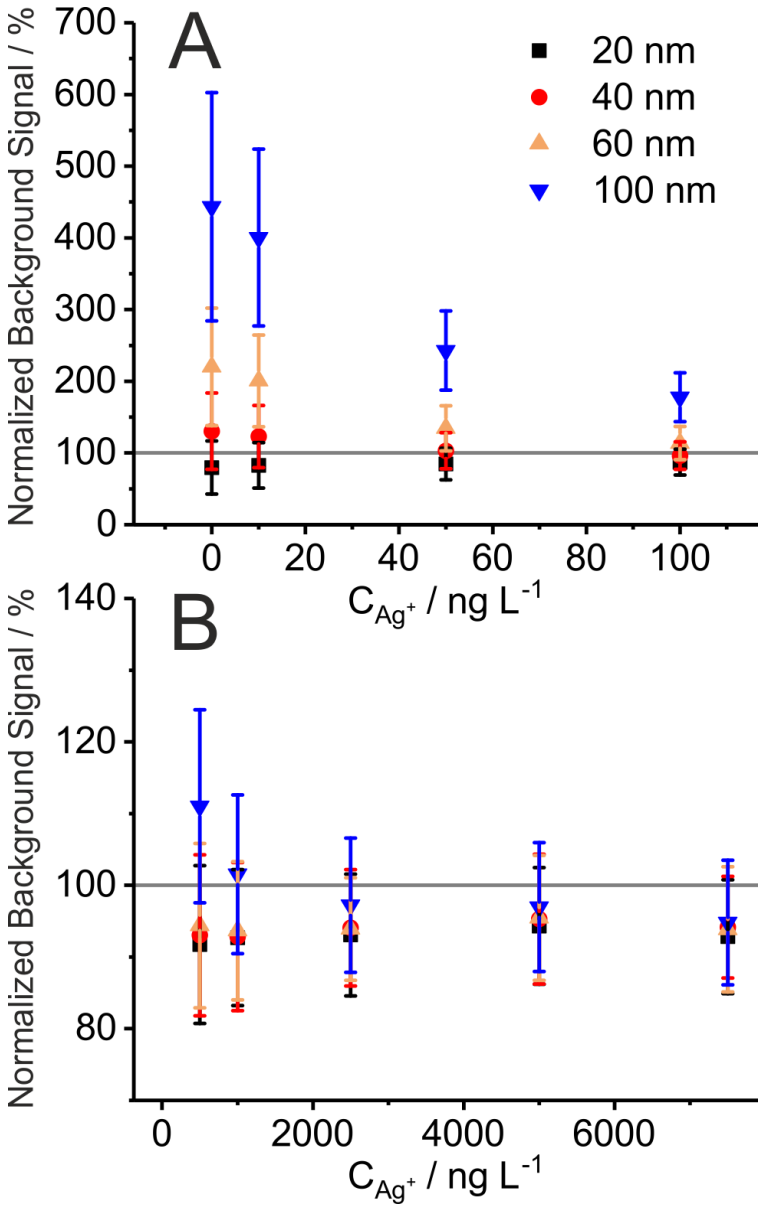

Figure 5.1: Mean background (BG) signal (recorded with ICP-Q-MS at $^{107}Ag^+$, 10 ms DT) in the 20, 40, 60, 100 nm Ag NPs suspensions (n = 3, different sample measurements on three different days) after the additions of Ag^+ from 0 ng L^{-1} to 100 ng L^{-1} (A) and from 500 ng L^{-1} to 7.5 µg L^{-1} (B) relative to the mean BG signal of Ag^+ calibration solutions without NPs. "Normalized background signal" represents ratio of the mean BG signal, when Ag^+ was added to the NPs suspension at different concentrations divided by the mean BG signal of Ag^+ calibration solutions of the same concentration but without NPs, in percent. A value of 100% would indicate that the BG counts obtained with and without NPs in solutions are equal.

a larger ionic mean BG signal increase, compared to the NPs of smaller diameter (20 nm, 40 nm). One explanation is that the former suspensions already may have contained elevated levels of Ag^+ (Figure 1A at 0 ng L^{-1} of Ag^+). Therefore, the fraction of the Ag^+ in the Ag NPs suspensions is significant and results in the elevated BG, especially when low concentrations of Ag^+ (10 – 500 µg L^{-1}) are added. The mean BG signal slightly decreases (94.6 ± 1.4%) when NP are present in the samples compared to solutions only with ionic silver (100%, cf. Figure 5.1B; trend notable starting at >1 µg L^{-1} Ag^+). The same effects were observed in this chapter for PVP-coated NPs (data not shown here). The depletion of the signal may be a potential indication of matrix effects in the plasma, according to the following studies. As Chan and Hieftje[47] have recently demonstrated, droplets in the plasma cause local plasma cooling during evaporation followed by the reheating of the plasma to even higher temperature in a time period of a few milliseconds (the effect is slower than the typical ion cloud duration of a NP, which is on the order of few hundreds microseconds). Accordingly, it is assumed that NPs result in a similar local plasma cooling and reheating, which then shortly thereafter may influence the ionization efficiency of ionic species. Another experimental proof for the effects of NPs on fundamental plasma parameters was presented by Murtazin et al.[43] In their study, the position of atomization and ionization of calcium in the ICP was delayed relative to the increasing diameter of SiO_2 particles (from 0.83 to 1.55 µm), which were added to the aspirated sample. Both studies are certainly relevant for SP-ICP-MS studies and one should be aware of potential matrix effects during the analysis of dissolved species in the presence of nanoparticles (and vice versa) and a potential shift of the ideal sampling position in ICP-MS. In this study, a signal drop for silver ions BG (>1 µg L^{-1} of Ag^+ added) of approximately 5% (as discussed above) is observed when NPs were present, compared to the solution without NPs. Please note that different NPs (20, 40, 60, 100 nm) did not significantly change the degree of signal depletion; and according to Figure 5.1B, 100% signal is in the range of one SD of the mean BG from triplicate analysis. In addition, it should be noted here that the counting stage of the SEM has a limited linear dynamic range. The upper level of the linear dynamic range can be limited due to pulse pile-up at high count rates because of large amounts of incoming ions (especially relevant for

larger Ag NPs). In the current work, an ionic silver concentration, and, thus, average BG signal was used below the saturation level of the used SEM. A future study on potential NP matrix effects in SP-ICP-MS with microsecond time resolution and a study on how to expand the upper level of the linear dynamic range in SP-ICP-MS is planned to further understand these observations in more detail.

5.3.3 Background Correction for NP Signals Recorded with Microsecond Time Resolution (µsDAQ)

As the total signal of an ion cloud is the sum of the extracted counts, it is important to compensate for any BG influence to achieve a more precise sizing. To avoid an artificial NP size increase, a BG subtraction mechanism is proposed, where the BG is subtracted mathematically from each extracted ion cloud, taking into the account the specific durations of each ion cloud with the following formula:

$$S_{cor,i} = S_i - D_i \cdot BG_{5\,\mu s} \qquad \textbf{(Equation 5.1)}$$

where $S_{cor,i}$ is the corrected signal of an ion cloud, S_i is the non-corrected signal of an ion cloud, D_i is the duration of the ion cloud in number of extracted data points with 5 µs time resolution, and $BG_{5\,\mu s}$ is the BG per 5 µs. In this chapter, this BG value was recalculated from the BG obtained with the vendor software for the same measurement. The BG correction was implemented to all data used in this chapter.

After data processing with the BG subtraction (Equation 5.1), the BG corrected Ag NP sizes in the presence of ionic silver were found to be in a better agreement with Ag NP reference values (sizes obtained from suspensions without an addition of ionic silver). In fact, the NPs sizes were gradually decreasing with the increasing Ag^+ concentration, with around a 4 nm size decrease for 40, 60, and 100 nm Ag NPs after the addition of 7.5 µg L^{-1} of Ag^+. As $^{107}Ag^+$ is detected in ICP-MS, Ag^+ and Ag NPs are not differentiated from each other; therefore, the slight decrease in the calculated NPs size may occur due to partial suppression of the BG, when NPs are detected; or due to a lower number of counts detected per NP, when the BG is present. As it was discussed in the previous section, the simultaneous

presence of Ag NPs and Ag^+ may cause matrix effects in plasma due to changes in plasma characteristics, it is also confirmed by the fact that the average BG obtained with the vendor software decreased 5.4 ± 1.4% compared to the values obtained for calibration solutions (after 1 µg L^{-1} of the added Ag^+) (Figure 5.1B). The NPs sizes obtained with different ion cloud extraction conditions were not compensated for the discovered NP size decrease, as the mentioned matrix effects require more investigations (in a future study).

5.3.4 Limits for Qualitative NPs Ion Cloud Extraction for the µsDAQ

Usually $3\times SD_{BG}$ is used as L_D in SP-ICP-MS.[89] Because a time resolution of 5 µs is now feasible in SP-ICP-MS, the concept of L_D for NPs should be revisited as well. Early papers on the detection limit were published by Kaiser in 1947[290] and Currie in 1968.[291] In the paper by Currie, the detection limit formula was derived for normal distribution and for Poisson distribution under an assumption of a normal distribution. In the mathematical transformations, both errors of the first kind (α, detecting false positives) and the second kind (ß, failing to detect the substance when it is present) were set to 5%. Another parameter that was introduced was the critical level (L_C), upon which a substance may be considered detected. Here, only a value for α of 5% was used ($L_C<L_D$) assuming that risks of 5% are acceptable and random errors are normally-distributed.[290]

In contrast to conventional SP-ICP-MS operation, which provides only one count value per particle event at 1-10 ms DT, data from the µsDAQ is comprised of a time-resolved profile of counts, where the sum of counts gives the total NP signal. Therefore, it is proposed that the L_D can represent a value, above which an ion cloud profile can be detected on top of BG fluctuations. As it was not feasible in the current study to get an average BG from 5 µs resolved data due to a high number of data points and limitations in the software, the BG was obtained from data acquired with 10 ms DT and then recalculated (discussed above) to match shorter DTs. After a recalculation to 25 µs (S = 5), the BG is typically only between fractions of a count and 32 counts. In this case, a normal distribution, which was assumed for the conventional L_D formula derivation, does not apply anymore, and

a Poisson distribution can be used instead.[291] Three main criteria determine the Poisson distribution:

1. The values are positive integer numbers, which is the case for the μsDAQ.
2. If a time interval tends to zero, then also the probability to get a count tends to zero; which is also true for the NPs detection, as the detection occurs at discrete time intervals.
3. A value x_n does not depend on the next value x_{n+1}. In order to achieve this condition, there should be only one data point detected per NP, which is not the case for the μsDAQ. When a NP begins, then the next count will be dependent on the previous one.

In order to determine the L_D for an ion cloud, the ion cloud extraction process should be considered. To fulfil all three criteria of the Poisson distribution, especially the third criterion, only the beginning of an ion cloud can be considered, namely the T threshold value (an ion cloud starts, when the value is reached), so the decision for the detection of an ion cloud would depend only on the rising edge of the ion cloud count profile. Consequently, the L_D calculation for the low number of counts in Poisson distribution has to be found. As in the ion cloud extraction process one of the conditions is that T>E (when T = E, the algorithm would go to a loop), it is proposed to use L_C to determine the end of an ion cloud. Thus, the T parameter should be above L_D ($\alpha \leq 5\%$, $ß \leq 5\%$), and the E parameter should be equal to L_C ($\alpha \leq 5\%$). Cases of low number of counts are often found in radiochemistry; and Currie[291] treated Poisson distribution under an assumption of normal distribution, "if the number of counts are sufficiently large". The L_D formulas for the Poisson distribution (with the assumption of normal distribution) were determined for two cases: paired observations and well-known blank (where the deviations of the BG are neglected).[291] Later, the paper was extended[292] in order to address the issue of "very low-level counting data" below 5 counts. The initial paper and a more recent summary[293] present a table based on the calculations using cumulative exact Poisson distribution (without Gaussian approximation), a well-known blank; and $\alpha \leq 5\%$, $ß \leq 5\%$ for L_D ($\alpha \leq 5\%$ for L_C). Formulas and example calculations for exact Poisson distribution to determine L_D and L_C are presented in the Chapter A. 2 and

Table A.3. It should be noted that for Poisson distribution, L_Q should be above 100 counts; therefore, this parameter was not considered in the calculations.

Table 5.2: Formulas for L_C and L_D[291] for NP ion clouds extraction.

	L_C (limit to identify the end of an ion cloud)	L_D (limit to identify the beginning of an ion cloud)
Paired observations ($\mu_B < 5$)	$2.33\sqrt{\mu_B}$	$2.71 + 4.65\sqrt{\mu_B}$
"Well-known" BG ($\mu_B > 5$)	$1.64\sqrt{\mu_B}$	$2.71 + 3.29\sqrt{\mu_B}$

The paired observations case takes into the account the deviation of BG, resulting in higher values compared to the case with "well-known" BG values. The "well-known" BG represents the case, where the deviations of the BG are neglected.

For a user friendly calculation of L_D and L_C, it is proposed to use the formulas that are presented in Table 5.2 (Poisson distribution with the normal distribution approximation). The values obtained from the cumulative exact Poisson distributions were compared (Table 5.3) with the values obtained for the Poisson distribution with normality approximation, where only an average BG (μ_B) is sufficient to conduct the calculations (Table 5.2).[291] In the paired observations formula, the deviation of BG is taken into account, resulting in higher values compared to the case with "well-known" BG values. After the comparison of the values (Table 5.3), the paired observations formula (Table 5.2) can be used as an approximation for the BG below 5 counts, and the "well-known" blank formula can be used for the BG above 5 counts. According to this approximation, the difference between the values obtained with the cumulative Poisson distribution and the normality approximated values was below 1 count (only two values of L_D differed less than 2 counts, with the higher values obtained for the normality approximation). In practice, false positives and false negatives can still be separated from the NPs events, since the size distribution diagram is constructed,

and the remaining BG can still be distinguished from the NPs by the $3.29 \times SD_{BG}$ criterion.

Table 5.3: Comparison between y_C and y_D obtained with Poisson distribution under different approximations for 20 nm Ag NPs spiked with Ag^+.*

C_{Ag^+} / ng L^{-1}	μ_B / counts in 25 µs (S = 5)	SD / counts in 25 µs (S = 5)	Poisson distribution[292, 293]		Paired observations[291]		"Well-known" BG[291]	
			y_C	y_D	y_C	y_D	y_C	y_D
0	0.09	0.02	1	4.74	0.77	4.16	0.57	3.76
10	0.12	0.02	1	4.74	0.92	4.44	0.69	3.97
50	0.28	0.03	1	4.74	1.51	5.45	1.15	4.73
100	0.48	0.04	2	6.30	2.10	6.42	1.62	5.48
500	2.1	0.1	5	10.51	5.51	11.59	4.50	9.61
1000	4.2	0.2	8	14.44	8.91	16.35	7.50	13.57
2500	9.9	0.4	15	23.10	17.24	27.26	15.07	22.98
5000	19.9	0.7	28	38.38	30.35	43.42	27.27	37.35
7500	30	1	39	50.94	42.37	57.72	38.61	50.31

*The first set of y_C and y_D was calculated for exact Poisson distribution with "well known" BG (Table A.3), further sets were calculated with an assumption of normality for Poisson distribution according to Table 5.2. L_C and L_D are obtained from y_C and y_D, correspondingly, by subtraction of μ_B.

In order to get the ion clouds extraction parameters E and T, μ_B should be added to the obtained L_C and L_D to obtain the corresponding gross counts (y_C and y_D). It should be noted that only positive integer numbers are used in the ion clouds extraction, since only integer counts are detected; thus, the obtained non-integers can be rounded to the closest integer number to obtain the suitable ion clouds

extraction conditions. In the next section, the hypothesis of using L_C and L_D for NP ion clouds extraction will be tested in detail.

5.3.5 Optimization of the Ion Cloud Extraction Conditions

Different ion cloud extraction conditions below and above L_C and L_D were chosen to study their effect on the obtained NP size distributions. It is noted here that 20 nm sized Ag NPs could only be partially separated from the BG in the count histogram. The size L_D was at least 16 nm (S = 5, T = 5, E = 1) (Table A.4); therefore, 20 nm Ag NPs do not follow the same trends that were observed with 40, 60, and 100 nm sized Ag NPs (discussed below). All other tested NPs size distributions could be separated from the BG even in the presence of ionic silver up to 1,000,000 cps, which is a significant improvement compared to the data obtained with 10 ms DT due to the high time resolution in SP-ICP-MS.

Figure 5.2 and Figure A.4 represent average calculated NPs sizes (Label B in Figure A.3) obtained with different extraction conditions without an addition of dissolved silver (Figure 5.2) and with the addition of 7.5 µg L^{-1} of Ag^+ (Figure A.4). In general, the main trends are very similar, and the obtained sizes are more or less independent of the T parameter and change depending on the E parameter. Lower E results in higher sizes, since more counts are added in the end of ion clouds; and higher E results in lower sizes. No specific trends were found for the changes in the width of the NP size distributions (Label C in Figure A.3) with varying extraction conditions. The obtained NPs sizes do not change to a large degree with the varied extraction conditions: maximum deviation up to 4.7 nm for 40 nm, up to 2.1 nm for 60 nm, and up to 1.0 nm for 100 nm Ag NPs (Figure 5.2 and Figure A.4). Considering the trends from the Figure 5.2 and Figure A.4, T and E parameters can be chosen from the proposed L_C and L_D calculations (Table 5.2).

The number of detected particles (Label E in Figure A.3) is an important parameter in quantitative SP-ICP-MS applications and was, therefore, used here to identify suitable ion clouds extraction conditions (Figure A.5 and Figure A.6). It was found that there was a significant difference in the number of detected particles in the case of 20 nm sized Ag NPs with the change of extraction conditions, however, this happens because they could not completely be separated

from the BG. The trends are more difficult to follow (Figure A.5 and Figure A.6), with the number of detected NPs being more dependent on E than on T. In general, it was found that a relatively wide range of extraction conditions can be used for larger sized NPs, specifically for 60 nm and 100 nm Ag NPs, because only minimal differences in the number of detected NPs were obtained. The number of detected

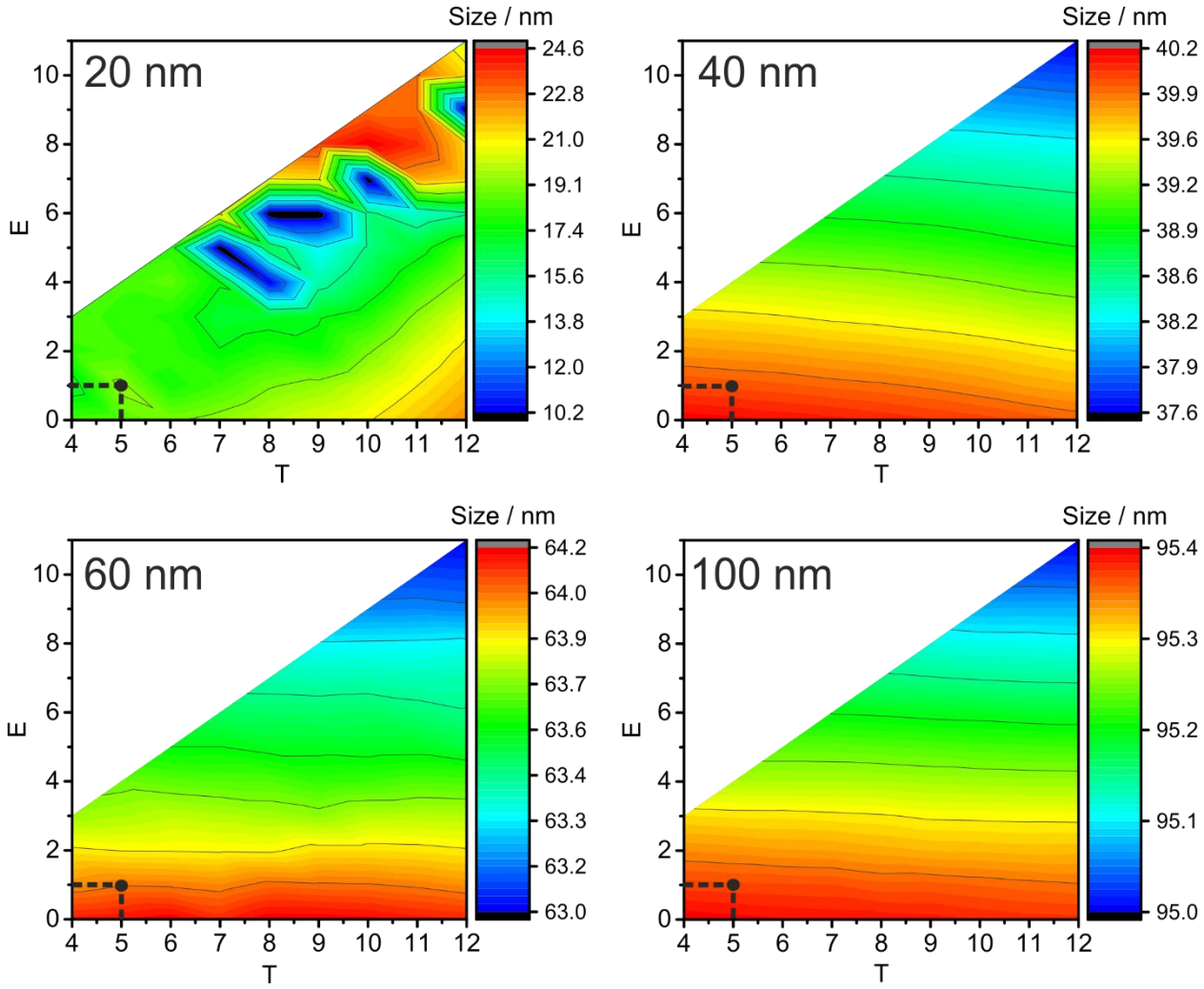

Figure 5.2: Average sizes of 20, 40, 60, 100 nm Ag NPs size distributions (without addition of Ag^+, 0 µg L^{-1}, to NP suspension) depending on different count thresholds during ion cloud extraction (T – number of counts required to flag ion cloud start and E – number of counts to define end of ion cloud extraction). Optimal conditions (S = 5, T = 5, E = 1) are highlighted with black dots. Note: The step size in size resolution is for illustrative purposes only and is a result of data processing. It does not represent the actual size resolution of the SP-ICP-MS method. Also, areas of white colour indicate extraction conditions, which were not tested.

20 nm Ag NPs and 40 nm NPs with Ag^+ above 1 µg L^{-1} were significantly affected by the extraction conditions, with few hundreds more NPs detected with the extraction conditions below L_C and L_D (false positives). Clearly, the choice of extraction conditions according to L_C and L_D assures a more reliable detection of smaller sized NPs.

The next parameter to consider is the BG maximum (Label A in Figure A.3). A high BG results in a high number of false positive, hinders the detection of NPs with sizes close to the BG, and increases the file size, which leads to time-consuming data processing. In the study, the BG was high at low T values, and found to be mostly independent of E values (Figure 5.3); therefore, T is the decisive factor in choosing the BG. Similar trends are detected for all NPs sizes and all the concentrations of Ag^+ that were tested: the BG decreases with increasing T values.

If Gaussian distribution would be used instead of Poisson distribution, then the decision threshold would be $3\times SD_{BG}$. For example, let us calculate this threshold for 60 nm Ag NPs with 7.5 µg L^{-1} Ag^+ and Gaussian distribution. With average BG of 29.033 ± 1.178 counts in 25 µs, L_D for Gaussian distribution is 32.567 counts or 33 counts, if rounded. The optimal conditions obtained with Poisson statistics are higher (T = 51, E = 39, Figure 3) than the ones obtained with Gaussian statistics. In Figure 5.3 it can be seen that, when T = 40, E = 33, the BG that was extracted from the raw data was high, around 100,000 events at BG maximum (file size approximately 14 Mb each). When Gaussian statistics were used, the average NP size (at T = 40, E = 33) was higher than the NP size detected at T = 51, E = 39 (Figure A.4), the BG maximum was significantly higher (cf. Figure 5.3, T = 40, E = 33), the number of detected NPs was decreasing (cf. Figure A.6, T = 40, E = 33), and the size starting from which NPs could be distinguished from the BG significantly increased by 10 nm (cf. Figure 5.3, at T = 40, E = 33); compared to T = 51, E = 39 as optimal extraction conditions with Poisson statistics. In conclusion, Gaussian distribution statistics at low number of counts (average BG below 100 counts) results in thresholds underestimation in SP-ICP-MS: more BG is extracted together with NPs, and, in turn, the detection and characterization of the NPs is less precise.

Considering all the parameters discussed in the section, L_C and L_D can be used for quantitative extraction of NP ion clouds. As an option, T parameter may be chosen 4-5 counts above the L_D value to decrease the BG further, which will not significantly affect the size or the number of extracted NPs.

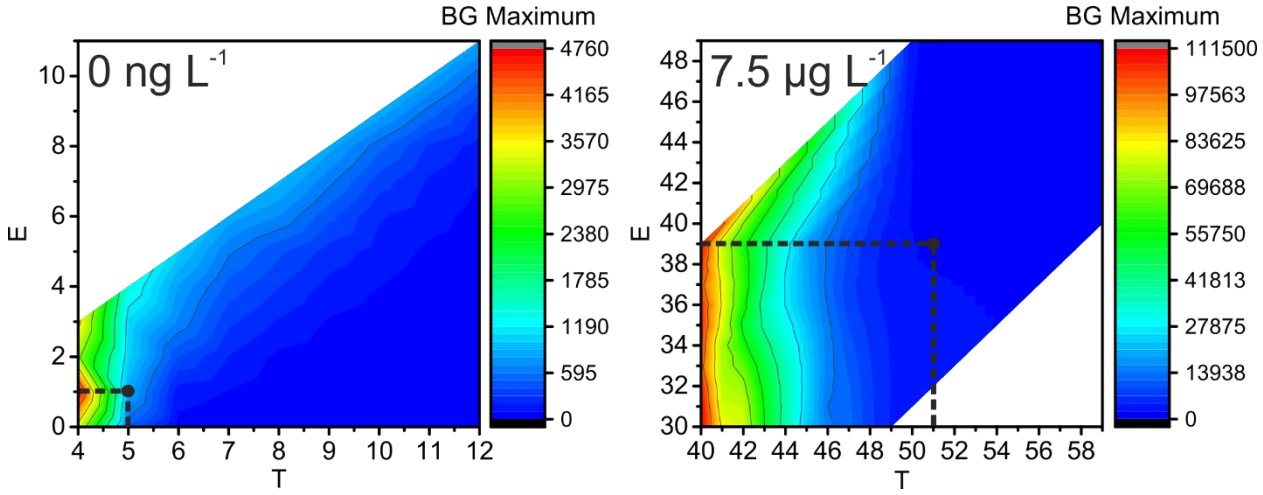

Figure 5.3: Influence of ion cloud extraction conditions on maximum of the number of BG events (BG count distribution maximum, see Label A in Figure A.3) during the analysis of 60 nm Ag NPs (left: without, and right: with 7.5 µg L^{-1} Ag^+ added to the NP suspension). Optimal conditions are highlighted with black dots. Note: The step size in size resolution is for illustrative purposes only and a result of data processing. It does not represent the actual size resolution of the SP-ICP-MS method. Also, areas of white colour indicate extraction conditions, which were not tested.

5.3.6 Workflow after Method Optimization

The developed data processing procedure for SP-ICP-MS and µsDAQ allows to extract the NPs in the presence of up to 1,000,000 cps of BG signal using Poisson statistics to determine thresholds to identify beginning and end of NP signal events. Higher BG signals were not tested because of the use of the SEM in the counting mode. The principle of the data processing algorithm can be extended to different types of NPs, detection of different elements, or to NPs containing high natural or instrumental BG. The method allows to quantify NPs in a wider range of the BG signal, compared to conventional SP-ICP-MS with millisecond DT.

In order to determine the concentration of dissolved metal in the presence of NPs and to assess the NP size distribution the following steps are proposed:

- Perform a calibration with dissolved metal with millisecond DT (e.g. 10 ms). This is done in order to ascertain the concentration of dissolved metal in the mixture, taking into account possible matrix effects.
- Construct the signal distribution after sample analysis to determine the average BG. It represents the dissolved metal concentration.
- In order to determine the NPs size distribution, extract the NP ion clouds from the data obtained with the µsDAQ. This is done by setting thresholds (S, T, E), and the threshold typically increase with the increasing BG signal. The thresholds can be calculated using the average BG obtained from the vendor software from cumulative Poisson distribution or with the normality approximation (Table 5.2). The ion cloud beginning threshold (T) may be increased by 4-5 counts to decrease the BG further.
- Subtract the average BG from each ion cloud to obtain more precise sizing information.
- Construct the size distribution based on the NPs size calibration.

5.4 Conclusion

A data processing procedure was developed for SP-ICP-MS with microsecond time resolution (µsDAQ) to determine both the concentration of dissolved metal and NPs sizes in a mixture using Poisson statistics to determine thresholds to identify beginning and end of NP signal events. Possible matrix effects were discussed, and the BG subtraction procedure was developed in order to obtain more precise quantitative information on the NPs. Data acquired with millisecond DT was used to determine the average BG, which relates to the concentration of the dissolved ionic species. Data acquired with the µsDAQ was used for the characterization of NPs. NPs were extracted based on thresholds, which were related to quantitative limits (L_C and L_D) for Poisson distribution to get probability theory based NP ion cloud extraction from the raw data. Different extraction condition combinations were tested and used to verify the use of L_C and L_D for NP ion clouds extraction. The developed method is based on Ag NPs detection, but it can be universally used with NPs containing elements detectable by ICP-MS, high natural BG or high dissolved ion concentration; it can also be used for environmental samples or NPs production quality control.

Chapter 6

Concluding Remarks and Future Perspectives

Based on:

D. Mozhayeva, C. Engelhard, A Critical Review of Single Particle Inductively Coupled Plasma Mass Spectrometry – A Step Towards the Ideal Method for Nanomaterials Characterization, *J. Anal. At. Spectrom.*, 2019, DOI: 10.1039/C9JA00206E.

D. Mozhayeva, I. Strenge, C. Engelhard, Implementation of Online Preconcentration and Microsecond Time Resolution to Capillary Electrophoresis Single Particle Inductively Coupled Plasma Mass Spectrometry (CE-SP-ICP-MS) and its Application in Silver Nanoparticle Analysis, *Anal. Chem.*, 2017, **89**, 7152-7159.

D. Mozhayeva, C. Engelhard, Separation of Silver Nanoparticles with Different Coatings by Capillary Electrophoresis Coupled to ICP-MS in Single Particle Mode, *Anal. Chem.*, 2017, **89**, 9767-9774.

D. Mozhayeva, C. Engelhard, A Quantitative Nanoparticle Extraction Method for Microsecond Time Resolved Single-Particle ICP-MS Data in the Presence of High Background, *J. Anal. At. Spectrom.*, 2019, DOI: 10.1039/c9ja00042a.

6.1 Summary and Concluding Remarks

In this thesis, novel methods for NP analysis were carefully developed and optimized. CE-SP-ICP-MS was used for the first time with online preconcentration and microsecond time resolution SP-ICP-MS for separation and characterization of Ag NPs. Moreover, the optimized method was used to separate Ag NPs with similar sizes and different coatings for the first time. A novel data processing approach was introduced to extract NP ion clouds from the data acquired with microsecond time resolution based on decision criteria of Poisson distribution.

Recent developments in SP-ICP-MS were reviewed in Chapter 2. The method substantially developed since a first report in 2003,[16] however, more instrumental developments in sample introduction, ionization conditions, ion transport to MS, and MS would help to achieve lower L_D and minimize matrix effects. SP-ICP-MS has already been applied in different fields, including model and real aqueous samples, some biological and solid matrices. Care should be taken that all the ICP-MS instrumental conditions are stated in publications, because the choice of the plasma conditions affects the detection of NPs in different matrices.

In Chapter 3, a novel method, CE-SP-ICP-MS, was used for the first time with REPSM and SP-ICP-MS detection with microsecond time resolution. CE separation of NPs added an extra dimension to SP-ICP-MS analysis. After optimization of the preconcentration conditions, 110 s injection with REPSM and a CE separation at 20 kV were found to be the optimum for the separation of 20, 40, and 60 nm sized Ag NPs. The capability of CE-SP-ICP-MS to do quantitative analysis was demonstrated, and linear calibration curves could be obtained with detection limits in sub-microgram-per-liter-range. CE-SP-ICP-MS made it possible to separate NPs by size and get information on NPs average size, size distribution, and PNC at any chosen time period during a CE separation. The data could be visualized with two-dimensional color maps, simplifying data evaluation and representation.

In the next experimental study (Chapter 4), an optimized CE-SP-ICP-MS method was used to separate mixtures of Ag NPs with different coatings for the first time. Different CE migration profiles and MTs for the NPs with different

coatings were successfully obtained. It was found that NPs with polymeric coatings migrate with their coatings attached to the NP surface and have relatively short MTs. NPs with a monomeric citrate coating might experience partitioning with SDS molecules and, in turn, could be separated with high size resolution but at longer MTs. On the basis of these results, it could be concluded that the characterization of NPs simply by their size is not sufficient and that the coating should also be considered, especially when NP standards are used for calibration of the CE-ICP-MS method. It was found here that CE-SP-ICP-MS is able to distinguish every NP type in a five-component mixture of 20, 40, and 60 nm sized citrate-coated NPs and 40 and 60 nm sized PVP-coated NPs by resolving NPs with similar MTs due to the additional SP-ICP-MS NP size domain.

Chapter 5 was focused on development of a new data processing algorithm for SP-ICP-MS with microsecond time resolution. The developed algorithm allowed to determine both the concentration of dissolved metal and NPs sizes in a mixture using Poisson statistics. NPs were extracted based on thresholds, which were related to qualitative limits (L_C and L_D) for Poisson distribution to extract NP ion cloud extraction from the raw data. The developed method was based on Ag NPs detection, but it could be universally used with NPs containing elements detectable by ICP-MS, high natural BG or high dissolved ion concentration.

6.2 Future Perspectives

Fundamental developments as well as applications of SP-ICP-MS are expected to stay an important research area in the coming years. Chapter 2 highlights the areas, where SP-ICP-MS still needs some fundamental developments. Namely, more robust and efficient nebulizers would simplify the sample introduction for different complex matrices. Optimized plasma conditions would ensure complete ionization of NPs irrespective of the matrix they are in. An improved interface between the ICP and the MS would improve the transport efficiency of the NPs and minimize the losses of the ions, when they are transferred to vacuum. An ideal MS would be able to perform sensitive simultaneous multielemental detection, be robust and affordable in cost, and achieve single atom L_D. These are the "ideal" characteristics of SP-ICP-MS that may be a cornerstone aim in the fundamental developments of the method.

CE-SP-ICP-MS (Chapter 3) has a potential to become a widely used method for NPs separation and analysis. This method still has certain limitations that should be addressed in the future. Now the method can be used in research and still requires an experienced operator. Quantification approaches can be further developed, when PNC NP standards will be available on the market. Other CE preconcentration strategies may help to expand the size range and types of NPs that can be separated and to decrease the L_D below sub-microgram-per-liter range. Simultaneous detection of several isotopes will be of help in analyzing more complex mixtures. Also, the coupling interface can be improved to make the technique more readily accessible. If these conditions are met, a broader use of CE-SP-ICP-MS is anticipated with applications, for example, in environmental and nanotoxicology research as well as consumer products analyses.

The separation of NPs with different coatings with CE-SP-ICP-MS (Chapter 4) may provide more information about the state of NPs in the environment, help to better understand toxicity of various types of NPs, and provide a tool of extensive NPs characterization during or after their production. As the surface coating of NPs is an important parameter that determines NP reactivity, CE-SP-ICP-MS may help to understand the stability of the coating

depending on the MT pattern that is obtained. Further tests can be made on greater number of NPs types with positive and negative surface coatings of different nature, when a greater number of well characterized NPs will be available on the market. Also, further investigations are needed to learn more about the separation mechanism of positively charged NPs and to answer the question why it was not possible to separate the BPEI-coated NPs from any of the negatively charged NPs.

SP-ICP-MS with microsecond time resolution can now be used to quantify both NPs and dissolved metal in a mixture (Chapter 5). New automated data processing algorithms for treatment of the SP-ICP-MS data would simplify the use of the method for routine applications. Nowadays, visualization of a complete data set e.g. after only 1 min of 5 μs resolved measurement is not possible with the average computers used in research, and typical software can load only around few million data points at once. Therefore, the development of specialized tools for SP-ICP-MS data processing would make it much faster. The integration of machine learning or data mining algorithm would improve and simplify the data processing procedures for SP-ICP-MS.

The future developments in SP-ICP-MS and CE-SP-ICP-MS, in the opinion of the author, require joint integrated forces of different fields of science. Specialists from physics, chemistry, engineering, statistics, and computer science would help to improve the existing instrumentation. The data processing could be automated with the help of the computer scientists and, in particular, artificial intelligence. New application of the method could be developed by chemists together with biologists. To sum up, SP-ICP-MS and CE-SP-ICP-MS have the potential to become routine methods for NPs analysis using the developments that were introduced in the current thesis, and after addressing the challenges mentioned above.

Appendix

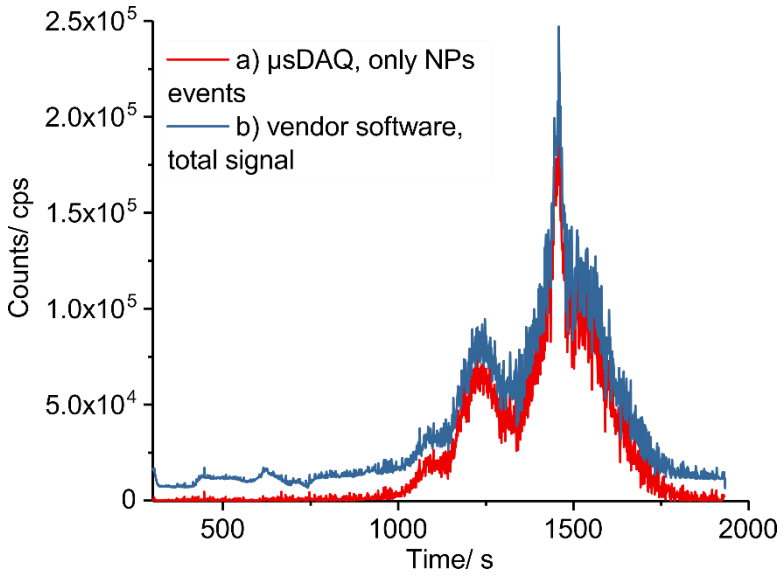

Figure A.1: CE-ICP-MS diagrams obtained with 1 s dwell time ($^{107}Ag^{+}$) (A) by summing up only extracted NPs events from µsDAQ and (B) by summing up 10 ms DTs in the vendor software for a mixture of 5 µg L^{-1} 20 nm sized, 35 µg L^{-1} 40 nm sized, and 200 µg L^{-1} 60 nm sized Ag NPs analyzed using 110 s injection time in REPSM at 20 kV.

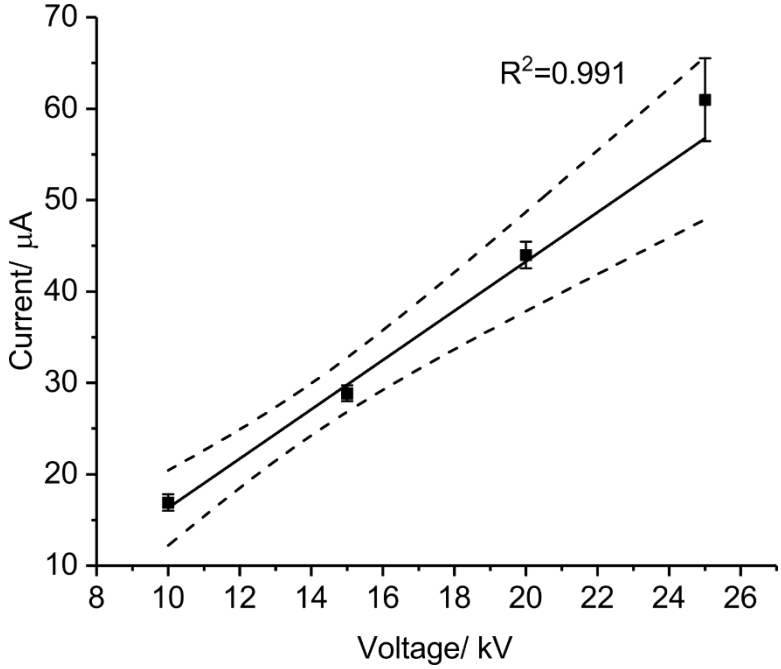

Figure A.2: Influence of applied voltage on the current in CE using 110 s injection time in REPSM (linear fit with 95% confidence levels).

Table A.1: Characteristics of one-component Ag NPs dispersions.*

Nominal diameter/ nm	Diameter (TEM)/ nm	Surface coating	Zeta potential for concentrated 20 mg L^{-1} suspensions/ mV	MT/ s	RSD/ %
20	18.5 ± 3.4	citrate	-43.4	10855 ± 10	0.92
20	21.2 ± 3.1	PVP	-37	10625 ± 12	1.09
40	39 ± 4	citrate	-47	12755 ± 115	9.05
40	41 ± 5	PVP	-36	10485 ± 15	1.46
40	41 ± 4	PEG	-23	9585 ± 32	3.35
40	39.7 ± 3.6	BPEI	+73	9585 ± 21	2.17
60	62 ± 7	citrate	-51	15155 ± 105	6.91
60	60 ± 6	PVP	-39	10985 ± 21	1.90
60	59.6 ± 5.8	PEG	-25.5	9685 ± 6	0.60

* Diameter, surface coating, and zeta potential are provided by the manufacturer. MTs are the maxima of the corresponding profiles obtained by CE-SP-ICP-MS with SD and RSD, (n=3). Zeta potentials are presented only for qualitative comparison.

Table A.2: MTs of two-component Ag NPs dispersions.*

Nominal diameter/ nm	Surface coating 1	Surface coating 2	MT 1/ s	RSD 1/ %	MT 2/ s	RSD 2/ %
20	PVP	citrate	1088 ± 15	1.38	-	-
40	BPEI	PEG	1042 ± 6	0.55	-	-
40	BPEI	PVP	1122 ± 35	3.13	-	-
40	BPEI	citrate	1278 ± 65	5.09	-	-
40	PEG	PVP	898 ± 82	9.07	-	-
40	PEG	citrate	995 ± 30	3.02	1282 ± 57	4.44
40	PVP	citrate	1122 ± 6	0.51	1412 ± 29	2.04
60	PEG	PVP	968 ± 15	1.58	-	-
60	PEG	citrate	1008 ± 6	0.57	-	-
60	PVP	citrate	1118 ± 6	0.52	1272 ± 21	1.64

*MTs are the maxima of the corresponding profiles obtained by CE-SP-ICP-MS with SD and RSD, (n = 3). MT 1 corresponds to the component with Surface coating 1, and MT 2 corresponds to the component with Surface coating 2, when two components are separated by CE-SP-ICP-MS. When a mixture is not separated, the mixture´s MT is presented as MT 1.

Chapter A.1 Size Distribution Characteristics

The following size distribution characteristics are used in Chapter 5 to describe NP size histograms and to compare the effects of extraction conditions on the final NP size distribution (Figure A.3):

BG maximum (maximum number of extracted events in the background distribution in 2-nm bins. BG maximum is a rough indication of the quality of the ion clouds extraction process. The goal is to extract the NPs from the raw data, and not the BG.Higher number of the extracted BG counts makes the data files larger and the processing slower, also it may affect the extraction of NPs with lower sizes) (Label A in Figure A.3);

NPs average size (to determine the influence of the ion clouds extraction conditions on the obtained mean NP size) (Label B in Figure A.3);

width "W" of the size distribution that equals to two SDs of the NPs average size (W = 2SD, Label C in Figure A.3);

size starting from which the NP size distribution can be distinguished (if NPs are not completely separated from the BG, starting from the lowest point between the BG and the size distribution) (Label D in Figure A.3);

total number of NPs detected in the size distribution (Label E in Figure A.3).

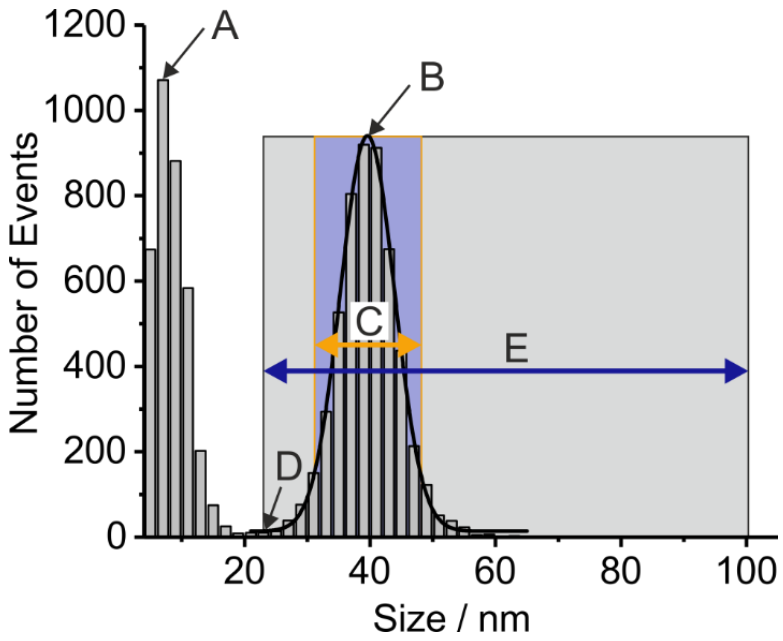

Figure A.3: Model histogram with labels that indicate parameters of a NPs size distribution that are used in Chapter 5 to compare different extraction conditions: BG maximum (A), NPs average size (B), width "W" of the size distribution (C, W = 2SD of the NPs average size), minimal size from which NPs can be distinguished from the BG (D), and total number detected of NPs (E).

Chapter A.2 Calculation of L_C and L_D for exact Poisson distribution with "well-known" BG

According to Currie[292, 293], a cumulative Poisson distribution can be used for the calculations:

$$P(y, \lambda) = \sum_{i=0}^{y} \frac{e^{-\lambda}\lambda^{i}}{i!} \quad \text{(Equation A. 1)}$$

The critical limit (L_C) can be expressed as:

$$P(y > y_C, \lambda = \mu_B) \leq \alpha \quad \text{(Equation A. 2)}$$

The detection limit (L_D) can be expressed as:

$$P(y \leq y_C, \lambda = y_D) = \beta \quad \text{(Equation A. 3)}$$

In formulas (A. 2) and (A. 3), y is the number of gross counts, μ_B is the average BG counts, α is the error of the first kind, β is the error of the second kind, y_C is the critical number of gross counts (including the BG), and y_D is the detection limit for gross counts. L_C and L_D values are net counts after BG subtraction. μ_B, y_C, and y_D may be non-integer numbers because they represent mean parameters of the Poisson distribution.

Determination of y_C and y_D can be done with the tables presented in the original publications.[292, 293] Alternatively, an example calculation of y_C and y_D using cumulative Poisson distribution is presented in Table A.3. First, the average BG (μ_B in 25 µs since S = 5) is taken, which is recalculated from the vendor software to the desired time interval. Then y_C is chosen in a way that the cumulative probability $P(y > y_C, \mu_B)$ would be below 0.05. With a known y_C (e.g. $y_C = 5$), y_D is chosen for $P(y \leq y_C, y_D)$ to be equal to 0.05 (in the example y is changing from 0 to 5). Therefore, $y_C = 5$ and $y_D = 10.51$; after BG subtraction $L_C = 2.88$, $L_D = 8.39$. For the ion cloud extraction the following parameters may be chosen if y_C and y_D are rounded: S = 5, T = 10 or 11, and E = 5.

Table A.3: Example calculation of y_C, critical number of gross counts, and y_D, detection limit for gross counts, for a suspension of 20 nm Ag NPs spiked with 500 ng L^{-1} Ag^+ according to the previous page descriptions.

y	μ_B in 25 µs (S = 5)	$P_i(y, \mu_B)$	y_D	$P_i(y, y_D)$
0	2.117	0.120	10.51	2.73×10^{-5}
1	2.117	0.255	10.51	2.87×10^{-4}
2	2.117	0.270	10.51	1.51×10^{-3}
3	2.117	0.190	10.51	5.27×10^{-3}
4	2.117	0.101	10.51	0.014
5	2.117	0.043	10.51	0.029
6	2.117	0.015	10.51	0.051
7	2.117	0.005	10.51	0.077
8	2.117	1.20×10^{-3}	10.51	0.101
9	2.117	2.83×10^{-4}	10.51	0.118
10	2.117	6.00×10^{-5}	10.51	0.124
11	2.117	1.15×10^{-5}	10.51	0.118
12	2.117	2.04×10^{-6}	10.51	0.103
13	2.117	3.32×10^{-7}	10.51	0.084
14	2.117	5.02×10^{-8}	10.51	0.063
Resulting cumulative Poisson distribution probabilities, y_C, and y_D				
	y_C	$P(y > y_C, \mu_B) = \sum_{i=6}^{\infty} P_i \leq 0.05$	y_D	$P(y \leq y_C, y_D) = \sum_{i=0}^{5} P_i = 0.05$
	5	0.021	10.51	0.050

Table A.4: Gross size detection limit ($\boldsymbol{y_D}$) for selected ion clouds extraction conditions calculated for a suspension of 20 nm Ag NPs spiked with different concentrations of Ag^+ in solution.*

C_{Ag^+} / ng L^{-1}	T	E	μ_B / nm	$\boldsymbol{y_D}$ / nm
0	5	1	7	16
10	5	1	7	16
50	5	1	7	16
100	6	2	7	16
500	11	5	9	19
1000	15	8	10	20
2500	23	15	11	22
5000	38	28	13	24
7500	51	40	13	25

*The $\boldsymbol{y_D}$ is calculated only for selected extraction conditions based on the Table 5.3. The formula $y_D = \mu_B + 3.29\sqrt{\mu_B}$ was used for the calculations, assuming normal distribution with the standard deviation of the Poisson distribution. μ_B was taken from the constructed size distributions. Note that counting statistics was assumed also for the size of NPs since size distributions were constructed by counting the number of events of a certain size.

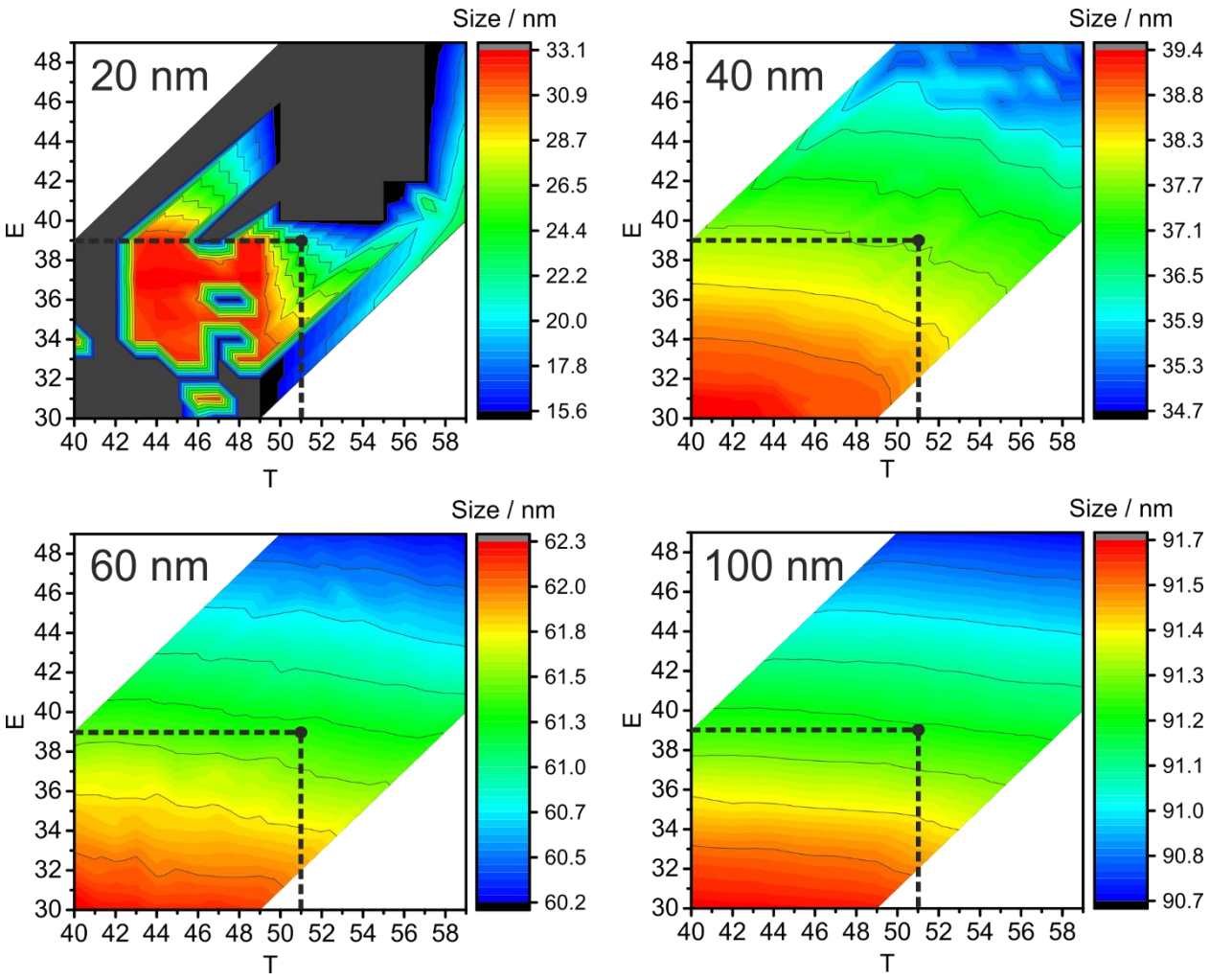

Figure A.4: Average sizes of 20, 40, 60, 100 nm Ag NPs size distributions (NP suspensions in the presence of 7.5 µg L^{-1} of Ag^{+}) depending on different count thresholds during ion cloud extraction, T and E. Optimal conditions (S = 5, T = 51, E = 39) are highlighted with black dots. Note: The step size in size resolution is for illustrative purposes only and is a result of data processing. It does not represent the actual size resolution of the SP-ICP-MS method. Also, areas of white color indicate extraction conditions, which were not tested.

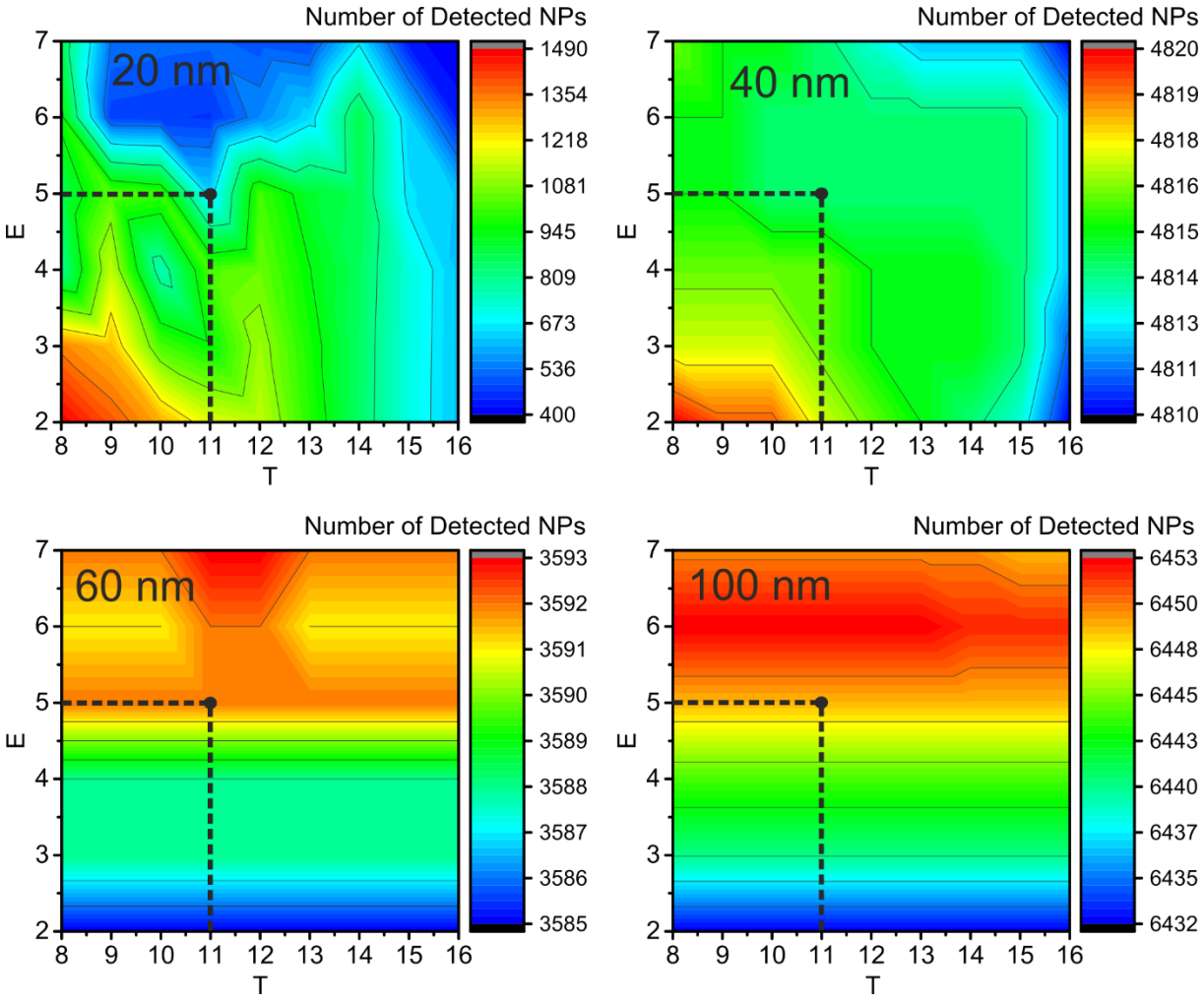

Figure A.5: Number of detected NPs for the 20, 40, 60, 100 nm Ag NPs (with 0.5 µg L^{-1} of Ag^{+} in solution) depending on different count thresholds during ion cloud extraction, T and E. Optimal conditions (S = 5, T = 11, E = 5) are highlighted with black dots. The step size in size resolution is for illustrative purposes only and is a result of data processing. It does not represent the actual size resolution of the SP-ICP-MS method. Also, areas of white color indicate extraction conditions, which were not tested.

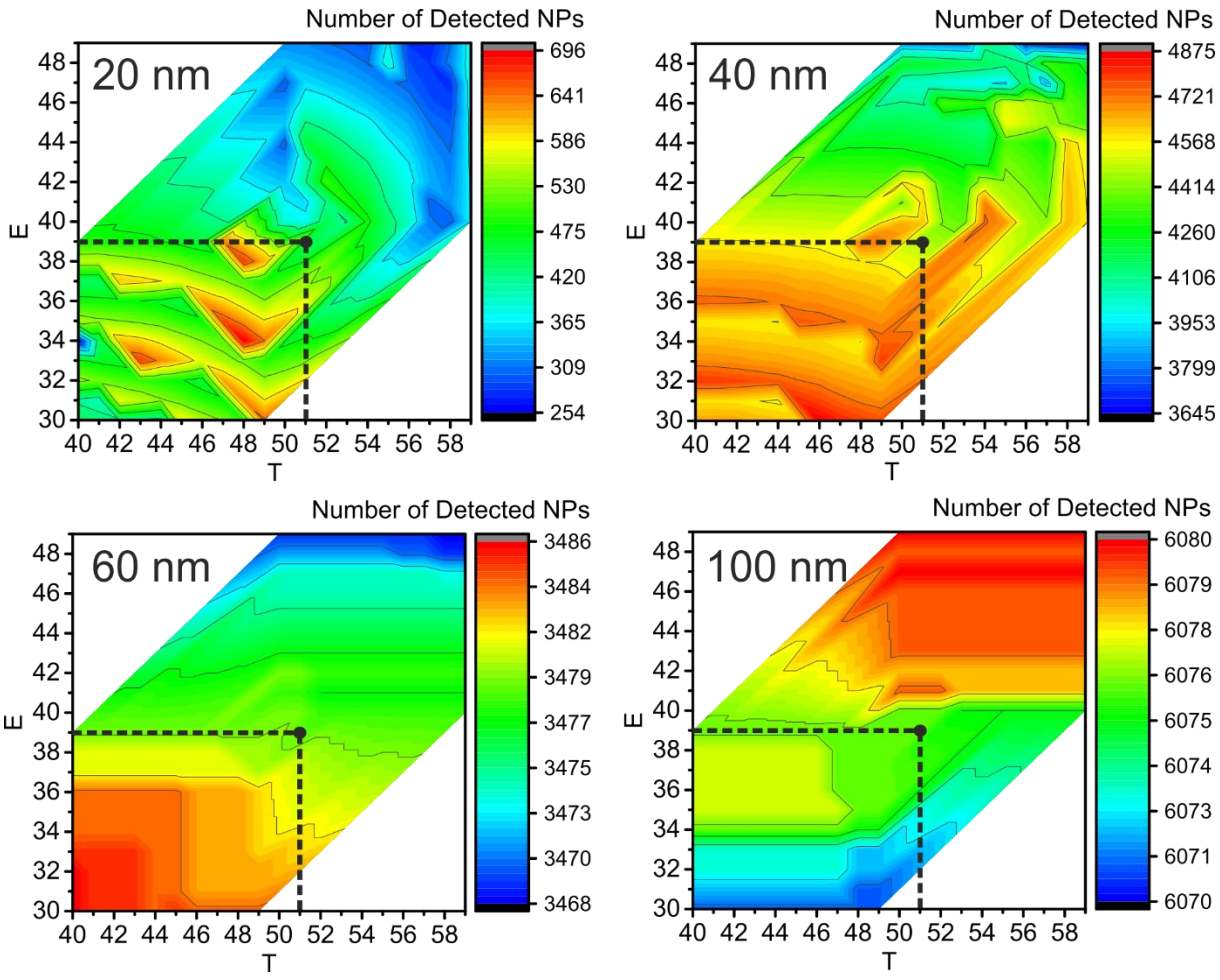

Figure A.6: Number of detected NPs for the 20, 40, 60, 100 nm Ag NPs (with 7.5 µg L^{-1} of Ag^{+}) depending on different count thresholds during ion cloud extraction, T and E. Optimal conditions (S = 5, T = 51, E = 39) are highlighted with black dots. The step size in size resolution is for illustrative purposes only and is a result of data processing. It does not represent the actual size resolution of the SP-ICP-MS method. Also, areas of white color indicate extraction conditions, which were not tested.

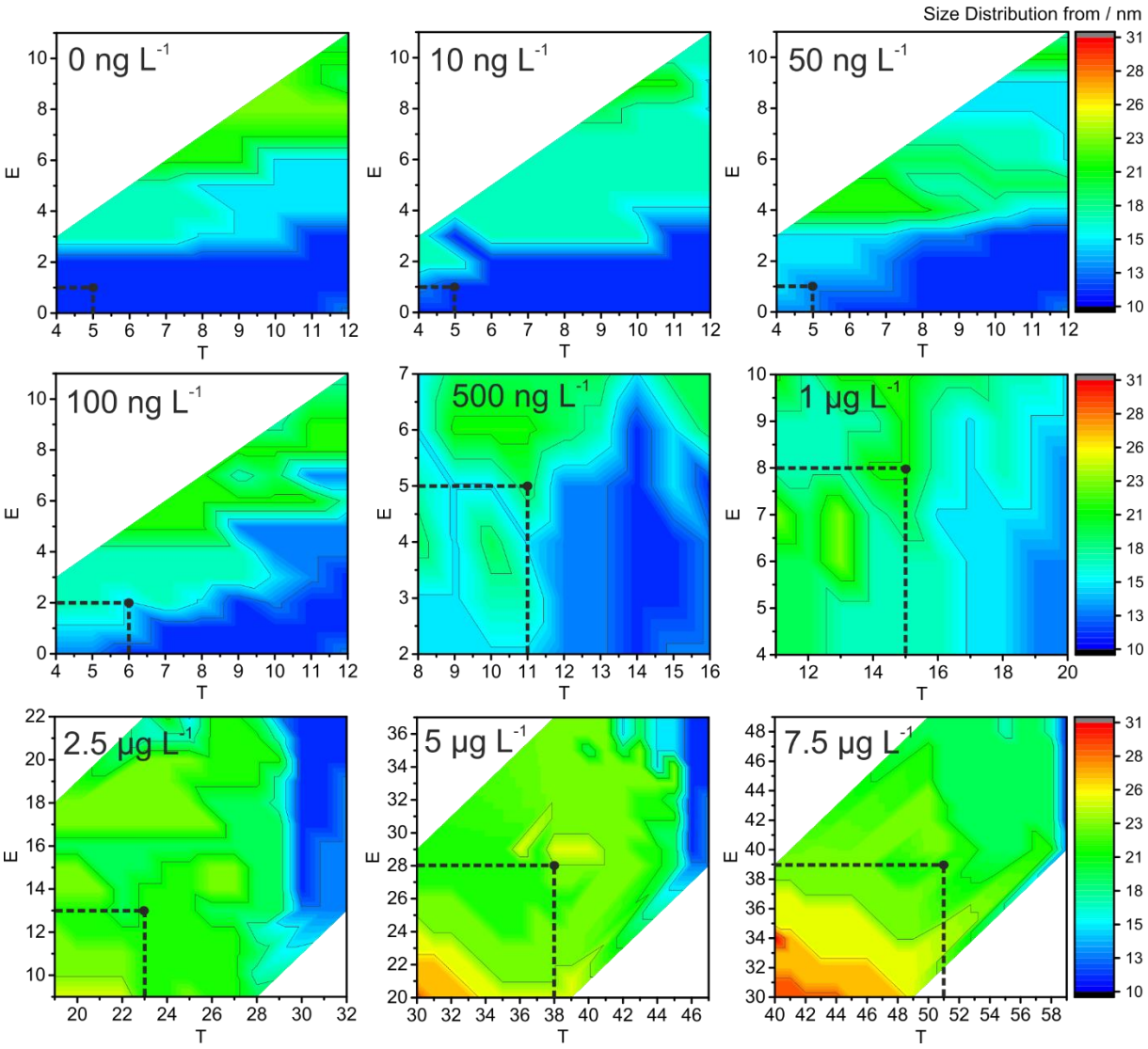

Figure A.7: Size starting from which the NP size distribution can be distinguished from the BG for 20 nm Ag NPs at different Ag^+ concentrations (shown on the graphs) depending on different count thresholds during ion cloud extraction, T and E. Optimal conditions are highlighted with black dots. The step size in size resolution is for illustrative purposes only and is a result of data processing. It does not represent the actual size resolution of the SP-ICP-MS method. Also, areas of white color indicate extraction conditions, which were not tested.

Chapter A.3 On the Selection of the NP Suspensions Matrix

When dissolved silver ions were added to the NPs suspensions in bi-distilled water, it was difficult to get a stable sample nebulization (frequent interruptions of the nebulizer flow). To prevent the formation of silver hydroxide in the neutral suspension and to decrease the surface tension of the bi-distilled water (high surface tension hinders the wettability of the plastic nebulizer) HNO_3 and $NaNO_3$ were added to the NP suspensions as matrix modifiers. When HNO_3 or $NaNO_3$ were added, also nebulization became stable. It was found that the presence of 0.1% (w/v) $NaNO_3$ significantly decreases the apparent average size of 40 nm NPs to 86.7 ± 2.4% and 40 nm NPs with 500 μg L^{-1} Ag^+ to 85.4 ± 1.1% of the original size in bi-distilled water (μsDAQ) in the course of seven hours of exposure. Since sodium is an EIE, it may suppress the ionization of silver[294], causing the decrease in NPs intensities. In 0.1% (w/v) HNO_3 the NPs size changed but to a lower extent to 92.7 ± 4.6% for 40 nm NPs and to 101.5 ± 4.2% for 40 nm NPs with 500 μg L^{-1} Ag^+ compared to the size in bi-distilled water (μsDAQ) in the course of seven hours of exposure. A lower concentration 0.025% (w/v) of HNO_3 was used further to stabilize the suspensions. Although NP size decreases up to 14% compared to the initial value in the presence of 0.025% (w/v) HNO_3 and without ionic silver in the course of seven hours, in the presence of 0.025% (w/v) HNO_3 and 1 μg L^{-1} Ag^+ the size changes less than 5.4% over the course of seven hours (μsDAQ). Maximum 3.8% deviation from the initial value was detected in the intensity of 1 μg L^{-1} Ag^+ in the presence of 40 nm NPs and 0.025% (w/v) HNO_3 over 7 hours after the sample preparation. Therefore, the citrate-capped NPs are stabilized in the presence of ionic silver together with traces of nitric acid, and 0.025% (w/v) HNO_3 was added to each sample in the further measurements, and the samples were analyzed not later than two hours after preparation. This set of experiments highlighted the importance of the matrix choice in SP-ICP-MS.

References

1. The Nanodatabase, http://nanodb.dk/en/search-database/, (accessed May 28, 2019).
2. The Project of Emerging Nanotechnologies. Consumer Products Inventory, http://www.nanotechproject.org/cpi/, (accessed May 28, 2019).
3. C. Levard, E. M. Hotze, G. V. Lowry and G. E. Brown, Jr., Environmental transformations of silver nanoparticles: impact on stability and toxicity, *Environ. Sci. Technol.*, 2012, **46**, 6900-6914.
4. T. Y. Sun, F. Gottschalk, K. Hungerbühler and B. Nowack, Comprehensive probabilistic modelling of environmental emissions of engineered nanomaterials, *Environ. Pollut.*, 2014, **185**, 69-76.
5. F. Gottschalk, T. Sun and B. Nowack, Environmental concentrations of engineered nanomaterials: review of modeling and analytical studies, *Environ. Pollut.*, 2013, **181**, 287-300.
6. M. Hassellöv, J. W. Readman, J. F. Ranville and K. Tiede, Nanoparticle analysis and characterization methodologies in environmental risk assessment of engineered nanoparticles, *Ecotoxicology*, 2008, **17**, 344-361.
7. F. Laborda, J. Jiménez-Lamana, E. Bolea and J. R. Castillo, Selective identification, characterization and determination of dissolved silver(i) and silver nanoparticles based on single particle detection by inductively coupled plasma mass spectrometry, *J. Anal. At. Spectrom.*, 2011, **26**, 1362-1371.
8. F. Laborda, E. Bolea and J. Jiménez-Lamana, Single particle inductively coupled plasma mass spectrometry: a powerful tool for nanoanalysis, *Anal. Chem.*, 2014, **86**, 2270-2278.
9. M. D. Montaño, J. W. Olesik, A. G. Barber, K. Challis and J. F. Ranville, Single Particle ICP-MS: Advances toward routine analysis of nanomaterials, *Anal. Bioanal. Chem.*, 2016, **408**, 5053-5074.
10. B. Meermann and V. Nischwitz, ICP-MS for the analysis at the nanoscale – a tutorial review, *J. Anal. At. Spectrom.*, 2018, **33**, 1432-1468.
11. I. Strenge and C. Engelhard, Capabilities of fast data acquisition with microsecond time resolution in inductively coupled plasma mass spectrometry and identification of signal artifacts from millisecond dwell times during detection of single gold nanoparticles, *J. Anal. At. Spectrom.*, 2016, **31**, 135-144.
12. G. M. Hieftje, Howard Malmstadt – Toward the ideal, *Spectrochim. Acta B*, 2006, **61**, 597-598.
13. R. P. Feynman, There's plenty of room at the bottom, *Eng. Sci.*, 1960, **23**, 22-36.
14. M. Faraday, Experimental relations of gold (and other metals) to light, *Philos. Trans. R. Soc. Lond.*, 1857, **147**, 145-181.
15. F. R. S. Thomas Graham, Liquid diffusion applied to analysis, *Philos. Trans. R. Soc. Lond.*, 1861, **151**, 183-224.

16. C. Degueldre and P. Y. Favarger, Colloid analysis by single particle inductively coupled plasma-mass spectroscopy: a feasibility study, *Colloids Surf. A Physicochem. Eng. Asp.*, 2003, **217**, 137-142.
17. F. Laborda, E. Bolea and J. Jiménez-Lamana, Single particle inductively coupled plasma mass spectrometry for the analysis of inorganic engineered nanoparticles in environmental samples, *Trends Environ. Anal. Chem.*, 2016, **9**, 15-23.
18. D. Mozhayeva, I. Strenge and C. Engelhard, Implementation of online preconcentration and microsecond time resolution to capillary electrophoresis single particle inductively coupled plasma mass spectrometry (CE-SP-ICP-MS) and its application in silver nanoparticle analysis, *Anal. Chem.*, 2017, **89**, 7152-7159.
19. H. Kawaguchi, N. Fukasawa and A. Mizuike, Investigation of airborne particles by inductively coupled plasma emission spectrometry calibrated with monodisperse aerosols, *Spectrochim. Acta B*, 1986, **41**, 1277-1286.
20. T. Nomizu, S. Kaneco, T. Tanaka, T. Yamamoto and H. Kawaguchi, Determination of femto-gram amounts of zinc and lead in individual airborne particles by inductively coupled plasma mass spectrometry with direct air-sample introduction, *Anal. Sci.*, 1993, **9**, 843-846.
21. S. Kaneco, T. Nomizu, T. Tanaka, N. Mizutani and H. Kawaguchi, Optimization of operating conditions in individual airborne particle analysis by inductively coupled plasma mass spectrometry, *Anal. Sci.*, 1995, **11**, 835-840.
22. T. Nomizu, H. Nakashima, Y. Hotta, T. Tanaka and H. Kawaguchi, Simultaneous measurement of the elemental content and size of airborne particles by inductively coupled plasma emission spectrometry combined with the laser light-scattering method, *Anal. Sci.*, 1992, **8**, 527-531.
23. T. Nomizu, H. Hayashi, N. Hoshino, T. Tanaka, H. Kawaguchi, K. Kitagawa and S. Kaneco, Determination of zinc in individual airborne particles by inductively coupled plasma mass spectrometry with digital signal processing, *J. Anal. At. Spectrom.*, 2002, **17**, 592-595.
24. M. Thompson, C. D. Flint, S. Chenery and K. Knight, Time resolved system for the analysis of particles in the inductively coupled plasma - preliminary studies, *J. Anal. At. Spectrom.*, 1992, **7**, 1099-1102.
25. K. Knight, S. Chenery, S. W. Zochowski, M. Thompson and C. D. Flint, Time-resolved signals from particles injected into the inductively coupled plasma, *J. Anal. At. Spectrom.*, 1996, **11**, 53-56.
26. C. Degueldre, P. Y. Favarger and C. Bitea, Zirconia colloid analysis by single particle inductively coupled plasma–mass spectrometry, *Anal. Chim. Acta*, 2004, **518**, 137-142.
27. C. Degueldre and P. Y. Favarger, Thorium colloid analysis by single particle inductively coupled plasma-mass spectrometry, *Talanta*, 2004, **62**, 1051-1054.
28. C. Degueldre, P. Y. Favarger, R. Rosse and S. Wold, Uranium colloid analysis by single particle inductively coupled plasma-mass spectrometry, *Talanta*, 2006, **68**, 623-628.

29. C. Degueldre, P. Y. Favarger and S. Wold, Gold colloid analysis by inductively coupled plasma-mass spectrometry in a single particle mode, *Anal. Chim. Acta*, 2006, **555**, 263-268.
30. G. M. Hieftje, A Brief Gaze into the Plasma Spectrochemistry Crystal Ball, Sankt Anton am Arlberg, Austria, 2017.
31. G. M. Hieftje, And Now What?, Amelia Island, FL, U.S.A., 2018.
32. F. Laborda, E. Bolea, G. Cepriá, M. T. Gómez, M. S. Jiménez, J. Pérez-Arantegui and J. R. Castillo, Detection, characterization and quantification of inorganic engineered nanomaterials: A review of techniques and methodological approaches for the analysis of complex samples, *Anal. Chim. Acta*, 2016, **904**, 10-32.
33. I. De la Calle, M. Menta and F. Séby, Current trends and challenges in sample preparation for metallic nanoparticles analysis in daily products and environmental samples: A review, *Spectrochim. Acta B*, 2016, **125**, 66-96.
34. J. W. Olesik and P. J. Gray, Considerations for measurement of individual nanoparticles or microparticles by ICP-MS: determination of the number of particles and the analyte mass in each particle, *J. Anal. At. Spectrom.*, 2012, **27**, 1143-1155.
35. S. I. Miyashita, H. Mitsuhashi, S. I. Fujii, A. Takatsu, K. Inagaki and T. Fujimoto, High transport efficiency of nanoparticles through a total-consumption sample introduction system and its beneficial application for particle size evaluation in single-particle ICP-MS, *Anal. Bioanal. Chem.*, 2017, **409**, 1531-1545.
36. S. Gschwind, L. Flamigni, J. Koch, O. Borovinskaya, S. Groh, K. Niemax and D. Günther, Capabilities of inductively coupled plasma mass spectrometry for the detection of nanoparticles carried by monodisperse microdroplets, *J. Anal. At. Spectrom.*, 2011, **26**, 1166-1174.
37. S. Gschwind, H. Hagendorfer, D. A. Frick and D. Günther, Mass quantification of nanoparticles by single droplet calibration using inductively coupled plasma mass spectrometry, *Anal. Chem.*, 2013, **85**, 5875-5883.
38. B. Ramkorun-Schmidt, S. A. Pergantis, D. Esteban-Fernández, N. Jakubowski and D. Günther, Investigation of a combined microdroplet generator and pneumatic nebulization system for quantitative determination of metal-containing nanoparticles using ICPMS, *Anal. Chem.*, 2015, **87**, 8687-8694.
39. S. Gschwind, M. d. L. A. Montes and D. Günther, Comparison of sp-ICP-MS and MDG-ICP-MS for the determination of particle number concentration, *Anal. Bioanal. Chem.*, 2015, **407**, 4035-4044.
40. B. Franze, I. Strenge and C. Engelhard, Single particle inductively coupled plasma mass spectrometry: evaluation of three different pneumatic and piezo-based sample introduction systems for the characterization of silver nanoparticles, *J. Anal. At. Spectrom.*, 2012, **27**, 1074-1083.
41. K. S. Ho, W. W. Lee and W. T. Chan, Effects of ionization potential of an element and boiling point of the corresponding oxide on the sensitivity of ICP-MS, *J. Anal. At. Spectrom.*, 2015, **30**, 2066-2073.

42. S. Groh, C. C. Garcia, A. Murtazin, V. Horvatic and K. Niemax, Local effects of atomizing analyte droplets on the plasma parameters of the inductively coupled plasma, *Spectrochim. Acta B*, 2009, **64**, 247-254.
43. A. Murtazin, S. Groh and K. Niemax, Investigation of sample introduction- and plasma-related matrix effects in inductively coupled plasma spectrometry applying single analyte droplet and particle injection, *Spectrochim. Acta B*, 2012, **67**, 3-16.
44. K. S. Ho, K. O. Lui, K. H. Lee and W. T. Chan, Considerations of particle vaporization and analyte diffusion in single-particle inductively coupled plasma-mass spectrometry, *Spectrochim. Acta B*, 2013, **89**, 30-39.
45. O. Borovinskaya, M. Aghaei, L. Flamigni, B. Hattendorf, M. Tanner, A. Bogaerts and D. Günther, Diffusion- and velocity-driven spatial separation of analytes from single droplets entering an ICP off-axis, *J. Anal. At. Spectrom.*, 2014, **29**, 262-271.
46. M. Aghaei and A. Bogaerts, Particle transport through an inductively coupled plasma torch: elemental droplet evaporation, *J. Anal. At. Spectrom.*, 2016, **31**, 631-641.
47. G. C. Y. Chan and G. M. Hieftje, Local cooling, plasma reheating and thermal pinching induced by single aerosol droplets injected into an inductively coupled plasma, *Spectrochim. Acta B*, 2016, **121**, 55-66.
48. I. Kálomista, A. Kéri and G. Galbács, Optimization of plasma sampling depth and aerosol gas flow rates for single particle inductively coupled plasma mass spectrometry analysis, *Talanta*, 2017, **172**, 147-154.
49. K. H. Chun, H. Zhang and W. T. Chan, Double-viewing-position single-particle inductively coupled plasma-atomic emission spectrometry for the selection of ICP sampling position in SP-ICP measurements, *Anal. Sci.*, 2018, **34**, 711-717.
50. S. J. Hill, A. Fisher and M. Liezers, in *Inductively Coupled Plasma Mass Spectrometry Handbook*, ed. S. M. Nelms, Blackwell Publishing Ltd, Oxford, UK, 2005, pp. 1-25.
51. H. Niu and R. S. Houk, Fundamental aspects of ion extraction in inductively coupled plasma mass spectrometry, *Spectrochim. Acta B*, 1996, **51**, 779-815.
52. M. D. Montaño, H. R. Badiei, S. Bazargan and J. F. Ranville, Improvements in the detection and characterization of engineered nanoparticles using spICP-MS with microsecond dwell times, *Environ. Sci.: Nano*, 2014, **1**, 338-346.
53. T. W. May and R. H. Wiedmeyer, A table of polyatomic interferences in ICP-MS, *Atom. Spectrosc.*, 1998, **19**, 150-155.
54. F. Laborda, J. Medrano and J. R. Castillo, Quality of quantitative and semiquantitative results in inductively coupled plasma mass spectrometry, *J. Anal. At. Spectrom.*, 2001, **16**, 732-738.
55. A. T. Ince, J. G. Williams and A. L. Gray, Noise in inductively-coupled plasma-mass spectrometry - some preliminary measurements, *J. Anal. At. Spectrom.*, 1993, **8**, 899-903.
56. J. Liu, K. E. Murphy, R. I. MacCuspie and M. R. Winchester, Capabilities of single particle inductively coupled plasma mass spectrometry for the size measurement of nanoparticles: a case study on gold nanoparticles, *Anal. Chem.*, 2014, **86**, 3405-3414.

57. L. A. Rush, M. C. Endres, M. Liezers, J. D. Ward, G. C. Eiden and A. M. Duffin, Collisional dampening for improved quantification in single particle inductively coupled plasma mass spectrometry, *Talanta*, 2018, **189**, 268-273.
58. E. Bolea-Fernandez, D. Leite, A. Rua-Ibarz, L. Balcaen, M. Aramendia, M. Resano and F. Vanhaecke, Characterization of SiO_2 nanoparticles by single particle-inductively coupled plasma-tandem mass spectrometry (SP-ICP-MS/MS), *J. Anal. At. Spectrom.*, 2017, **32**, 2140-2152.
59. S. Candás-Zapico, D. J. Kutscher, M. Montes-Bayón and J. Bettmer, Single particle analysis of TiO_2 in candy products using triple quadrupole ICP-MS, *Talanta*, 2018, **180**, 309-315.
60. M. Tharaud, A. P. Gondikas, M. F. Benedetti, F. von der Kammer, T. Hofmann and G. Cornelis, TiO_2 nanomaterial detection in calcium rich matrices by spICPMS. A matter of resolution and treatment, *J. Anal. At. Spectrom.*, 2017, **32**, 1400-1411.
61. P. Shaw and A. Donard, Nano-particle analysis using dwell times between 10 µs and 70 µs with an upper counting limit of greater than 3×10^7 cps and a gold nanoparticle detection limit of less than 10 nm diameter, *J. Anal. At. Spectrom.*, 2016, **31**, 1234-1242.
62. J. Tuoriniemi, G. Cornelis and M. Hassellöv, A new peak recognition algorithm for detection of ultra-small nano-particles by single particle ICP-MS using rapid time resolved data acquisition on a sector-field mass spectrometer, *J. Anal. At. Spectrom.*, 2015, **30**, 1723-1729.
63. J. Tuoriniemi, G. Cornelis and M. Hassellöv, Improving the accuracy of single particle ICPMS for measurement of size distributions and number concentrations of nanoparticles by determining analyte partitioning during nebulisation, *J. Anal. At. Spectrom.*, 2014, **29**, 743-752.
64. J. Tuoriniemi, M. D. Jurgens, M. Hassellöv and G. Cornelis, Size dependence of silver nanoparticle removal in a wastewater treatment plant mesocosm measured by FAST single particle ICP-MS, *Environ. Sci.: Nano*, 2017, **4**, 1189-1197.
65. A. J. Managh, D. N. Douglas, K. M. Cowen, H. J. Reid and B. L. Sharp, Acquisition of fast transient signals in ICP-MS with enhanced time resolution, *J. Anal. At. Spectrom.*, 2016, **31**, 1688-1692.
66. K. Newman, C. Metcalfe, J. Martin, H. Hintelmann, P. Shaw and A. Donard, Improved single particle ICP-MS characterization of silver nanoparticles at environmentally relevant concentrations, *J. Anal. At. Spectrom.*, 2016, **31**, 2069-2077.
67. S. Yongyang, W. Wei, L. Zhiming, D. Hu, Z. Guoqing, X. Jiang and R. Xiangjun, Direct detection and isotope analysis of individual particles in suspension by single particle mode MC-ICP-MS for nuclear safety, *J. Anal. At. Spectrom.*, 2015, **30**, 1184-1190.
68. L. Telgmann, C. D. Metcalfe and H. Hintelmann, Rapid size characterization of silver nanoparticles by single particle ICP-MS and isotope dilution, *J. Anal. At. Spectrom.*, 2014, **29**, 1265-1272.
69. C. A. Sötebier, D. J. Kutscher, L. Rottmann, N. Jakubowski, U. Panne and J. Bettmer, Combination of single particle ICP-QMS and isotope dilution analysis for the determination of size, particle number and number size

distribution of silver nanoparticles, *J. Anal. At. Spectrom.*, 2016, **31**, 2045-2052.

70. O. Borovinskaya, B. Hattendorf, M. Tanner, S. Gschwind and D. Günther, A prototype of a new inductively coupled plasma time-of-flight mass spectrometer providing temporally resolved, multi-element detection of short signals generated by single particles and droplets, *J. Anal. At. Spectrom.*, 2013, **28**, 226-233.
71. J. Tuoriniemi, G. Cornelis and M. Hassellöv, Size discrimination and detection capabilities of single-particle ICPMS for environmental analysis of silver nanoparticles, *Anal. Chem.*, 2012, **84**, 3965-3972.
72. S. Lee, X. Bi, R. B. Reed, J. F. Ranville, P. Herckes and P. Westerhoff, Nanoparticle size detection limits by single particle ICP-MS for 40 elements, *Environ. Sci. Technol.*, 2014, **48**, 10291-10300.
73. O. Borovinskaya, S. Gschwind, B. Hattendorf, M. Tanner and D. Günther, Simultaneous mass quantification of nanoparticles of different composition in a mixture by microdroplet generator-ICPTOFMS, *Anal. Chem.*, 2014, **86**, 8142-8148.
74. A. Praetorius, A. Gundlach-Graham, E. Goldberg, W. Fabienke, J. Navratilova, A. Gondikas, R. Kaegi, D. Günther, T. Hofmann and F. von der Kammer, Single-particle multi-element fingerprinting (spMEF) using inductively-coupled plasma time-of-flight mass spectrometry (ICP-TOFMS) to identify engineered nanoparticles against the elevated natural background in soils, *Environ. Sci.: Nano*, 2017, **4**, 307-314.
75. A. Gondikas, F. von der Kammer, R. Kaegi, O. Borovinskaya, E. Neubauer, J. Navratilova, A. Praetorius, G. Cornelis and T. Hofmann, Where is the nano? Analytical approaches for the detection and quantification of TiO_2 engineered nanoparticles in surface waters, *Environ. Sci.: Nano*, 2018, **5**, 313-326.
76. S. Naasz, S. Weigel, O. Borovinskaya, A. Serva, C. Cascio, A. K. Undas, F. C. Simeone, H. J. P. Marvin and R. J. B. Peters, Multi-element analysis of single nanoparticles by ICP-MS using quadrupole and time-of-flight technologies, *J. Anal. At. Spectrom.*, 2018, **33**, 835-845.
77. A. Hineman and C. Stephan, Effect of dwell time on single particle inductively coupled plasma mass spectrometry data acquisition quality, *J. Anal. At. Spectrom.*, 2014, **29**, 1252-1257.
78. I. Abad-Álvaro, E. Peña-Vázquez, E. Bolea, P. Bermejo-Barrera, J. R. Castillo and F. Laborda, Evaluation of number concentration quantification by single-particle inductively coupled plasma mass spectrometry: microsecond vs. millisecond dwell times, *Anal. Bioanal. Chem.*, 2016, **408**, 5089-5097.
79. I. Kálomista, A. Kéri, D. Ungor, E. Csapó, I. Dékány, T. Prohaska and G. Galbács, Dimensional characterization of gold nanorods by combining millisecond and microsecond temporal resolution single particle ICP-MS measurements, *J. Anal. At. Spectrom.*, 2017, **32**, 2455-2462.
80. A. Kéri, I. Kálomista, D. Ungor, A. Bélteki, E. Csapó, I. Dékány, T. Prohaska and G. Galbács, Determination of the structure and composition of Au-Ag bimetallic spherical nanoparticles using single particle ICP-MS

measurements performed with normal and high temporal resolution, *Talanta*, 2018, **179**, 193-199.
81. M. D. Montaño, B. J. Majestic, A. K. Jamting, P. Westerhoff and J. F. Ranville, Methods for the detection and characterization of silica colloids by microsecond spICP-MS, *Anal. Chem.*, 2016, **88**, 4733-4741.
82. D. Mozhayeva and C. Engelhard, A quantitative nanoparticle extraction method for microsecond time resolved single-particle ICP-MS data in the presence of a high background, *J. Anal. At. Spectrom.*, 2019, DOI: 10.1039/c9ja00042a.
83. S. Weigel, R. Peters, K. Loeschner, R. Grombe and T. P. J. Linsinger, Results of an interlaboratory method performance study for the size determination and quantification of silver nanoparticles in chicken meat by single-particle inductively coupled plasma mass spectrometry (sp-ICP-MS), *Anal. Bioanal. Chem.*, 2017, **409**, 4839-4848.
84. T. P. Linsinger, R. Peters and S. Weigel, International interlaboratory study for sizing and quantification of Ag nanoparticles in food simulants by single-particle ICPMS, *Anal. Bioanal. Chem.*, 2014, **406**, 3835-3843.
85. A. R. Montoro Bustos, K. P. Purushotham, A. Possolo, N. Farkas, A. E. Vladar, K. E. Murphy and M. R. Winchester, Validation of single particle ICP-MS for routine measurements of nanoparticle size and number size distribution, *Anal. Chem.*, 2018, **90**, 14376-14386.
86. R. P. Lamsal, G. Jerkiewicz and D. Beauchemin, Flow injection single particle inductively coupled plasma mass spectrometry: an original simple approach for the characterization of metal-based nanoparticles, *Anal. Chem.*, 2016, **88**, 10552-10558.
87. C. Toncelli, K. Mylona, M. Tsapakis and S. A. Pergantis, Flow injection with on-line dilution and single particle inductively coupled plasma – mass spectrometry for monitoring silver nanoparticles in seawater and in marine microorganisms, *J. Anal. At. Spectrom.*, 2016, **31**, 1430-1439.
88. W. W. Lee and W. T. Chan, Calibration of single-particle inductively coupled plasma-mass spectrometry (SP-ICP-MS), *J. Anal. At. Spectrom.*, 2015, **30**, 1245-1254.
89. F. Laborda, J. Jiménez-Lamana, E. Bolea and J. R. Castillo, Critical considerations for the determination of nanoparticle number concentrations, size and number size distributions by single particle ICP-MS, *J. Anal. At. Spectrom.*, 2013, **28**, 1220-1232.
90. X. Y. Bi, S. Lee, J. F. Ranville, P. Sattigeri, A. Spanias, P. Herckes and P. Westerhoff, Quantitative resolution of nanoparticle sizes using single particle inductively coupled plasma mass spectrometry with the K-means clustering algorithm, *J. Anal. At. Spectrom.*, 2014, **29**, 1630-1639.
91. G. Cornelis and M. Hassellöv, A signal deconvolution method to discriminate smaller nanoparticles in single particle ICP-MS, *J. Anal. At. Spectrom.*, 2014, **29**, 134-144.
92. A. Gundlach-Graham, L. Hendriks, K. Mehrabi and D. Günther, Monte Carlo simulation of low-count signals in time-of-flight mass spectrometry and its application to single-particle detection, *Anal. Chem.*, 2018, **90**, 11847-11855.

93. M. Hadioui, C. Peyrot and K. J. Wilkinson, Improvements to single particle ICPMS by the online coupling of ion exchange resins, *Anal. Chem.*, 2014, **86**, 4668-4674.
94. D. M. Schwertfeger, J. R. Velicogna, A. H. Jesmer, R. P. Scroggins and J. I. Princz, Single particle-inductively coupled plasma mass spectroscopy analysis of metallic nanoparticles in environmental samples with large dissolved analyte fractions, *Anal. Chem.*, 2016, **88**, 9908-9914.
95. S. A. Pergantis, T. L. Jones-Lepp and E. M. Heithmar, Hydrodynamic chromatography online with single particle-inductively coupled plasma mass spectrometry for ultratrace detection of metal-containing nanoparticles, *Anal. Chem.*, 2012, **84**, 6454-6462.
96. K. A. Huynh, E. Siska, E. Heithmar, S. Tadjiki and S. A. Pergantis, Detection and quantification of silver nanoparticles at environmentally relevant concentrations using asymmetric flow field-flow fractionation online with single particle inductively coupled plasma mass spectrometry, *Anal. Chem.*, 2016, **88**, 4909-4916.
97. J. Tan, J. Liu, M. Li, H. El Hadri, V. A. Hackley and M. R. Zachariah, Electrospray-differential mobility hyphenated with single particle inductively coupled plasma mass spectrometry for characterization of nanoparticles and their aggregates, *Anal. Chem.*, 2016, **88**, 8548-8555.
98. B. Franze, I. Strenge and C. Engelhard, Separation and detection of gold nanoparticles with capillary electrophoresis and ICP-MS in single particle mode (CE-SP-ICP-MS), *J. Anal. At. Spectrom.*, 2017, **32**, 1481-1489.
99. D. Mozhayeva and C. Engelhard, Separation of silver nanoparticles with different coatings by capillary electrophoresis coupled to ICP-MS in single particle mode, *Anal. Chem.*, 2017, **89**, 9767-9774.
100. B. Hetzer, A. Burcza, V. Graf, E. Walz and R. Greiner, Online-coupling of AF(4) and single particle-ICP-MS as an analytical approach for the selective detection of nanosilver release from model food packaging films into food simulants, *Food Control*, 2017, **80**, 113-124.
101. D. Rakcheev, A. Philippe and G. E. Schaumann, Hydrodynamic chromatography coupled with single particle-inductively coupled plasma mass spectrometry for investigating nanoparticles agglomerates, *Anal. Chem.*, 2013, **85**, 10643-10647.
102. K. Proulx, M. Hadioui and K. J. Wilkinson, Separation, detection and characterization of nanomaterials in municipal wastewaters using hydrodynamic chromatography coupled to ICPMS and single particle ICPMS, *Anal. Bioanal. Chem.*, 2016, **408**, 5147-5155.
103. Y. Yang, C. L. Long, H. P. Li, Q. Wang and Z. G. Yang, Analysis of silver and gold nanoparticles in environmental water using single particle-inductively coupled plasma-mass spectrometry, *Sci. Total Environ.*, 2016, **563-564**, 996-1007.
104. M. van der Zande, R. J. Vandebriel, E. Van Doren, E. Kramer, Z. Herrera Rivera, C. S. Serrano-Rojero, E. R. Gremmer, J. Mast, R. J. Peters, P. C. Hollman, P. J. Hendriksen, H. J. Marvin, A. A. Peijnenburg and H. Bouwmeester, Distribution, elimination, and toxicity of silver nanoparticles and silver ions in rats after 28-day oral exposure, *ACS Nano*, 2012, **6**, 7427-7442.

105. J. G. Coleman, A. J. Kennedy, A. J. Bednar, J. F. Ranville, J. G. Laird, A. R. Harmon, C. A. Hayes, E. P. Gray, C. P. Higgins, G. Lotufo and J. A. Steevens, Comparing the effects of nanosilver size and coating variations on bioavailability, internalization, and elimination, using Lumbriculus variegatus, *Environ. Toxicol. Chem.*, 2013, **32**, 2069-2077.
106. E. P. Gray, J. G. Coleman, A. J. Bednar, A. J. Kennedy, J. F. Ranville and C. P. Higgins, Extraction and analysis of silver and gold nanoparticles from biological tissues using single particle inductively coupled plasma mass spectrometry, *Environ. Sci. Technol.*, 2013, **47**, 14315-14323.
107. L. D. Scanlan, R. B. Reed, A. V. Loguinov, P. Antczak, A. Tagmount, S. Aloni, D. T. Nowinski, P. Luong, C. Tran, N. Karunaratne, D. Pham, X. X. Lin, F. Falciani, C. P. Higgins, J. F. Ranville, C. D. Vulpe and B. Gilbert, Silver nanowire exposure results in internalization and toxicity to Daphnia magna, *ACS Nano*, 2013, **7**, 10681-10694.
108. K. Loeschner, M. S. Brabrand, J. J. Sloth and E. H. Larsen, Use of alkaline or enzymatic sample pretreatment prior to characterization of gold nanoparticles in animal tissue by single-particle ICPMS, *Anal. Bioanal. Chem.*, 2014, **406**, 3845-3851.
109. R. J. Peters, Z. H. Rivera, G. van Bemmel, H. J. Marvin, S. Weigel and H. Bouwmeester, Development and validation of single particle ICP-MS for sizing and quantitative determination of nano-silver in chicken meat, *Anal. Bioanal. Chem.*, 2014, **406**, 3875-3885.
110. R. Tassinari, F. Cubadda, G. Moracci, F. Aureli, M. D'Amato, M. Valeri, B. De Berardis, A. Raggi, A. Mantovani, D. Passeri, M. Rossi and F. Maranghi, Oral, short-term exposure to titanium dioxide nanoparticles in Sprague-Dawley rat: focus on reproductive and endocrine systems and spleen, *Nanotoxicology*, 2014, **8**, 654-662.
111. S. Makama, R. Peters, A. Undas and N. W. van den Brink, A novel method for the quantification, characterisation and speciation of silver nanoparticles in earthworms exposed in soil, *Environ. Chem.*, 2015, **12**, 643-651.
112. R. Grombe, G. Allmaier, J. Charoud-Got, A. Dudkiewicz, H. Emteborg, T. Hofmann, E. H. Larsen, A. Lehner, M. Llinàs, K. Loeschner, K. Mølhave, R. J. Peters, J. Seghers, C. Solans, F. von der Kammer, S. Wagner, S. Weigel and T. P. J. Linsinger, Feasibility of the development of reference materials for the detection of Ag nanoparticles in food: neat dispersions and spiked chicken meat, *Accredit. Qual. Assur.*, 2015, **20**, 3-16.
113. L. Campagnolo, M. Massimiani, L. Vecchione, D. Piccirilli, N. Toschi, A. Magrini, E. Bonanno, M. Scimeca, L. Castagnozzi, G. Buonanno, L. Stabile, F. Cubadda, F. Aureli, P. H. Fokkens, W. G. Kreyling, F. R. Cassee and A. Pietroiusti, Silver nanoparticles inhaled during pregnancy reach and affect the placenta and the foetus, *Nanotoxicology*, 2017, **11**, 687-698.
114. F. Gallocchio, G. Biancotto, V. Cibin, C. Losasso, S. Belluco, R. Peters, G. van Bemmel, C. Cascio, S. Weigel, P. Tromp, F. Gobbo, S. Catania and A. Ricci, Transfer study of silver nanoparticles in poultry production, *J. Agric. Food Chem.*, 2017, **65**, 3767-3774.
115. M. E. Johnson, S. K. Hanna, A. R. Montoro Bustos, C. M. Sims, L. C. Elliott, A. Lingayat, A. C. Johnston, B. Nikoobakht, J. T. Elliott, R. D. Holbrook, K.

C. Scott, K. E. Murphy, E. J. Petersen, L. L. Yu and B. C. Nelson, Separation, sizing, and quantitation of engineered nanoparticles in an organism model using inductively coupled plasma mass spectrometry and image analysis, *ACS Nano*, 2017, **11**, 526-540.

116. B. Kollander, F. Widemo, E. Agren, E. H. Larsen and K. Loeschner, Detection of lead nanoparticles in game meat by single particle ICP-MS following use of lead-containing bullets, *Anal. Bioanal. Chem.*, 2017, **409**, 1877-1885.
117. K. Ramos, L. Ramos and M. M. Gómez-Gómez, Simultaneous characterisation of silver nanoparticles and determination of dissolved silver in chicken meat subjected to in vitro human gastrointestinal digestion using single particle inductively coupled plasma mass spectrometry, *Food Chem.*, 2017, **221**, 822-828.
118. Q. Li, Z. Wang, J. Mo, G. Zhang, Y. Chen and C. Huang, Imaging gold nanoparticles in mouse liver by laser ablation inductively coupled plasma mass spectrometry, *Sci. Rep.*, 2017, **7**, 2965.
119. J. Modrzynska, T. Berthing, G. Ravn-Haren, K. Kling, A. Mortensen, R. R. Rasmussen, E. H. Larsen, A. T. Saber, U. Vogel and K. Loeschner, In vivo-induced size transformation of cerium oxide nanoparticles in both lung and liver does not affect long-term hepatic accumulation following pulmonary exposure, *PLoS One*, 2018, **13**, e0202477.
120. H. K. Sung, E. Jo, E. Kim, S. K. Yoo, J. W. Lee, P. J. Kim, Y. Kim and I. C. Eom, Analysis of gold and silver nanoparticles internalized by zebrafish (Danio rerio) using single particle-inductively coupled plasma-mass spectrometry, *Chemosphere*, 2018, **209**, 815-822.
121. M. V. Taboada-López, S. Iglesias-López, P. Herbello-Hermelo, P. Bermejo-Barrera and A. Moreda-Piñeiro, Ultrasound assisted enzymatic hydrolysis for isolating titanium dioxide nanoparticles from bivalve mollusk before sp-ICP-MS, *Anal. Chim. Acta*, 2018, **1018**, 16-25.
122. F. Abdolahpur Monikh, L. Chupani, E. Zusková, R. Peters, M. Vancová, M. G. Vijver, P. Porcal and W. J. Peijnenburg, Method for extraction and quantification of metal-based nanoparticles in biological media: number-based biodistribution and bioconcentration, *Environ. Sci. Technol.*, 2019, **53**, 946−953.
123. S. Hu, R. Liu, S. Zhang, Z. Huang, Z. Xing and X. Zhang, A new strategy for highly sensitive immunoassay based on single-particle mode detection by inductively coupled plasma mass spectrometry, *J. Am. Soc. Mass Spectrom.*, 2009, **20**, 1096-1103.
124. S. Zhang, G. Han, Z. Xing, S. Zhang and X. Zhang, Multiplex DNA assay based on nanoparticle probes by single particle inductively coupled plasma mass spectrometry, *Anal. Chem.*, 2014, **86**, 3541-3547.
125. H. Klingberg, L. B. Oddershede, K. Loeschner, E. H. Larsen, S. Loft and P. Møller, Uptake of gold nanoparticles in primary human endothelial cells, *Toxicol. Res.*, 2015, **4**, 655-666.
126. I. L. Hsiao, F. S. Bierkandt, P. Reichardt, A. Luch, Y. J. Huang, N. Jakubowski, J. Tentschert and A. Haase, Quantification and visualization of cellular uptake of TiO_2 and Ag nanoparticles: comparison of different ICP-MS techniques, *J. Nanobiotechnology*, 2016, **14**, 50.

127. A. Malysheva, N. Voelcker, P. E. Holm and E. Lombi, Unraveling the complex behavior of AgNPs driving NP-cell interactions and toxicity to algal cells, *Environ. Sci. Technol.*, 2016, **50**, 12455-12463.
128. B. Krause, T. Meyer, H. Sieg, C. Kästner, P. Reichardt, J. Tentschert, H. Jungnickel, I. Estrela-Lopis, A. Burel, S. Chevance, F. Gauffre, P. Jalili, J. Meijer, L. Böhmert, A. Braeuning, A. F. Thünemann, F. Emmerling, V. Fessard, P. Laux, A. Lampen and A. Luch, Characterization of aluminum, aluminum oxide and titanium dioxide nanomaterials using a combination of methods for particle surface and size analysis, *RSC Adv.*, 2018, **8**, 14377-14388.
129. I. Aharchaou, J. S. Py, S. Cambier, J. L. Loizeau, G. Cornelis, P. Rousselle, E. Battaglia and D. A. L. Vignati, Chromium hazard and risk assessment: New insights from a detailed speciation study in a standard test medium, *Environ. Toxicol. Chem.*, 2018, **37**, 983-992.
130. A. P. Walczak, R. Fokkink, R. Peters, P. Tromp, Z. E. Herrera Rivera, I. M. Rietjens, P. J. Hendriksen and H. Bouwmeester, Behaviour of silver nanoparticles and silver ions in an in vitro human gastrointestinal digestion model, *Nanotoxicology*, 2013, **7**, 1198-1210.
131. S. V. Jenkins, H. Qu, T. Mudalige, T. M. Ingle, R. Wang, F. Wang, P. C. Howard, J. Chen and Y. Zhang, Rapid determination of plasmonic nanoparticle agglomeration status in blood, *Biomaterials*, 2015, **51**, 226-237.
132. E. Leese, J. F. Staff, V. A. Carolan and J. Morton, Exhaled breath condensate: a novel matrix for biological monitoring to assess occupational exposure to respirable crystalline silica, *Ann. Work Expo. Health*, 2017, **61**, 902-906.
133. M. Witzler, F. Küllmer and K. Günther, Validating a single-particle ICP-MS method to measure nanoparticles in human whole blood for nanotoxicology, *Anal. Lett.*, 2017, **51**, 587-599.
134. J. Vidmar, T. Buerki-Thurnherr and K. Loeschner, Comparison of the suitability of alkaline or enzymatic sample pre-treatment for characterization of silver nanoparticles in human tissue by single particle ICP-MS, *J. Anal. At. Spectrom.*, 2018, **33**, 752-761.
135. J. Vidmar, K. Loeschner, M. Correia, E. H. Larsen, P. Manser, A. Wichser, K. Boodhia, Z. S. Al-Ahmady, J. Ruiz, D. Astruc and T. Buerki-Thurnherr, Translocation of silver nanoparticles in the ex vivo human placenta perfusion model characterized by single particle ICP-MS, *Nanoscale*, 2018, **10**, 11980-11991.
136. R. B. Reed, D. G. Goodwin, K. L. Marsh, S. S. Capracotta, C. P. Higgins, D. H. Fairbrother and J. F. Ranville, Detection of single walled carbon nanotubes by monitoring embedded metals, *Environ. Sci.: Process. Impacts*, 2013, **15**, 204-213.
137. J. J. Wang, R. S. Lankone, R. B. Reed, D. H. Fairbrother and J. F. Ranville, Analysis of single-walled carbon nanotubes using spICP-MS with microsecond dwell time, *NanoImpact*, 2016, **1**, 65-72.
138. R. S. Lankone, J. Wang, J. F. Ranville and D. H. Fairbrother, Photodegradation of polymer-CNT nanocomposites: effect of CNT loading and CNT release characteristics, *Environ. Sci.: Nano*, 2017, **4**, 967-982.

139. Y. Dan, H. Shi, C. Stephan and X. Liang, Rapid analysis of titanium dioxide nanoparticles in sunscreens using single particle inductively coupled plasma–mass spectrometry, *Microchem. J.*, 2015, **122**, 119-126.
140. I. de la Calle, M. Menta, M. Klein and F. Seby, Screening of TiO_2 and Au nanoparticles in cosmetics and determination of elemental impurities by multiple techniques (DLS, SP-ICP-MS, ICP-MS and ICP-OES), *Talanta*, 2017, **171**, 291-306.
141. B. Bocca, S. Caimi, O. Senofonte, A. Alimonti and F. Petrucci, ICP-MS based methods to characterize nanoparticles of TiO_2 and ZnO in sunscreens with focus on regulatory and safety issues, *Sci. Total Environ.*, 2018, **630**, 922-930.
142. I. de la Calle, M. Menta, M. Klein, B. Maxit and F. Séby, Towards routine analysis of TiO 2 (nano-)particle size in consumer products: Evaluation of potential techniques, *Spectrochim. Acta B*, 2018, **147**, 28-42.
143. P. J. Lu, S. W. Fang, W. L. Cheng, S. C. Huang, M. C. Huang and H. F. Cheng, Characterization of titanium dioxide and zinc oxide nanoparticles in sunscreen powder by comparing different measurement methods, *J. Food Drug Anal.*, 2018, **26**, 1192-1200.
144. M. Correia, T. Uusimäki, A. Philippe and K. Loeschner, Challenges in determining the size distribution of nanoparticles in consumer products by asymmetric flow field-flow fractionation coupled to inductively coupled plasma-mass spectrometry: the example of Al_2O_3, TiO_2, and SiO_2 nanoparticles in toothpaste, *Separations*, 2018, **5**, 56.
145. Y. S. Zimmermann, A. Schaffer, P. F. Corvini and M. Lenz, Thin-film photovoltaic cells: long-term metal(loid) leaching at their end-of-life, *Environ. Sci. Technol.*, 2013, **47**, 13151-13159.
146. L. M. Furtado, M. E. Hoque, D. F. Mitrano, J. F. Ranville, B. Cheever, P. C. Frost, M. A. Xenopoulos, H. Hintelmann and C. D. Metcalfe, The persistence and transformation of silver nanoparticles in littoral lake mesocosms monitored using various analytical techniques, *Environ. Chem.*, 2014, **11**, 419-430.
147. D. M. Mitrano, J. F. Ranville, A. Bednar, K. Kazor, A. S. Hering and C. P. Higgins, Tracking dissolution of silver nanoparticles at environmentally relevant concentrations in laboratory, natural, and processed waters using single particle ICP-MS (spICP-MS), *Environ. Sci.: Nano*, 2014, **1**, 248-259.
148. M. Hadioui, V. Merdzan and K. J. Wilkinson, Detection and characterization of ZnO nanoparticles in surface and waste waters using single particle ICPMS, *Environ. Sci. Technol.*, 2015, **49**, 6141-6148.
149. A. R. Donovan, C. D. Adams, Y. Ma, C. Stephan, T. Eichholz and H. Shi, Detection of zinc oxide and cerium dioxide nanoparticles during drinking water treatment by rapid single particle ICP-MS methods, *Anal. Bioanal. Chem.*, 2016, **408**, 5137-5145.
150. A. R. Donovan, C. D. Adams, Y. Ma, C. Stephan, T. Eichholz and H. Shi, Single particle ICP-MS characterization of titanium dioxide, silver, and gold nanoparticles during drinking water treatment, *Chemosphere*, 2016, **144**, 148-153.
151. M. Azodi, Y. Sultan and S. Ghoshal, Dissolution behavior of silver nanoparticles and formation of secondary silver nanoparticles in municipal

wastewater by single-particle ICP-MS, *Environ. Sci. Technol.*, 2016, **50**, 13318-13327.

152. J. Jiménez-Lamana and V. I. Slaveykova, Silver nanoparticle behaviour in lake water depends on their surface coating, *Sci. Total Environ.*, 2016, **573**, 946-953.
153. C.-l. Long, Z.-g. Yang, Y. Yang, H.-p. Li and Q. Wang, Determination of gold nanoparticles in natural water using single particle-ICP-MS, *J. Cent. South Univ.*, 2016, **23**, 1611-1617.
154. J. M. Pettibone and J. Liu, In Situ methods for monitoring silver nanoparticle sulfidation in simulated waters, *Environ. Sci. Technol.*, 2016, **50**, 11145-11153.
155. L. Telgmann, M. T. Nguyen, L. Shen, V. Yargeau, H. Hintelmann and C. D. Metcalfe, Single particle ICP-MS as a tool for determining the stability of silver nanoparticles in aquatic matrixes under various environmental conditions, including treatment by ozonation, *Anal. Bioanal. Chem.*, 2016, **408**, 5169-5177.
156. A. Azimzada, N. Tufenkji and K. J. Wilkinson, Transformations of silver nanoparticles in wastewater effluents: links to Ag bioavailability, *Environ. Sci.: Nano*, 2017, **4**, 1339-1349.
157. R. Aznar, F. Barahona, O. Geiss, J. Ponti, T. Jose Luis and J. Barrero-Moreno, Quantification and size characterisation of silver nanoparticles in environmental aqueous samples and consumer products by single particle-ICPMS, *Talanta*, 2017, **175**, 200-208.
158. Y. J. Chang, Y. H. Shih, C. H. Su and H. C. Ho, Comparison of three analytical methods to measure the size of silver nanoparticles in real environmental water and wastewater samples, *J. Hazard. Mater.*, 2017, **322**, 95-104.
159. N. Londono, A. R. Donovan, H. Shi, M. Geisler and Y. Liang, Impact of TiO_2 and ZnO nanoparticles on an aquatic microbial community: effect at environmentally relevant concentrations, *Nanotoxicology*, 2017, **11**, 1140-1156.
160. J. D. Martin, L. Telgmann and C. D. Metcalfe, A method for preparing silver nanoparticle suspensions in bulk for ecotoxicity testing and ecological risk assessment, *Bull. Environ. Contam. Toxicol.*, 2017, **98**, 589-594.
161. R. C. Merrifield, C. Stephan and J. Lead, Determining the concentration dependent transformations of Ag nanoparticles in complex media: using SP-ICP-MS and Au@Ag core-shell nanoparticles as tracers, *Environ. Sci. Technol.*, 2017, **51**, 3206-3213.
162. T. Théoret and K. J. Wilkinson, Evaluation of enhanced darkfield microscopy and hyperspectral analysis to analyse the fate of silver nanoparticles in wastewaters, *Anal. Methods*, 2017, **9**, 3920-3928.
163. C. Toncelli, K. Mylona, I. Kalantzi, A. Tsiola, P. Pitta, M. Tsapakis and S. A. Pergantis, Silver nanoparticles in seawater: A dynamic mass balance at part per trillion silver concentrations, *Sci. Total Environ.*, 2017, **601-602**, 15-21.
164. L. Degenkolb, G. Metreveli, A. Philippe, A. Brandt, K. Leopold, L. Zehlike, H. J. Vogel, G. E. Schaumann, T. Baumann, M. Kaupenjohann, F. Lang, S. Kumahor and S. Klitzke, Retention and remobilization mechanisms of

environmentally aged silver nanoparticles in an artificial riverbank filtration system, *Sci. Total Environ.*, 2018, **645**, 192-204.

165. A. R. Donovan, C. D. Adams, Y. Ma, C. Stephan, T. Eichholz and H. Shi, Fate of nanoparticles during alum and ferric coagulation monitored using single particle ICP-MS, *Chemosphere*, 2018, **195**, 531-541.
166. A. Georgantzopoulou, P. Almeida Carvalho, C. Vogelsang, M. Tilahun, K. Ndungu, A. M. Booth, K. V. Thomas and A. Macken, Ecotoxicological effects of transformed silver and titanium dioxide nanoparticles in the effluent from a lab-scale wastewater treatment system, *Environ. Sci. Technol.*, 2018, **52**, 9431-9441.
167. L. Luo, Y. Yang, H. Li, R. Ding, Q. Wang and Z. Yang, Size characterization of silver nanoparticles after separation from silver ions in environmental water using magnetic reduced graphene oxide, *Sci. Total Environ.*, 2018, **612**, 1215-1222.
168. J. D. Martin, P. C. Frost, H. Hintelmann, K. Newman, M. J. Paterson, L. Hayhurst, M. D. Rennie, M. A. Xenopoulos, V. Yargeau and C. D. Metcalfe, Accumulation of silver in Yellow Perch (Perca flavescens) and Northern Pike (Esox lucius) from a lake dosed with nanosilver, *Environ. Sci. Technol.*, 2018, **52**, 11114-11122.
169. D. C. Rearick, L. Telgmann, H. Hintelmann, P. C. Frost and M. A. Xenopoulos, Spatial and temporal trends in the fate of silver nanoparticles in a whole-lake addition study, *PLoS One*, 2018, **13**, e0201412.
170. J. Vidmar, P. Oprčkal, R. Milačič, A. Mladenovič and J. Ščančar, Investigation of the behaviour of zero-valent iron nanoparticles and their interactions with Cd(2+) in wastewater by single particle ICP-MS, *Sci. Total Environ.*, 2018, **634**, 1259-1268.
171. J. J. López-Mayán, B. Cerneira-Temperán, E. Peña-Vázquez, M. C. Barciela-Alonso, M. R. Domínguez-González and P. Bermejo-Barrera, Evaluation of a cloud point extraction method for the preconcentration and quantification of silver nanoparticles in water samples by ETAAS, *Int. J. Environ. Anal. Chem.*, 2019, **98**, 1434-1447.
172. A. P. Gondikas, F. von der Kammer, R. B. Reed, S. Wagner, J. F. Ranville and T. Hofmann, Release of TiO_2 nanoparticles from sunscreens into surface waters: a one-year survey at the old Danube recreational Lake, *Environ. Sci. Technol.*, 2014, **48**, 5415-5422.
173. L. Li, M. Stoiber, A. Wimmer, Z. Xu, C. Lindenblatt, B. Helmreich and M. Schuster, To what extent can full-scale wastewater treatment plant effluent influence the occurrence of silver-based nanoparticles in surface waters?, *Environ. Sci. Technol.*, 2016, **50**, 6327-6333.
174. S. P. Bitragunta, S. G. Palani, A. Gopala, S. K. Sarkar and V. R. Kandukuri, Detection of TiO_2 nanoparticles in municipal sewage treatment plant and their characterization using single particle ICP-MS, *Bull. Environ. Contam. Toxicol.*, 2017, **98**, 595-600.
175. R. B. Reed, D. P. Martin, A. J. Bednar, M. D. Montaño, P. Westerhoff and J. F. Ranville, Multi-day diurnal measurements of Ti-containing nanoparticle and organic sunscreen chemical release during recreational use of a natural surface water, *Environ. Sci.: Nano*, 2017, **4**, 69-77.

176. M. Loula, A. Kaňa, R. Koplík, J. Hanuš, M. Vosmanská and O. Mestek, Analysis of silver nanoparticles using single-particle inductively coupled plasma – mass spectrometry (ICP-MS): parameters affecting the quality of results, *Anal. Lett.*, 2018, **52**, 288-307.
177. C. D. Metcalfe, T. Sultana, J. Martin, K. Newman, P. Helm, S. Kleywegt, L. Shen and V. Yargeau, Silver near municipal wastewater discharges into western Lake Ontario, Canada, *Environ. Monit. Assess.*, 2018, **190**, 555.
178. R. J. B. Peters, G. van Bemmel, N. B. L. Milani, G. C. T. den Hertog, A. K. Undas, M. van der Lee and H. Bouwmeester, Detection of nanoparticles in Dutch surface waters, *Sci. Total Environ.*, 2018, **621**, 210-218.
179. A. K. Venkatesan, R. B. Reed, S. Lee, X. Bi, D. Hanigan, Y. Yang, J. F. Ranville, P. Herckes and P. Westerhoff, Detection and sizing of Ti-containing particles in recreational waters using single particle ICP-MS, *Bull. Environ. Contam. Toxicol.*, 2018, **100**, 120-126.
180. A. Wimmer, A. Kalinnik and M. Schuster, New insights into the formation of silver-based nanoparticles under natural and semi-natural conditions, *Water Res.*, 2018, **141**, 227-234.
181. A. K. Venkatesan, B. T. Rodríguez, A. R. Marcotte, X. Bi, J. Schoepf, J. F. Ranville, P. Herckes and P. Westerhoff, Using single-particle ICP-MS for monitoring metal-containing particles in tap water, *Environ. Sci.: Water Res. Technol.*, 2018, **4**, 1923-1932.
182. R. J. B. Peters, Z. H. Rivera, H. Bouwmeester, S. Weigel and H. J. P. Marvin, Advanced analytical techniques for the measurement of nanomaterials in complex samples: a comparison, *Qual. Assur. Saf. Crop.*, 2014, **6**, 281-290.
183. S. Addo Ntim, T. A. Thomas and G. O. Noonan, Influence of aqueous food simulants on potential nanoparticle detection in migration studies involving nanoenabled food-contact substances, *Food Addit. Contam. Part A*, 2016, **33**, 905-912.
184. M. Witzler, F. Kullmer, A. Hirtz and K. Günther, Validation of gold and silver nanoparticle analysis in fruit juices by single-particle ICP-MS without sample pretreatment, *J. Agric. Food Chem.*, 2016, **64**, 4165-4170.
185. M. Jokar, M. Correia and K. Loeschner, Behavior of silver nanoparticles and ions in food simulants and low fat cow milk under migration conditions, *Food Control*, 2018, **89**, 77-85.
186. R. J. Peters, G. van Bemmel, Z. Herrera-Rivera, H. P. Helsper, H. J. Marvin, S. Weigel, P. C. Tromp, A. G. Oomen, A. G. Rietveld and H. Bouwmeester, Characterization of titanium dioxide nanoparticles in food products: analytical methods to define nanoparticles, *J. Agric. Food Chem.*, 2014, **62**, 6285-6293.
187. E. Verleysen, E. Van Doren, N. Waegeneers, P. J. De Temmerman, M. Abi Daoud Francisco and J. Mast, TEM and SP-ICP-MS analysis of the release of silver nanoparticles from decoration of pastry, *J. Agric. Food Chem.*, 2015, **63**, 3570-3578.
188. I. de la Calle, M. Menta, M. Klein and F. Seby, Study of the presence of micro- and nanoparticles in drinks and foods by multiple analytical techniques, *Food Chem.*, 2018, **266**, 133-145.
189. K. Loeschner, M. Correia, C. Lopez Chaves, I. Rokkjaer and J. J. Sloth, Detection and characterisation of aluminium-containing nanoparticles in

Chinese noodles by single particle ICP-MS, *Food Addit. Contam. Part A*, 2018, **35**, 86-93.

190. M. V. Taboada-López, P. Herbello-Hermelo, R. Domínguez-González, P. Bermejo-Barrera and A. Moreda-Piñeiro, Enzymatic hydrolysis as a sample pre-treatment for titanium dioxide nanoparticles assessment in surimi (crab sticks) by single particle ICP-MS, *Talanta*, 2019, **195**, 23-32.
191. Y. Dan, W. Zhang, R. Xue, X. Ma, C. Stephan and H. Shi, Characterization of gold nanoparticle uptake by tomato plants using enzymatic extraction followed by single-particle inductively coupled plasma-mass spectrometry analysis, *Environ. Sci. Technol.*, 2015, **49**, 3007-3014.
192. D. Bao, Z. G. Oh and Z. Chen, Characterization of silver nanoparticles internalized by Arabidopsis plants using single particle ICP-MS analysis, *Front. Plant Sci.*, 2016, **7**, 32.
193. Y. Dan, X. Ma, W. Zhang, K. Liu, C. Stephan and H. Shi, Single particle ICP-MS method development for the determination of plant uptake and accumulation of CeO2 nanoparticles, *Anal. Bioanal. Chem.*, 2016, **408**, 5157-5167.
194. J. Jiménez-Lamana, J. Wojcieszek, M. Jakubiak, M. Asztemborska and J. Szpunar, Single particle ICP-MS characterization of platinum nanoparticles uptake and bioaccumulation by Lepidium sativum and Sinapis alba plants, *J. Anal. At. Spectrom.*, 2016, **31**, 2321-2329.
195. I. D. la Calle, P. Pérez-Rodríguez, D. Soto-Gómez and J. E. López-Periago, Detection and characterization of Cu-bearing particles in throughfall samples from vine leaves by DLS, AF4-MALLS (-ICP-MS) and SP-ICP-MS, *Microchem. J.*, 2017, **133**, 293-301.
196. C. C. Li, F. Dang, M. Li, M. Zhu, H. Zhong, H. Hintelmann and D. M. Zhou, Effects of exposure pathways on the accumulation and phytotoxicity of silver nanoparticles in soybean and rice, *Nanotoxicology*, 2017, **11**, 699-709.
197. P. Wang, E. Lombi, S. Sun, K. G. Scheckel, A. Malysheva, B. A. McKenna, N. W. Menzies, F.-J. Zhao and P. M. Kopittke, Characterizing the uptake, accumulation and toxicity of silver sulfide nanoparticles in plants, *Environ. Sci.: Nano*, 2017, **4**, 448-460.
198. A. A. Keller, Y. Huang and J. Nelson, Detection of nanoparticles in edible plant tissues exposed to nano-copper using single-particle ICP-MS, *J. Nanoparticle Res.*, 2018, **20**.
199. K. Kinska, J. Jiménez-Lamana, J. Kowalska, B. Krasnodebska-Ostrega and J. Szpunar, Study of the uptake and bioaccumulation of palladium nanoparticles by Sinapis alba using single particle ICP-MS, *Sci. Total Environ.*, 2018, **615**, 1078-1085.
200. S. S. D. Kumar, N. N. Houreld, E. M. Kroukamp and H. Abrahamse, Cellular imaging and bactericidal mechanism of green-synthesized silver nanoparticles against human pathogenic bacteria, *J. Photochem. Photobiol. B*, 2018, **178**, 259-269.
201. J. Nath, I. Dror, P. Landa, T. Vanek, I. Kaplan-Ashiri and B. Berkowitz, Synthesis and characterization of isotopically-labeled silver, copper and zinc oxide nanoparticles for tracing studies in plants, *Environ. Pollut.*, 2018, **242**, 1827-1837.

202. H. Zhang, Y. Huang, J. Gu, A. Keller, Y. Qin, Y. Bian, K. Tang, X. Qu, R. Ji and L. Zhao, Single particle ICP-MS and GC-MS provide a new insight into the formation mechanisms during the green synthesis of AgNPs, *New J. Chem.*, 2019, **43**, 3946-3955.
203. Y. Yang, X. Bi, P. Westerhoff, K. Hristovski and J. E. McLain, Engineered nanomaterials impact biological carbon conversion in soils, *Environ. Eng. Sci.*, 2014, **31**, 381-392.
204. J. Navratilova, A. Praetorius, A. Gondikas, W. Fabienke, F. von der Kammer and T. Hofmann, Detection of engineered copper nanoparticles in soil using single particle ICP-MS, *Int. J. Environ. Res. Public Health*, 2015, **12**, 15756-15768.
205. H. E. Hadri and V. A. Hackley, Investigation of cloud point extraction for the analysis of metallic nanoparticles in a soil matrix, *Environ. Sci.: Nano*, 2017, **4**, 105-116.
206. A. H. Jesmer, J. R. Velicogna, D. M. Schwertfeger, R. P. Scroggins and J. I. Princz, The toxicity of silver to soil organisms exposed to silver nanoparticles and silver nitrate in biosolids-amended field soil, *Environ. Toxicol. Chem.*, 2017, **36**, 2756-2765.
207. D. Schwertfeger, J. Velicogna, A. Jesmer, H. McShane, R. Scroggins and J. Princz, Ion exchange technique (IET) to characterise Ag^+ exposure in soil extracts contaminated with engineered silver nanoparticles, *Environ. Chem.*, 2017, **14**, 123.
208. D. M. Schwertfeger, J. R. Velicogna, A. H. Jesmer, S. Saatcioglu, H. McShane, R. P. Scroggins and J. I. Princz, Extracting metallic nanoparticles from soils for quantitative analysis: method development using engineered silver nanoparticles and SP-ICP-MS, *Anal. Chem.*, 2017, **89**, 2505-2513.
209. H. El Hadri, S. M. Louie and V. A. Hackley, Assessing the interactions of metal nanoparticles in soil and sediment matrices – a quantitative analytical multi-technique approach, *Environ. Sci.: Nano*, 2018, **5**, 203-214.
210. L. Torrent, M. Iglesias, M. Hidalgo and E. Marguí, Determination of silver nanoparticles in complex aqueous matrices by total reflection X-ray fluorescence spectrometry combined with cloud point extraction, *J. Anal. At. Spectrom.*, 2018, **33**, 383-394.
211. M. A. Gomez-Gonzalez, E. Bolea, P. A. O'Day, J. Garcia-Guinea, F. Garrido and F. Laborda, Combining single-particle inductively coupled plasma mass spectrometry and X-ray absorption spectroscopy to evaluate the release of colloidal arsenic from environmental samples, *Anal. Bioanal. Chem.*, 2016, **408**, 5125-5135.
212. F. Tou, Y. Yang, J. Feng, Z. Niu, H. Pan, Y. Qin, X. Guo, X. Meng, M. Liu and M. F. Hochella, Environmental risk implications of metals in sludges from waste water treatment plants: The discovery of vast stores of metal-containing nanoparticles, *Environ. Sci. Technol.*, 2017, **51**, 4831-4840.
213. K. Folens, T. Van Acker, E. Bolea-Fernandez, G. Cornelis, F. Vanhaecke, G. Du Laing and S. Rauch, Identification of platinum nanoparticles in road dust leachate by single particle inductively coupled plasma-mass spectrometry, *Sci. Total Environ.*, 2018, **615**, 849-856.
214. M. Hadioui, S. Leclerc and K. J. Wilkinson, Multimethod quantification of Ag^+ release from nanosilver, *Talanta*, 2013, **105**, 15-19.

215. D. M. Mitrano, Y. Arroyo Rojas Dasilva and B. Nowack, Effect of variations of washing solution chemistry on nanomaterial physicochemical changes in the laundry cycle, *Environ. Sci. Technol.*, 2015, **49**, 9665-9673.
216. D. Paunescu, C. A. Mora, L. Querci, R. Heckel, M. Puddu, B. Hattendorf, D. Günther and R. N. Grass, Detecting and number counting of single engineered nanoparticles by digital particle polymerase chain reaction, *ACS Nano*, 2015, **9**, 9564-9572.
217. H. A. Kim, B. T. Lee, S. Y. Na, K. W. Kim, J. F. Ranville, S. O. Kim, E. Jo and I. C. Eom, Characterization of silver nanoparticle aggregates using single particle-inductively coupled plasma-mass spectrometry (spICP-MS), *Chemosphere*, 2017, **171**, 468-475.
218. A. S. Adeleye, E. A. Oranu, M. Tao and A. A. Keller, Release and detection of nanosized copper from a commercial antifouling paint, *Water Res.*, 2016, **102**, 374-382.
219. A. Mackevica, M. E. Olsson and S. F. Hansen, Silver nanoparticle release from commercially available plastic food containers into food simulants, *J. Nanoparticle Res.*, 2016, **18**.
220. K. Ramos, M. M. Gómez-Gómez, C. Cámara and L. Ramos, Silver speciation and characterization of nanoparticles released from plastic food containers by single particle ICPMS, *Talanta*, 2016, **151**, 83-90.
221. D. P. Martin, N. L. Melby, S. M. Jordan, A. J. Bednar, A. J. Kennedy, M. E. Negrete, M. A. Chappell and A. R. Poda, Nanosilver conductive ink: A case study for evaluating the potential risk of nanotechnology under hypothetical use scenarios, *Chemosphere*, 2016, **162**, 222-227.
222. I. Abad-Alvaro, E. Bolea, F. Laborda and J. R. Castillo, An ICP-MS-based platform for release studies on silver-based nanomaterials, *J. Anal. At. Spectrom.*, 2017, **32**, 1101-1108.
223. A. Mackevica, M. E. Olsson and S. F. Hansen, The release of silver nanoparticles from commercial toothbrushes, *J. Hazard. Mater.*, 2017, **322**, 270-275.
224. A. Mackevica, M. E. Olsson and S. F. Hansen, Quantitative characterization of TiO_2 nanoparticle release from textiles by conventional and single particle ICP-MS, *J. Nanoparticle Res.*, 2017, **20**.
225. N. Neubauer, L. Scifo, J. Navratilova, A. Gondikas, A. Mackevica, D. Borschneck, P. Chaurand, V. Vidal, J. Rose, F. von der Kammer and W. Wohlleben, Spectroscopic Characterization and Nanosafety of Ag-Modified Antibacterial Leather and LeatheretteNanoscale coloristic pigments: upper limits on releases from pigmented plastic during environmental aging, in food contact, and by leaching, *Environ. Sci. Technol.*, 2017, **51**, 11669-11680.
226. M. C. Sportelli, R. A. Picca, F. Paladini, A. Mangone, L. C. Giannossa, C. D. Franco, A. L. Gallo, A. Valentini, A. Sannino, M. Pollini and N. Cioffi, Spectroscopic characterization and nanosafety of Ag-modified antibacterial leather and leatherette, *Nanomaterials (Basel)*, 2017, **7**, E203.
227. B. Bocca, E. Sabbioni, I. Mičetić, A. Alimonti and F. Petrucci, Size and metal composition characterization of nano- and microparticles in tattoo inks by a combination of analytical techniques, *J. Anal. At. Spectrom.*, 2017, **32**, 616-628.

228. J. Nelson, M. Yamanaka, F. Lopez-Linares, L. Poirier and E. Rogel, Characterization of dissolved metals and metallic nanoparticles in asphaltene solutions by single-particle inductively coupled plasma mass spectrometry, *Energy Fuels*, 2017, **31**, 11971-11976.
229. A. Sápi, A. Kéri, I. Kálomista, D. G. Dobó, Á. S. Ákos Szamosvölgyi, K. L. Juhász, Á. K. Ákos Kukovecz, Z. Kónya and G. Galbács, Determination of the platinum concentration of a Pt/silica nanocomposite decorated with ultra small Pt nanoparticles using single particle inductively coupled plasma mass spectrometry, *J. Anal. At. Spectrom.*, 2017, **32**, 996-1003.
230. S. Addo Ntim, S. Norris, K. Scott, T. A. Thomas and G. O. Noonan, Consumer use effects on nanoparticle release from commercially available ceramic cookware, *Food Control*, 2018, **87**, 31-39.
231. J. Therkorn, L. Calderon, B. Cartledge, N. Thomas, B. Majestic and G. Mainelis, Inactivation of pure bacterial biofilms by impaction of aerosolized consumer products containing nanoparticulate metals, *Environ. Sci.: Nano*, 2018, **5**, 544-555.
232. R. D. Heringer and J. F. Ranville, Gunshot residue (GSR) analysis by single particle inductively coupled plasma mass spectrometry (spICP-MS), *Forensic Sci. Int.*, 2018, **288**, e20-e25.
233. J.-R. Huang, P. Li, J.-H. Wen, X. Hu, Y.-J. Chen, D.-H. Yin and H.-Z. Lian, Determination of arsenic species in mainstream cigarette smoke based on inductively coupled plasma mass spectrometry, *Spectrosc. Lett.*, 2018, **51**, 252-256.
234. J. Jiménez-Lamana, I. Abad-Álvaro, K. Bierla, F. Laborda, J. Szpunar and R. Lobinski, Detection and characterization of biogenic selenium nanoparticles in selenium-rich yeast by single particle ICPMS, *J. Anal. At. Spectrom.*, 2018, **33**, 452-460.
235. M. Van Wassenhoven, M. Goyens, E. Capieaux, P. Devos and P. Dorfman, Nanoparticle characterisation of traditional homeopathically manufactured cuprum metallicum and gelsemium sempervirens medicines and controls, *Homeopathy*, 2018, **107**, 244-263.
236. A. Hegetschweiler, O. Borovinskaya, T. Staudt and T. Kraus, Single particle mass spectrometry of titanium and niobium carbonitride precipitates in steels, *Anal. Chem.*, 2018, **91**, 943-950.
237. A. Helfrich, W. Brüchert and J. Bettmer, Size characterisation of Au nanoparticles by ICP-MS coupling techniques, *J. Anal. At. Spectrom.*, 2006, **21**, 431-434.
238. A. Helfrich and J. Bettmer, Analysis of gold nanoparticles using ICP-MS-based hyphenated and complementary ESI-MS techniques, *Int. J. Mass Spectrom.*, 2011, **307**, 92-98.
239. J. Soto-Alvaredo, M. Montes-Bayón and J. Bettmer, Speciation of silver nanoparticles and silver(I) by reversed-phase liquid chromatography coupled to ICPMS, *Anal. Chem.*, 2013, **85**, 1316-1321.
240. X. X. Zhou, R. Liu and J. F. Liu, Rapid chromatographic separation of dissoluble Ag(I) and silver-containing nanoparticles of 1-100 nanometer in antibacterial products and environmental waters, *Environ. Sci. Technol.*, 2014, **48**, 14516-14524.

241. K. Tiede, A. B. A. Boxall, D. Tiede, S. P. Tear, H. David and J. Lewis, A robust size-characterisation methodology for studying nanoparticle behaviour in 'real' environmental samples, using hydrodynamic chromatography coupled to ICP-MS, *J. Anal. At. Spectrom.*, 2009, **24**, 964-972.
242. A. Philippe and G. E. Schaumann, Evaluation of hydrodynamic chromatography coupled with UV-visible, fluorescence and inductively coupled plasma mass spectrometry detectors for sizing and quantifying colloids in environmental media, *PLoS One*, 2014, **9**, e90559.
243. K. Proulx and K. J. Wilkinson, Separation, detection and characterisation of engineered nanoparticles in natural waters using hydrodynamic chromatography and multi-method detection (light scattering, analytical ultracentrifugation and single particle ICP-MS), *Environ. Chem.*, 2014, **11**, 392-401.
244. D. J. Lewis, Hydrodynamic chromatography - inductively coupled plasma mass spectrometry, with post-column injection capability for simultaneous determination of nanoparticle size, mass concentration and particle number concentration (HDC-PCi-ICP-MS), *Analyst*, 2015, **140**, 1624-1628.
245. A. R. Poda, A. J. Bednar, A. J. Kennedy, A. Harmon, M. Hull, D. M. Mitrano, J. F. Ranville and J. Steevens, Characterization of silver nanoparticles using flow-field flow fractionation interfaced to inductively coupled plasma mass spectrometry, *J. Chromatogr. A*, 2011, **1218**, 4219-4225.
246. B. Schmidt, K. Loeschner, N. Hadrup, A. Mortensen, J. J. Sloth, C. B. Koch and E. H. Larsen, Quantitative characterization of gold nanoparticles by field-flow fractionation coupled online with light scattering detection and inductively coupled plasma mass spectrometry, *Anal. Chem.*, 2011, **83**, 2461-2468.
247. D. M. Mitrano, A. Barber, A. Bednar, P. Westerhoff, C. P. Higgins and J. F. Ranville, Silver nanoparticle characterization using single particle ICP-MS (SP-ICP-MS) and asymmetrical flow field flow fractionation ICP-MS (AF4-ICP-MS), *J. Anal. At. Spectrom.*, 2012, **27**, 1131-1142.
248. O. Geiss, C. Cascio, D. Gilliland, F. Franchini and J. Barrero-Moreno, Size and mass determination of silver nanoparticles in an aqueous matrix using asymmetric flow field flow fractionation coupled to inductively coupled plasma mass spectrometer and ultraviolet-visible detectors, *J. Chromatogr. A*, 2013, **1321**, 100-108.
249. B. Meermann, A.-L. Fabricius, L. Duester, F. Vanhaecke and T. Ternes, Fraction-related quantification of silver nanoparticlesvia on-line species-unspecific post-channel isotope dilution in combination with asymmetric flow-field-flow fractionation (AF4)/sector field ICP-mass spectrometry (ICP-SF-MS), *J. Anal. At. Spectrom.*, 2014, **29**, 287-296.
250. F. Barahona, O. Geiss, P. Urban, I. Ojea-Jimenez, D. Gilliland and J. Barrero-Moreno, Simultaneous determination of size and quantification of silica nanoparticles by asymmetric flow field-flow fractionation coupled to ICPMS using silica nanoparticles standards, *Anal. Chem.*, 2015, **87**, 3039-3047.
251. C. Cascio, O. Geiss, F. Franchini, I. Ojea-Jimenez, F. Rossi, D. Gilliland and L. Calzolai, Detection, quantification and derivation of number size

distribution of silver nanoparticles in antimicrobial consumer products, *J. Anal. At. Spectrom.*, 2015, **30**, 1255-1265.
252. B. Meermann, Field-flow fractionation coupled to ICP-MS: separation at the nanoscale, previous and recent application trends, *Anal. Bioanal. Chem.*, 2015, **407**, 2665-2674.
253. T. K. Mudalige, H. Qu, G. Sanchez-Pomales, P. N. Sisco and S. W. Linder, Simple functionalization strategies for enhancing nanoparticle separation and recovery with asymmetric flow field flow fractionation, *Anal. Chem.*, 2015, **87**, 1764-1772.
254. H. K. Jones and N. E. Ballou, Separations of chemicafly different particles by capillary electrophoresis, *Anal. Chem.*, 1990, **62**, 2484-2490.
255. F.-K. Liu and G.-T. Wei, Adding sodium dodecylsulfate to the running electrolyte enhances the separation of gold nanoparticles by capillary electrophoresis, *Anal. Chim. Acta*, 2004, **510**, 77-83.
256. F.-K. Liu, F.-H. Ko, P.-W. Huang, C.-H. Wu and T.-C. Chu, Studying the size/shape separation and optical properties of silver nanoparticles by capillary electrophoresis, *J. Chromatogr. A*, 2005, **1062**, 139-145.
257. B. Franze and C. Engelhard, Fast separation, characterization, and speciation of gold and silver nanoparticles and their ionic counterparts with micellar electrokinetic chromatography coupled to ICP-MS, *Anal. Chem.*, 2014, **86**, 5713-5720.
258. M. C. Breadmore, Recent advances in enhancing the sensitivity of electrophoresis and electrochromatography in capillaries and microchips, *Electrophoresis*, 2007, **28**, 254-281.
259. M. C. Breadmore, A. Wuethrich, F. Li, S. C. Phung, U. Kalsoom, J. M. Cabot, M. Tehranirokh, A. I. Shallan, A. S. Abdul Keyon, H. H. See, M. Dawod and J. P. Quirino, Recent advances in enhancing the sensitivity of electrophoresis and electrochromatography in capillaries and microchips (2014-2016), *Electrophoresis*, 2017, **38**, 33-59.
260. Z. Liu, P. Sam, S. R. Sirimanne, P. C. McClure, J. Grainger and D. G. Patterson, Field-amplified sample stacking in micellar electrokinetic chromatography for on-column sample concentration of neutral molecules, *J. Chromatogr. A*, 1994, **673**, 125-132.
261. J. P. Quirino and S. Terabe, On-line concentration of neutral analytes for micellar electrokinetic chromatography. II. Reversed electrode polarity stacking mode, *J. Chromatogr. A*, 1997, **791**, 255-267.
262. K. H. Lin, T. C. Chu and F. K. Liu, On-line enhancement and separation of nanoparticles using capillary electrophoresis, *J. Chromatogr. A*, 2007, **1161**, 314-321.
263. F. K. Liu, A high-efficiency capillary electrophoresis-based method for characterizing the sizes of Au nanoparticles, *J. Chromatogr. A*, 2007, **1167**, 231-235.
264. F. K. Liu, Using micellar electrokinetic chromatography for the highly efficient preconcentration and separation of gold nanoparticles, *J. Chromatogr. A*, 2009, **1216**, 2554-2559.
265. F. K. Liu, Extremely highly efficient on-line concentration and separation of gold nanoparticles using the reversed electrode polarity stacking mode and

surfactant-modified capillary electrophoresis, *Anal. Chim. Acta*, 2011, **694**, 167-173.
266. H. E. Pace, N. J. Rogers, C. Jarolimek, V. A. Coleman, C. P. Higgins and J. F. Ranville, Determining transport efficiency for the purpose of counting and sizing nanoparticles via single particle inductively coupled plasma mass spectrometry, *Anal. Chem.*, 2011, **83**, 9361-9369.
267. B. V. Derjaguin and L. D. Landau, Theory of the stability of strongly charged lyophobic sols and adhersion of strongly charged particles in solutions of Electrolytes, *Acta Physicochim. URSS*, 1941, **14**, 633-652.
268. E. J. W. Verwey and J. T. G. Overbeek, *Theory of the Stability of Lyophobic Colloids*, Elsevier Pub. Co., New York, 1948.
269. T. L. Moore, L. Rodriguez-Lorenzo, V. Hirsch, S. Balog, D. Urban, C. Jud, B. Rothen-Rutishauser, M. Lattuada and A. Petri-Fink, Nanoparticle colloidal stability in cell culture media and impact on cellular interactions, *Chem. Soc. Rev.*, 2015, **44**, 6287-6305.
270. J. P. Ryman-Rasmussen, J. E. Riviere and N. A. Monteiro-Riviere, Surface coatings determine cytotoxicity and irritation potential of quantum dot nanoparticles in epidermal keratinocytes, *J. Invest. Dermatol.*, 2007, **127**, 143-153.
271. X. Huang, J. Weng, F. Sang, X. Song, C. Cao and J. Ren, Characterization of quantum dot bioconjugates by capillary electrophoresis with laser-induced fluorescent detection, *J. Chromatogr. A*, 2006, **1113**, 251-254.
272. G. Vicente and L. A. Colón, Separation of bioconjugated quantum dots using capillary electrophoresis, *Anal. Chem.*, 2008, **80**, 1988-1994.
273. M. Hanauer, S. Pierrat, I. Zins, A. Lotz and C. Sönnichsen, Separation of nanoparticles by gel electrophoresis according to size and shape, *Nano Lett.*, 2007, **7**, 2881-2885.
274. Y.-h. Zhang, H.-s. Zhang, M. Ma, X.-f. Guo and H. Wang, The influence of ligands on the preparation and optical properties of water-soluble CdTe quantum dots, *Appl. Surf. Sci.*, 2009, **255**, 4747-4753.
275. F. d'Orlye´, A. Varenne, T. Georgelin, J. M. Siaugue, B. Teste, S. Descroix and P. Gareil, Charge-based characterization of nanometric cationic bifunctional maghemite/silica core/shell particles by capillary zone electrophoresis, *Electrophoresis*, 2009, **30**, 2572-2582.
276. L. Li, H. Yu, D. Liu and T. You, A novel dark-field microscopy technique coupled with capillary electrophoresis for visual analysis of single nanoparticles, *Analyst*, 2013, **138**, 3705-3710.
277. H. Qu, S. W. Linder and T. K. Mudalige, Surface coating and matrix effect on the electrophoretic mobility of gold nanoparticles: a capillary electrophoresis-inductively coupled plasma mass spectrometry study, *Anal. Bioanal. Chem.*, 2017, **409**, 979-988.
278. *Handbook of Capillary Electrophoresis*, CRC Press LLC, USA, 2nd edn., 1997.
279. G. R. Ducatte, N. E. Ballou, C. Quang and S. L. Petersen, Separation and characterization of oxide particles by capillary electrophoresis, *J. Microcolumn Sep.*, 1996, **8**, 403-412.

280. G. Duplatre, M. F. F. Marques and M. d. G. Miguel, Size of sodium dodecyl sulfate micelles in aqueous solutions as studied by positron annihilation lifetime spectroscopy, *J. Phys. Chem.*, 1996, **100**, 16608-16612.
281. J. W. Park and J. S. Shumaker-Parry, Structural study of citrate layers on gold nanoparticles: role of intermolecular interactions in stabilizing nanoparticles, *J. Am. Chem. Soc.*, 2014, **136**, 1907-1921.
282. J. Hedberg, M. Lundin, T. Lowe, E. Blomberg, S. Wold and I. O. Wallinder, Interactions between surfactants and silver nanoparticles of varying charge, *J. Colloid Interface Sci.*, 2012, **369**, 193-201.
283. D. A. Notter, D. M. Mitrano and B. Nowack, Are nanosized or dissolved metals more toxic in the environment? A meta-analysis, *Environ. Toxicol. Chem.*, 2014, **33**, 2733-2739.
284. M. H. Shen, X. X. Zhou, X. Y. Yang, J. B. Chao, R. Liu and J. F. Liu, Exposure medium: key in identifying free Ag^+ as the exclusive species of silver nanoparticles with acute toxicity to Daphnia magna, *Sci. Rep.*, 2015, **5:9674**, 1-8.
285. D. McShan, P. C. Ray and H. Yu, Molecular toxicity mechanism of nanosilver, *J. Food Drug Anal.*, 2014, **22**, 116-127.
286. S. K. Misra, A. Dybowska, D. Berhanu, S. N. Luoma and E. Valsami-Jones, The complexity of nanoparticle dissolution and its importance in nanotoxicological studies, *Sci. Total Environ.*, 2012, **438**, 225-232.
287. J. Vidmar, R. Milačič and J. Ščančar, Sizing and simultaneous quantification of nanoscale titanium dioxide and a dissolved titanium form by single particle inductively coupled plasma mass spectrometry, *Microchem. J.*, 2017, **132**, 391-400.
288. L. Hendriks, A. Gundlach-Graham and D. Günther, Analysis of inorganic nanoparticles by single-particle inductively coupled plasma time-of-flight mass spectrometry, *Chimia (Aarau)*, 2018, **72**, 221-226.
289. *USA Pat.,* US9754774B2, Systems and methods for automated analysis of output in single particle inductively coupled plasma mass spectrometry and similar data sets 2017.
290. H. Kaiser, Die Berechnung der Nachweisempfindlichkeit, *Spectrochim. Acta*, 1947, **3**, 40-67.
291. L. A. Currie, Limits for qualitative detection and quantitative determination - application to radiochemistry, *Anal. Chem.*, 1968, **40**, 586-593.
292. L. A. Currie, The measurement of environmental levels of rare gas nuclides and the treatment of very low-level counting data, *IEEE Trans. Nucl. Sci.*, 1972, **19**, 119-126.
293. L. A. Currie, On the detection of rare, and moderately rare, nuclear events, *J. Radioanal. Nucl. Ch.*, 2008, **276**, 285-297.
294. J. A. Olivares and R. S. Houk, Suppression of analyte signal by various concomitant salts in inductively coupled plasma mass-spectrometry, *Anal. Chem.*, 1986, **58**, 20-25.

List of Abbreviations

y_C	critical level gross counts
y_D	detection limit gross counts
μ_B	average background
"E"	end threshold; when it is reached, the ion cloud extraction ends
"S"	how many data points should be grouped and summed up to judge, if the chosen threshold conditions are reached
"T"	threshold value; when it is reached, an ion cloud extraction begins
"W"	width
µsDAQ	data acquisition system with microsecond time resolution
AES	atomic emission spectroscopy
AF4	asymmetrical flow field-flow fractionation
AFM	atomic force microscopy
Ag^+	ionic silver
BG	background
BPEI	branched polyethylenimine
BSA	bovine serum albumin
C/S	charge-to-size ratio
CAPS	3-cyclohexylamoniuopropanesulfonic acid
CE	capillary electrophoresis
CIGS	copper indium gallium selenide cells
CNT	carbon nanotube

CPE	cloud point extraction
cps	counts per second
CTAB	cetyltrimethylammonium bromide
CZE	capillary zone electrophoresis
DAQ	data acquisition system
DLVO	Derjaguin, Landau, Verwey, and Overbeek
DMEM	Dulbecco's modified eagle medium
DT	dwell time
EIE	easily ionizable elements
EOF	electroosmotic flow
EPA	Environmental Protection Agency
ESD	equivalent spherical diameter
ES-DMA	electrospray-differential mobility analysis
FFF	field-flow fractionation
HDC	hydrodynamic chromatography
ICP-MS	inductively coupled plasma mass spectrometry
ICP-Q-MS	ICP quadrupole MS
IEC	ion-exchange column
KED	kinetic energy discrimination
LA	laser ablation
L_C	critical level
LC	liquid chromatography
L_D	detection limit
LDR	linear dynamic range

L_Q	limit of quantification
m/*z*	mass-to-charge ratio
MA	multielemental analysis
MC	multi-collector
MDG	microdroplet generator
MEKC	micellar electrokinetic chromatography
MOPS	3-morpholinopropane-1-sulfonic acid
MT	migration time
n/a	not applicable
n/s	not specified
NIST	National Institute of Standards and Technology
NOM	natural organic matter
NP	nanoparticle
OECD	The Organization for Economic Co-operation and Development
OPV	organic photovoltaic cells
PBS	phosphate buffered saline
PEG	polyethylene glycol
PFA	perfluoroalkoxy alkane
PNC	particle number concentration
PTFE	polytetrafluoroethylene
PVA	polyvinyl alcohol
PVP	polyvinylpyrrolidone
Q	quadrupole
REPSM	reversed electrode polarity stacking mode

RF	radio frequency
RSD	relative standard deviation
SD	standard deviation
SDS	sodium dodecyl sulfate
SEM	secondary electron multiplier
SF	sector field
SP-ICP-MS	single particle ICP-MS
TAP	tris-acetate-phosphate
TEM	transmission electron microscopy
TMAH	tetramethylammonium hydroxide
TOF	time-of-flight
TQ	triple quadrupole
TSPP	tetrasodium pyrophosphate
WWTP	waste water treatment plant
α	error of the first kind
ß	error of the second kind

List of Figures

Figure 2.1: Number of SP-ICP-MS publications according to the Web of Science database (accessed on 28 May 2019). 314 publications in total. The search command: "SP-ICP-MS" OR "SP-ICPMS" OR "sp-ICPMS" OR "single particle ICPMS" OR "single particle ICP-MS" OR "single particle inductively coupled plasma mass spectrometry" OR "single particle inductively coupled plasma mass-spectrometry" (the characters are not register sensitive). Note that two publication published in 2004-2006, that do not use the above mentioned terms, were added manually. *The results for 2019 are incomplete. 11

Figure 2.2: Sampling position profiles of (a) Au and (b) Zr in the form of aqueous solution of concentration of 10 $\mu g L^{-1}$ and discrete NPs. Reproduced from Ho et al. [41] with permission from The Royal Society of Chemistry, Copyright 2015. 17

Figure 3.1: CE-ICP-MS coupling setup schematic. 92

Figure 3.2: Ion clouds profiles (n = 10, $^{107}Ag^{+}$) of 60 nm sized Ag NPs obtained by SP-ICP-MS analysis of NPs diluted in bi-distilled water (top), in 4.7 mM Na^{+} matrix (middle) both with standard sample introduction, and during a CE-SP-ICP-MS run (bottom). Data was acquired with the µsDAQ and a DT of 5 µs, each ion cloud consists of approximately 730 counts. 96

Figure 3.3: CE-SP-ICP-MS data evaluation capabilities and obtained characteristics presented for 40 nm sized Ag NPs. Total number of particles in boxed-in area: approximately 10,000. 97

Figure 3.4: Influence of the REPSM injection time on the number of detected particles for a mixture of 5 µg L^{-1} 20 nm sized, 35 µg L^{-1} 40 nm sized, and 200 µg L^{-1} 60 nm sized Ag NPs analyzed at 20 kV (logistic fit)..... 100

Figure 3.5: Influence of applied voltage on NPs CE MT for a mixture of 10 µg L^{-1} 20 nm sized, 35 µg L^{-1} 40 nm sized, and 100 µg L^{-1} 60 nm sized Ag NPs analyzed using 110 s injection time in REPSM (exponential decay fit). 101

Figure 3.6: The dependence of number of detected particles on number of injected particles and PNC in NPs mixtures for the mixtures of 20 nm sized, 40 nm sized,

and 60 nm sized Ag NPs analyzed using 110 s injection time in REPSM at 20 kV (linear fit)..... 103

Figure 3.7: Two-dimensional color maps of CE-SP-ICP-MS analysis ($^{107}Ag^+$) of a mixture of 5 µg L^{-1} 20 nm sized, 35 µg L^{-1} 40 nm sized, and 200 µg L^{-1} 60 nm sized Ag NPs analyzed using 3 s injection without REPSM (A) and 110 s injection time in REPSM (B) at 20 kV (note that different color scales are used for (A) and (B); the BG in (A) is also present in (B), but not apparent due to the scale; time axis in (B) includes 110 s injection and 55 s REPSM preconcentration). 105

Figure 4.1: Separation of two-component mixtures and analysis of individual types of 40 nm sized Ag NPs with BPEI, PEG, PVP, and citrate surface coatings of 35 µg L^{-1} (approximately 1×10^8 particles per mL) each. Heat maps show the number of detected particles (monitored at $^{107}Ag^+$, 5 µs DT) at different MTs during a CE-SP-ICP-MS run. The composition of the mixture of different nanomaterials is given in the header of the columns/rows (First row, from left to right: BPEI only; mixture of BPEI and PEG; mixture of BPEI and PVP; etc.). Labels 1 and 2 represent repetitive measurements of the same mixture. 116

Figure 4.2: Separation of two-component mixtures and analysis of individual types of 60 nm sized NPs with PEG, PVP, and citrate surface coatings of 100 µg L^{-1} (approximately 8×10^7 particles per mL) each. Heat maps show the number of detected particles (monitored at $^{107}Ag^+$, 5 µs DT) at different MTs during a CE-SP-ICP-MS run. The composition of the mixture of different nanomaterials is given in the header of the columns/rows (First row: PEG only; mixture of PEG and PVP, etc.). Labels 1 and 2 (e.g. B1, B2) represent repetitive measurements of the same mixture. 119

Figure 4.3: Comparison of a standard CE-ICP-MS plot (A) and first CE-SP-ICP-MS two-dimensional color map (B) acquired from a complex five-component mixture of different nanomaterials (5 µg L^{-1} citrate-coated 20 nm sized, 35 µg L^{-1} each citrate- and PVP-coated 40 nm sized, 100 µg L^{-1} PVP-coated 60 nm sized, and 200 µg L^{-1} citrate-coated 60 nm sized Ag NPs). The analysis was conducted by monitoring at $^{107}Ag^+$ with 5 µs DT, using 110 s injection and REPSM at 20 kV. 121

Figure 5.1: Mean background (BG) signal (recorded with ICP-Q-MS at $^{107}Ag^+$, 10 ms DT) in the 20, 40, 60, 100 nm Ag NPs suspensions (n = 3, different sample measurements on three different days) after the additions of Ag^+ from 0 ng L^{-1} to 100 ng L^{-1} (A) and from 500 ng L^{-1} to 7.5 µg L^{-1} (B) relative to the mean BG signal of Ag^+ calibration solutions without NPs. “Normalized background signal”

represents ratio of the mean BG signal, when Ag^+ was added to the NPs suspension at different concentrations divided by the mean BG signal of Ag^+ calibration solutions of the same concentration but without NPs, in percent. A value of 100% would indicate that the BG counts obtained with and without NPs in solutions are equal. 134

Figure 5.2: Average sizes of 20, 40, 60, 100 nm Ag NPs size distributions (without addition of Ag^+, 0 µg L^{-1}, to NP suspension) depending on different count thresholds during ion cloud extraction (T – number of counts required to flag ion cloud start and E – number of counts to define end of ion cloud extraction). Optimal conditions (S = 5, T = 5, E = 1) are highlighted with black dots. Note: The step size in size resolution is for illustrative purposes only and is a result of data processing. It does not represent the actual size resolution of the SP-ICP-MS method. Also, areas of white colour indicate extraction conditions, which were not tested. 142

Figure 5.3: Influence of ion cloud extraction conditions on maximum of the number of BG events (BG count distribution maximum, see Label A in Figure A.3) during the analysis of 60 nm Ag NPs (left: without, and right: with 7.5 µg L^{-1} Ag^+ added to the NP suspension). Optimal conditions are highlighted with black dots. Note: The step size in size resolution is for illustrative purposes only and a result of data processing. It does not represent the actual size resolution of the SP-ICP-MS method. Also, areas of white colour indicate extraction conditions, which were not tested. 144

Figure A.1: CE-ICP-MS diagrams obtained with 1 s dwell time ($^{107}Ag^+$) (A) by summing up only extracted NPs events from µsDAQ and (B) by summing up 10 ms DTs in the vendor software for a mixture of 5 µg L^{-1} 20 nm sized, 35 µg L^{-1} 40 nm sized, and 200 µg L^{-1} 60 nm sized Ag NPs analyzed using 110 s injection time in REPSM at 20 kV. 153

Figure A.2: Influence of applied voltage on the current in CE using 110 s injection time in REPSM (linear fit with 95% confidence levels)..... 154

Figure A.3: Model histogram with labels that indicate parameters of a NPs size distribution that are used in Chapter 5 to compare different extraction conditions: BG maximum (A), NPs average size (B), width "W" of the size distribution (C, W = 2SD of the NPs average size), minimal size from which NPs can be distinguished from the BG (D), and total number detected of NPs (E). 158

Figure A.4: Average sizes of 20, 40, 60, 100 nm Ag NPs size distributions (NP suspensions in the presence of 7.5 µg L^{-1} of Ag^+) depending on different count thresholds during ion cloud extraction, T and E. Optimal conditions (S = 5, T = 51, E = 39) are highlighted with black dots. Note: The step size in size resolution is for illustrative purposes only and is a result of data processing. It does not represent the actual size resolution of the SP-ICP-MS method. Also, areas of white color indicate extraction conditions, which were not tested. 162

Figure A.5: Number of detected NPs for the 20, 40, 60, 100 nm Ag NPs (with 0.5 µg L^{-1} of Ag^+ in solution) depending on different count thresholds during ion cloud extraction, T and E. Optimal conditions (S = 5, T = 11, E = 5) are highlighted with black dots. The step size in size resolution is for illustrative purposes only and is a result of data processing. It does not represent the actual size resolution of the SP-ICP-MS method. Also, areas of white color indicate extraction conditions, which were not tested. 163

Figure A.6: Number of detected NPs for the 20, 40, 60, 100 nm Ag NPs (with 7.5 µg L^{-1} of Ag^+) depending on different count thresholds during ion cloud extraction, T and E. Optimal conditions (S = 5, T = 51, E = 39) are highlighted with black dots. The step size in size resolution is for illustrative purposes only and is a result of data processing. It does not represent the actual size resolution of the SP-ICP-MS method. Also, areas of white color indicate extraction conditions, which were not tested. 164

Figure A.7: Size starting from which the NP size distribution can be distinguished from the BG for 20 nm Ag NPs at different Ag^+ concentrations (shown on the graphs) depending on different count thresholds during ion cloud extraction, T and E. Optimal conditions are highlighted with black dots. The step size in size resolution is for illustrative purposes only and is a result of data processing. It does not represent the actual size resolution of the SP-ICP-MS method. Also, areas of white color indicate extraction conditions, which were not tested. 165

List of Tables

Table 2.1: An overview of the techniques coupled online to SP-ICP-MS for NPs analysis. 28

Table 2.2: Summary of peer-reviewed SP-ICP-MS nanoanalysis papers with selected experimental conditions, sample matrix, and particle size detection limit. 35

Table 3.1: Main ICP-MS instrumental parameters. 93

Table 4.1: Main ICP-MS instrumental parameters. 112

Table 5.1: ICP-MS instrumental parameters. 130

Table 5.2: Formulas for L_C and L_D[291] for NP ion clouds extraction. 139

Table 5.3: Comparison between $\boldsymbol{yC}$ and $\boldsymbol{yD}$ obtained with Poisson distribution under different approximations for 20 nm Ag NPs spiked with Ag^+.* 140

Table A.1: Characteristics of one-component Ag NPs dispersions.* 155

Table A.2: MTs of two-component Ag NPs dispersions.* 156

Table A.3: Example calculation of $\boldsymbol{yC}$, critical number of gross counts, and $\boldsymbol{yD}$, detection limit for gross counts, for a suspension of 20 nm Ag NPs spiked with 500 ng L^{-1} Ag^+ according to the previous page descriptions. 160

Table A.4: Gross size detection limit ($\boldsymbol{yD}$) for selected ion clouds extraction conditions calculated for a suspension of 20 nm Ag NPs spiked with different concentrations of Ag^+ in solution.* 161

Acknowledgements

My sincere gratitude goes to Prof. Dr. Carsten Engelhard and the research group. The House of Young Talents of the University of Siegen is acknowledged for providing me with the scholarship.

Funding within the project FENOMENO (Grant No.: 03XP0005) is acknowledged. FENOMENO is funded in the FP7 ERA-NET on Nanosafety: Safe Implementation of Innovative Nanoscience and Nanotechnology (SIINN) (http://www.siinn.eu/en/).